DUAL MULTICOLLECTOR LASER ABLATION SPLIT STREAM MASS SPECTROMETRY: APPLICATION TO THE BRUNEAU-JARBIDGE VOLCANIC CENTER, CENTRAL SNAKE RIVER PLAIN, IDAHO

by

Samantha Couper

A thesis submitted to the faculty of
The University of Utah
in partial fulfillment of the requirements for the degree of

Master of Science

in

Geology

Department of Geology and Geophysics

The University of Utah

December 2016

The University of Utah Graduate School

STATEMENT OF THESIS APPROVAL

The thesis of **Samantha Couper**

has been approved by the following supervisory committee members:

Barbara Nash	, Chair	**01/08/2016** Date Approved
Diego P. Fernandez	, Member	**01/08/2016** Date Approved
John R. Bowman	, Member	**01/08/2016** Date Approved

and by **John M. Bartley** , Chair/Dean of

the Department/College/School of **Geology and Geophysics**

and by David B. Kieda, Dean of The Graduate School.

ABSTRACT

The laser ablation split stream technique allows for concurrent measurement of Lu-Hf and U-Pb isotopes in zircon by consuming one sample volume, ensuring a direct relationship between crystallization age and Hf-isotope ratios. This is an improvement over common *in situ* techniques that utilize two sample volumes. In this study, we describe a new method for measuring Lu-Hf and U-Pb isotopes on zircons termed Dual Multicollector Laser Ablation Split Stream ICMPS (DM-LASS-ICPMS). The method is thus far unique because it uses two ThermoFinnigan Neptune Plus multicollector mass spectrometers, which allows high precision measurements of U-Pb as well as Hf. The robust nature of this technique is demonstrated through analyses of 5 natural zircons (91500, Plešovice, Mudtank, Temora-2, R33) and 3 synthetic zircons (MUNZirc 1, 3, and 4) with a 53 μm laser spot. Furthermore, the usefulness of this technique is confirmed by 190 measurements on zircons in rhyolites of the Bruneau-Jarbidge volcanic center. The Bruneau-Jarbidge center, located in the central Snake River Plain of Idaho, is an expression of the Yellowstone hotspot (YHS), and was active from 12.7–8 Ma. The εHf values of zircons from the Bruneau-Jarbidge volcanic center range from -15 to -1.5, indicating a period of increased basaltic input and suppression of a crustal signature that is associated with increased melt production.

TABLE OF CONTENTS

ABSTRACT iii

LIST OF TABLES v

ACKNOWLEDGEMENTS vi

Chapters

I HIGH RESOLUTION U-Pb AND Hf MEASUREMENTS ON ZIRCON USING LASER ABLATION SPLIT STREAM TECHNIQUE 1

- Introuction 2
- Methods 4
- Laser Parameters 8
- Data Reduction 10
- Results 15
- Discussion 26
- References 30

II APPLICATION OF THE DUAL MULTICOLLECTOR LASER ABLATION SPLIT STREAM ICPMS METHOD TO MEASURE Hf, U, Th, AND Pb ISOTOPES IN RHYOLITES OF THE YELLOWSTONE HOTSPOT 33

- Introduction 34
- Methods 41
- Results 44
- Discussion 51
- References 64

Appendices

A Lu-Hf AND U-Pb RESULTS OF BRUNEAU-JARBIDGE ZIRCONS 68

B CATHODOLUMINESCENCE IMAGES OF BRUNEAU-JARBIDGE ZIRCONS 79

LIST OF TABLES

Tables

1 Instrument operating parameters 9

2 Cup configurations for Lu-Hf 9

3 Summary of analyzed samples 39

4 Results of Lu-Hf and U-Pb analysis of BJ zircons 69

ACKNOWLEDGEMENTS

I would like to thank Barbara Nash for her tireless guidance and support in undertaking this project. For sample preparation, I thank John Bowman and Carl Beno who taught me how to mix epoxy and place standards into trenches drilled with the help of Lowell Miyagi. Development of the Dual Multicollector Laser Ablation Split Stream Inductively-Coupled Mass Spectrometry method would not have been possible without the continuous help of Diego Fernandez who provided both time and laboratory resources and was available to fix technical issues even at last-minute notice. Glen Mackey was the first to teach me how to use the ThermoFinnigan Neptune Plus and test multiple cup configurations. Lastly, I want to thank Michael Stearns for his insights into improving split stream precision, sharing his knowledge of U-Th-Pb isotopes, teaching me how to reduce my own data, and the use of his standards.

CHAPTER I

HIGH RESOLUTION U-Pb AND Hf MEASUREMENTS ON ZIRCON USING LASER ABLATION SPLIT STREAM TECHNIQUE

Introduction

The isotope geochemistry of zircon has been applied to a wide variety of chronological and petrological problems ranging from the age distribution of detrital grains in sedimentary basins, the interaction of rocks with hydrothermal fluids, to the origins of magmas. Zircon can incorporate lighter rare earth elements (REE), uranium, and thorium. The Hf^{4+} ion, in particular, substitutes for Zr^{4+} to such a degree that HfO_2 composes 0.5-2 weight percent of magmatic zircon (Hoskin & Schaltegger, 2003), thus making it possible to measure Hf isotopes with high precision in zircon. The ^{176}Hf isotope in zircon results from β- decay of ^{176}Lu and thus fractionation in the Lu-Hf system is measured by the deviation of the $^{176}Hf/^{177}Hf$ isotope ratio (εHf) from that of chondrites (εHf = 0). Positive εHf values indicate mantle signatures and negative εHf values indicate crystallization early in geologic time. For a detailed description of the Lu-Hf system and its applications, see Kinney & Maas (2003) and the references therein.

Zircons are often characterized by zoning in cathodoluminescence (CL) images or multiple domains distinct in CL. This heterogeneity in CL images often reflects heterogeneity in U-Pb isotopes (age), oxygen isotopes, or trace elements as indicated by grain-sized spot analyses. Several microbeam analytical methodologies are employed on a single grain to document this heterogeneity. These include: secondary ion mass spectrometry (SIMS) or sensitive high resolution ion microprobe (SHRIMP) ion beams for oxygen isotopes, trace element geochemistry or U-Th-Pb dating, or laser ablation with quadrupole, or single- or multicollector mass spectrometers, again for trace element chemistry or isotopic ratios of U-Th-Pb or Hf. Multiple analyses on the same zircon grain mean that different regions of single grains are sampled, whereas it would be

advantageous to measure as many elements and isotopes as possible within a single analytical volume, because zircons are rarely homogeneous in all respects. In this application we describe simultaneous measurement of the isotopes of Hf, Th, U, and Pb using laser ablation and two multicollector mass spectrometers, thus providing a direct date for the time of acquisition of the $^{176}Hf/^{177}Hf$ ratio.

Measuring finite volumes using *in situ* analysis allows investigation of complex chemical and chronological zonation within mineral grains. Common *in situ* procedures use two volumes of material by first analyzing U-Pb for dating the sample with either 1) secondary ion mass spectrometry (SIMS) or 2) laser ablation inductively-coupled plasma mass spectrometry (LA-ICPMS), and then analyzing Hf isotopes using LA-ICPMS with a multicollector mass spectrometer. The former places a larger laser spot over a small ion microprobe pit; the latter selects two adjacent sites for laser ablation within an ideally homogenous portion of single crystal as indicated by cathodoluminescence imagery. In both cases, variance in depth of the ablation pit and zone growth may result in the sampling of different chronological and chemical domains. Additionally, correction to initial εHf using CHUR (chondritic uniform reservoir) is age-dependent. Therefore, reported εHf values may be inaccurate if the age is not determined on the same volume, which results in erroneous interpretation of zircon growth. In contrast, simultaneous acquisition uses only one common volume of material.

The first description of simultaneous acquisition of ^{207}Pb and ^{206}Pb measured congruently with Hf used a Thermo Neptune zoom quadrupole lens (Woodhead *et al.*, 2004). Kemp *et al.* (2009) later applied the technique to inherited detrital zircons, inherited igneous zircons, and metamorphosed zircons. However, thermal events post-

dating zircon crystallization, such as in an evolving magma chamber, may induce intra-grain variation in $^{207}Pb/^{206}Pb$ ages (Kemp *et al*., 2009). Identifying discordant grains requires measuring $^{206}Pb/^{238}U$ and $^{207}Pb/^{235}U$. In addition, precision of both Hf and U-Pb measurements is reduced because counting time is divided among Hf measurement, U-Pb measurement, and magnet settling (Woodhead *et al.*, 2004). In 2008, Yuan et al. successfully measured Hf and U-Pb simultaneously on zircons using a laser and two mass spectrometers – a multicollector for Hf isotopes and a single collector for U-Pb. Their laser ablation split stream inductively-coupled mass spectometer (LASS-ICPMS) method has since been developed and employed with great success (Tollstrup *et al.*, 2012; Fisher *et al.*, 2014). In this paper we describe a new technique that utilizes two multicollector instruments in order to provide improved precision in the simultaneous measurement of U-Th-Pb and Hf isotopes.

Methods

Our method consists of connecting two Thermo Finnigan Neptune Plus multicollector mass spectrometers to a single laser ablation system. Following Fisher *et al*. (2014), we use a simplified plastic T connection to split the sample gas evacuated from a 193nm excimer laser sample chamber between the two ThermoFinnigan Neptune Plus multicollector mass spectrometers (Figure 1). The volume of analyte sent to each mass spectrometer is controlled by changing the rate of He carrier gas flow. Precision with this method is equal to or better than previous more complicated configurations (Fisher *et al.*, 2014) that control aerosol volume between mass spectrometers with clamps (Tollstrup *et al*., 2012), gas homogenizers (Yuan *et al.*, 2008; Tollstrup *et al*., 2012),

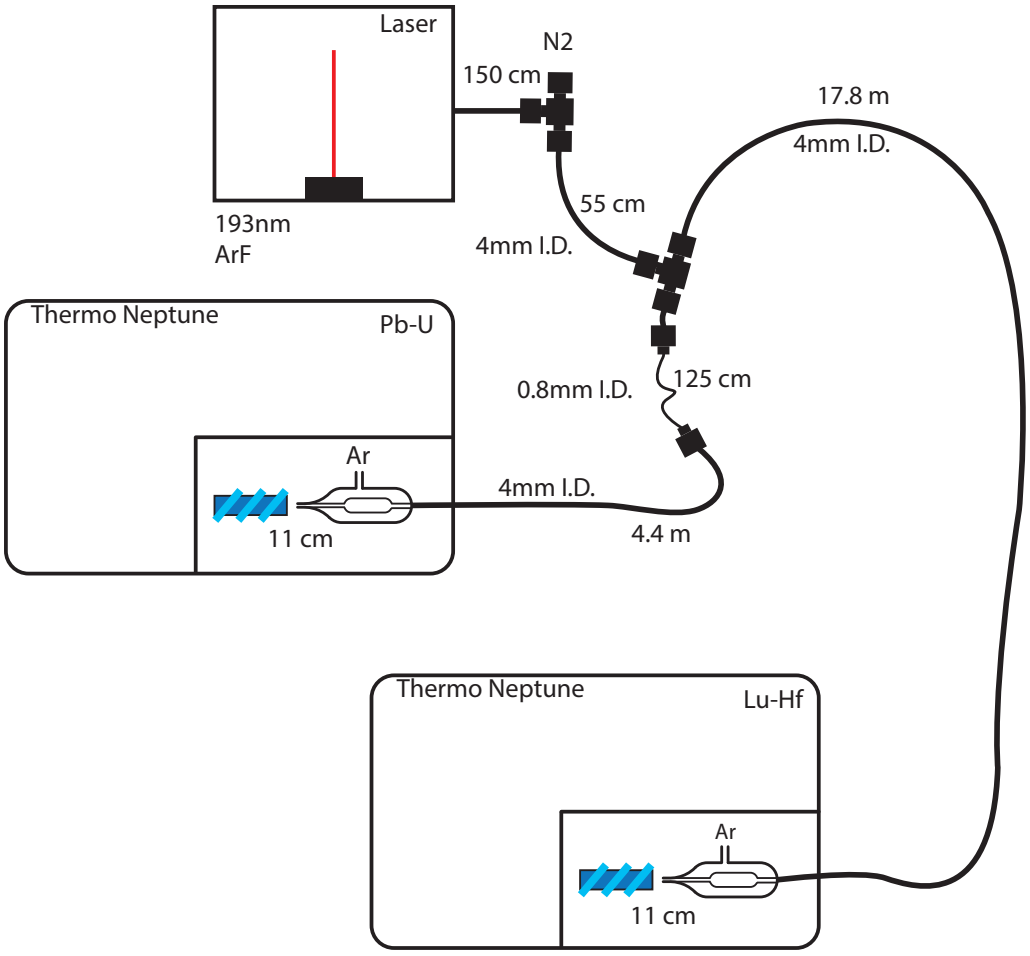

Figure 1. Schematic diagram of the DM-SS-ICPMS setup. See text for more details.

mass flow controllers (Yuan *et al.*, 2008), and baffles (Tollstrup *et al*., 2012).

The use of two ThermoFinnigan Neptunes is unique to this study. Previous split stream studies have measured Lu-Hf isotopes with a multicollector ICPMS, but U-Pb has been measured with either a quadrupole-ICPMS or a single collector-ICPMS (Tollstrup *et al.*, 2012; Fisher *et al*., 2014). Both quadrupole and single collector mass spectrometers rely on a single ion counter where only one mass can be measured at any given moment, and large jumps between ion masses require long magnet settling times. In addition, variable fractionation of U-Pb during analysis requires correction between each sweep. One approach to minimizing the effect of variable fractionation on ^{207}Pb and ^{206}Pb is to take the mean of ^{206}Pb/^{207}Pb ratios for an entire spot analysis (Fisher *et al.*, 2014). However, if a single ablation spot overlaps into an adjacent zone of different age, information on the average within the zone is lost. With multiple Faraday collectors and ion counters available on the Neptune, ^{232}Th, ^{238}U, ^{207}Pb, ^{206}Pb, ^{202}Hg, ^{204}Pb, and ^{208}Pb can be measured simultaneously. A change in either the ^{206}Pb/^{238}Pb ratio or ^{206}Pb/^{207}Pb ratio is seen when laser ablation drills to a new mineral zone and indicates complex growth history in zircons that would have otherwise been averaged with a single-collector mass spectrometer.

The following describes the details of a two-Neptune instrument setup, hereto referred to as Dual Multicollector Laser Ablation Split Stream Inductively-Coupled Plasma Mass Spectrometry (DM-LASS-ICPMS). Characterization of subtle zircon heterogeneity requires minimizing acquisition times while maximizing accuracy and precision of both Hf and U-Pb analysis. To minimize required acquisition times, we optimize parameters including integration times, laser frequency, and laser fluence. We

analyze a variety of commonly used zircon standards for both U-Pb and Hf, including three synthetic zircons (Fisher *et al*., 2011). These standards and synthetic grains represent a large range in concentrations of both U and Yb. U-Pb Ages and $^{176}Hf/^{177}Hf$ ratios are within error of accepted solution values, indicating the technique remains robust even where large interference corrections are necessary.

Analytical Setup

Samples are ablated with a 193 nm ArF excimer laser using a 53 μm spot with a laser frequency of 10 Hz and a laser fluence of 6.11 J/cm^2. A 0.625 L/min flow of He carrier gas in the arm and 0.417 L/min flow of He carrier gas in the cell carry ablated material out of the sample chamber through 4mm inner diameter (ID) teflon tubing. To reduce oxides (Payne *et al*., 2013) carried to the mass spectrometers and stabilize signal intensities, a plastic "T" connection adds 0.005 L/min of N_2 (Iizuka & Hirata, 2005) approximately 150 cm from the laser. Another plastic "T" connection 55 cm from the N_2 addition splits the sample gas into two 4mm ID teflon tubes that lead to each Neptune (Figure 1).

U-Pb Neptune

To increase the pressure gradient to the U-Pb Neptune without the need for excessively long teflon tubes, approximately 5 cm of 4 mm ID teflon tubing is connected with a Swagelok stepdown connector to ~1.25 m of 0.8 mm ID tubing after the "T" split. Another Swagelok stepdown connects this tubing to a 4 mm ID teflon tubing ~4.4 m in length. Ar sample gas is added to sample gas 11 cm from the torch. The U-Pb Neptune is

equipped with standard nickel sample and skimmer cones. Analyzed isotopes are listed in Table 1.

Hf Neptune

After the sample gas is split, ~17.8 m of 4 mm ID teflon tubing carries sample gas to the Hf Neptune located in an adjacent room. Ar sample gas is added 11 cm from the torch, and ablated material passes through a nickel Jet sample cone and an X-skimmer which have been shown to increase Hf signal intensities by a factor of 1.4 (Hu *et al.*, 2012). The Hf Neptune has 9 Faraday cups available with the option of using an ion counter in place of the central Faraday cup. Two cup configurations were employed (Table 2): 1) measures all known Yb isotopes to determine the best Yb correction for our Hf configuration; 2) follows Fisher *et al*. (2014). Comparison of measurements made in both configurations may be found in Results.

Laser Parameters

Laser parameters were chosen to minimize counting times required for ablation while maintaining high precision (~3% error for U-Pb (Kylander-Clark *et al.*, 2013)) and <2 εHf units standard error for ^{176}/Hf/^{177}Hf (Fisher *et al.*, 2014)).

Frequency and Laser Fluence

High laser energies required to ionize Hf resulted in irregular U-Pb fractionation between standards. Inadequate correction of U-Pb fractionation results in spurious ages of standards and therefore calculated ages of analytical unknowns. Laser frequencies were

Table 1. Instrument operating parameters

	Lu-Hf	U-Pb
Model	ThermoFinnigan Neptune	ThermoFinnigan Neptune
Forward Power	1215	1180
Mass Resolution	Low	Low
Gas flows-laser ablation		
Cool/plasma (Ar)	16 L/min	15 L/min
Auxiliary (Ar)	1.00 L/min	0.90 L/min
Sample/nebulizer (Ar)	1.09 L/min	1.34 L/min
Carrier gas (He)	1.1 L/min	1.1 L/min
Nitrogen	5 mL/min	5 mL/min
Laser ablation		
Type	193nm ArF	*Measured Masses*
Repetition rate	10 Hz	^{202}Hg, ^{204}Pb, ^{206}Pb, ^{207}Pb, ^{208}Pb, ^{232}Th, ^{238}U
Laser fluence	6.11 J/cm^2	
Spot size	53 μm	

Table 2. Cup configurations for Lu-Hf

	L4	L3	L2	L1	Axial	H1	H2	H3	H4
Cup Configuration 1		171Yb	172Yb	173Yb	174Yb	175Lu	176Hf	177Hf	179Hf
Cup Configuration 2[1]	171Yb	173Yb	175Lu	176Hf	177Hf	178Hf	179Hf	180Hf	182W

1. After Fisher *et al.* (2014)

chosen to produce a minimum intensity of 2.5 V of ^{179}Hf on the Pleisovice zircon standard which enables a precision of <2 εHf units. We tested frequencies and laser fluence combinations of 6 Hz (7.19 J/cm^2), 8 Hz (6.11 J/cm^2, 6.47 J/cm^2, 6.83 J/cm^2), and 10 Hz (5.03 J/cm^2, 5.39 J/cm^2, 5.75 J/cm^2, 6.11 J/cm^2, 6.47 J/cm^2 energy). A frequency of 10 Hz produced the most stable $^{206}Pb/^{207}Pb$ and $^{206}Pb/^{238}U$ ratios. Between laser fluences of 5.75 J/cm^2 and 6.11 J/cm^2 at 10 Hz, εHf uncertainties were consistently lowest for 6.11 J/cm^2 across standards and unknowns.

Spot Size and Shape

We chose a 53 μm diameter spot over 41 μm or 30 μm, thus sacrificing some spatial resolution, in order to obtain more precise εHf values. Moreover, a larger diameter pit ensures that the aspect ratio of pit depth to diameter is greater than 2:1. Woodhead *et al.* found a ratio less than 2:1 causes contamination of lower ablated material from material above it (2004). Ablation pits from this study were imaged with an FEI Quanta 600 FEG SEM at the University of Utah's Nanofab laboratory (Figure 2). A pit depth of 24 μm is averaged from 10 ablation sites measured via Zygo NewView profilometer also located at the Nanofab laboratory.

Data Reduction

U-Pb Data Reduction

Prior to zircon ablation, intensities of U-Pb are tuned to ~40-60 mV of ^{238}U on the NIST 610 glass standard using a 41 μm spot and laser settings of 6 Hz at a fluence of 3.20 J/cm^2 along a straight line path. Chosen ablation spots are first pre-ablated with 2

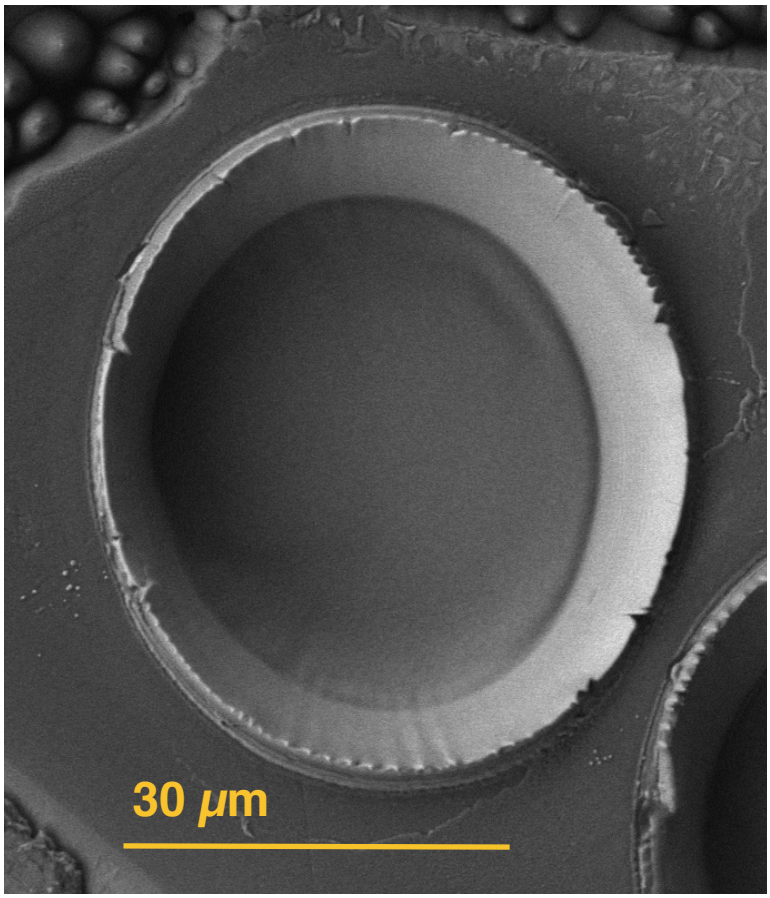

Figure 2. Back-scattered electron image (BSE) of a 53 μm laser ablation pit on the Plešovice zircon standard. Pit is ~20 μm deep.

cleaning shots using the same laser settings as for analysis (Table 1), followed by 35 s of gas blank. Acquisition time totals 40 s. A 6 s waiting period separates acquisition and cleaning shot. Zircon 91500 was chosen as the primary U-Pb standard, with Pleisoviche zircon as the secondary standard. Data are collected in a single file with a 0.131 s integration time.

Data are reduced primarily using Iolite's (version 2.4) U-Pb Data Reduction Scheme (Paton *et al*., 2010). First, baseline is selected during the period of 35 s gas blank measurement 8-15 s prior to the start of acquisition measurements. Using Iolite's "automatic" spline type, baseline is subtracted from all integrations. As data are in a single file, $^{206}Pb/^{238}U$ ratios can be selected from beam intensity for ^{238}U. Age integrations are only considered where both $^{206}Pb/^{238}U$ and $^{206}Pb/^{207}Pb$ ratios are stable. The entire integration time is chosen for the primary standard to ensure proper correction for downhole fractionation. However, only 10-15 s of integration time is required to produce accurate ages, so only the first 20 s of acquisition was considered for other standards. Mean ages and concordia plots are generated with Isoplot (version 3.76.12.02.24).

Lu-Hf Data Reduction

Intensities are tuned to a minimum of 140 mV ^{175}Lu on the NIST 610 glass standard using a 41 μm spot, frequency of 6 Hz, and a fluence of 3.20 J/cm^2 along a straight line path. When properly tuned, intensities are 2-3 V of ^{179}Hf and 7-9 V of ^{180}Hf on the Mudtank standard for cup configurations 1 and 2 (Table 1), respectively. Like others, we find a minimum of ~3-4 V of ^{180}Hf is necessary for high precision $^{176}Hf/^{177}Hf$

ratios (Hu *et al.*, 2012; Tollstrup *et al.*, 2012; Fisher *et al.*, 2014).

To minimize surface contamination, two cleaning shots are fired followed by 35 s of gas blank before ablation. An ablation time of 40 s is used, as it increases the precision of $^{176}Hf/^{177}Hf$ values compared to 30 s of ablation. A gas blank of 6 s precedes the next cleaning shot. Data are collected as a single file with an integration time of 0.131 s. While longer integration times have been used in other ICP-MS studies (Tollstrup *et al.*, 2012; Kylander-Clark *et al.*, 2013; Fisher *et al.*, 2014) and in TIMS work (Nowell *et al.*, 1998), the 0.131 s integration time consistently increases precision across standards compared to 0.262 s, 0.524 s, and 1.049 s integration times (Figure 3).

Data are reduced in Iolite (version 2.4) and normalized to the Plešovice zircon standard. For a detailed description of corrections used in this study, see Fisher *et al.* (2011; 2013) and the references therein. Mass bias of Hf is corrected with the exponential law from a $^{179}Hf/^{177}Hf$ value of 0.7325 (Patchett & Tatsumoto, 1980) and the measured $^{179}Hf/^{177}Hf$. Following Fisher *et al.* (2014), Yb mass bias is corrected using a $^{171}Yb/^{173}Yb$ ratio of 1.13268. We measure only ^{175}Lu, and so the mass bias correction for Yb is used for Lu. There are three critical isotopes with mass 176 – Yb, Lu, and Hf. The correction for ^{176}Yb is made using the $^{176}Yb/^{173}Yb$ ratio measured on synthetic zircons MUNZirc 1, 3, and 4 (Fisher *et al.*, 2011). The $^{176}Yb/^{173}Yb$ ratios in this study are 0.79654 for cup configuration 1 and 0.79675 for cup configuration 2. The correction for ^{176}Lu assumes a $^{176}Lu/^{175}Lu$ value of 0.2656 (Chu *et al.*, 2002).

The 5 L/min of N_2 added to analyte leaving the cell (Figure 1) reduces the formation of $^{160}Gd^{16}O$ (Payne *et al.*, 2013), so no correction is made for $^{160}Gd^{16}O$ interference. Baselines are corrected with Iolite's "automatic" spline type by selecting a

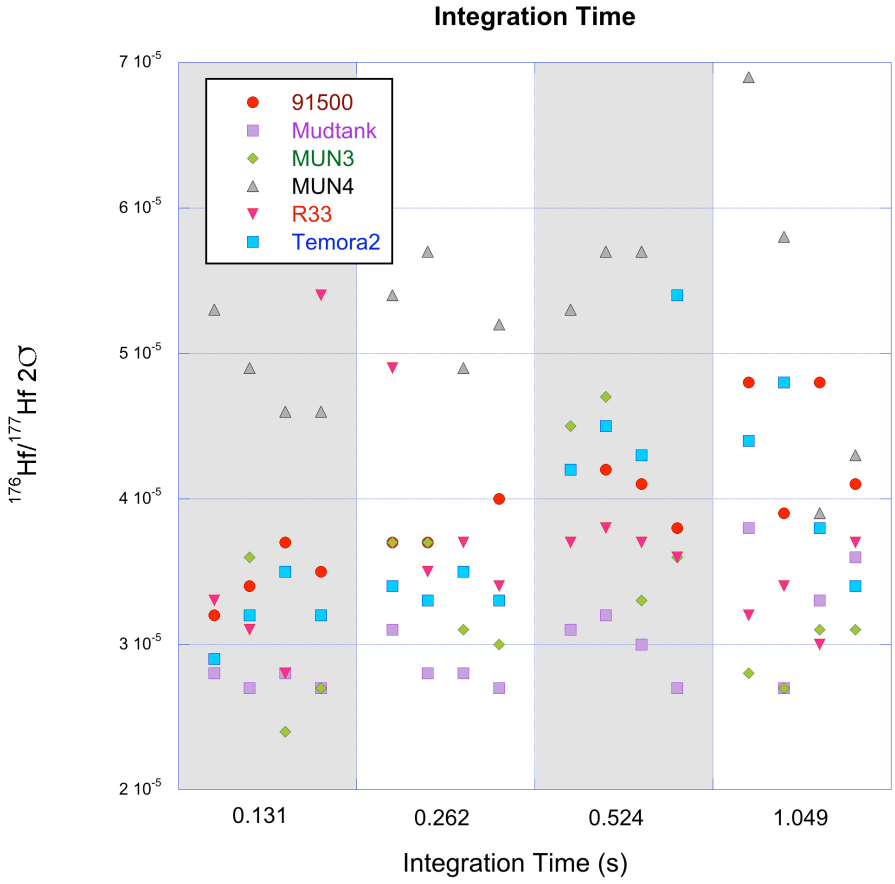

Figure 3. Effects of integration time on $^{176}Hf/^{177}Hf$ ratio precision of zircon standards in this study. Data points are staggered for visibility.

stable 10-15 s of gas blank preceding all ablations and 20-30 s of gas blank at the end of a run. Index channels are ^{179}Hf for cup configuration 1 and 178Hf for cup configuration 2. The unstable ~3 s of ablation signal at beginning and end are trimmed, and integrations are made over the remaining ~34 s of ablation time.

Results

91500

The 91500 standard is a zircon from a syenite pegmatite in Ontario, Canada, that is well characterized for both U-Pb and Lu-Hf composition (Wiedenbeck *et al.*, 1995; Wiedenbeck *et al.*, 2004). We chose 91500 as the primary standard for U-Pb because few to no discordant analyses are reported in other studies (Wiedenbeck *et al.*, 1995; Schoene *et al.*, 2005; Yuan *et al.*, 2008; Fisher *et al.*, 2014). As it is used to normalize all other U-Pb standards, it is not possible to assess the accuracy of U-Pb using DM-LASS-ICPMS method on this zircon.

The mean of ^{176}Hf/^{177}Hf isotope ratios for cup configuration 1 (Table 1) over a period of one month is 0.282300 ± 68 (2σ, n = 91) (Figure 4) with an average internal reproducibility of ~ 1.4 εHf units. One data point was excluded. This is in good agreement with the laser ablation ICPMS value of 0.282307 ± 31 from Wu *et al.* (2006) and the pooled value of 0.282308 ± 6 from Blichert-Toft (2008). The measured ^{176}Hf/^{177}Hf isotope ratio for a single run using cup configuration 2 is 0.282328 ± 23 (2σ, n = 8) with an average internal reproducibility of 1.7 εHf units. This is higher than the value from Blichert-Toft (2008) by 0.7 εHf units, although still within error.

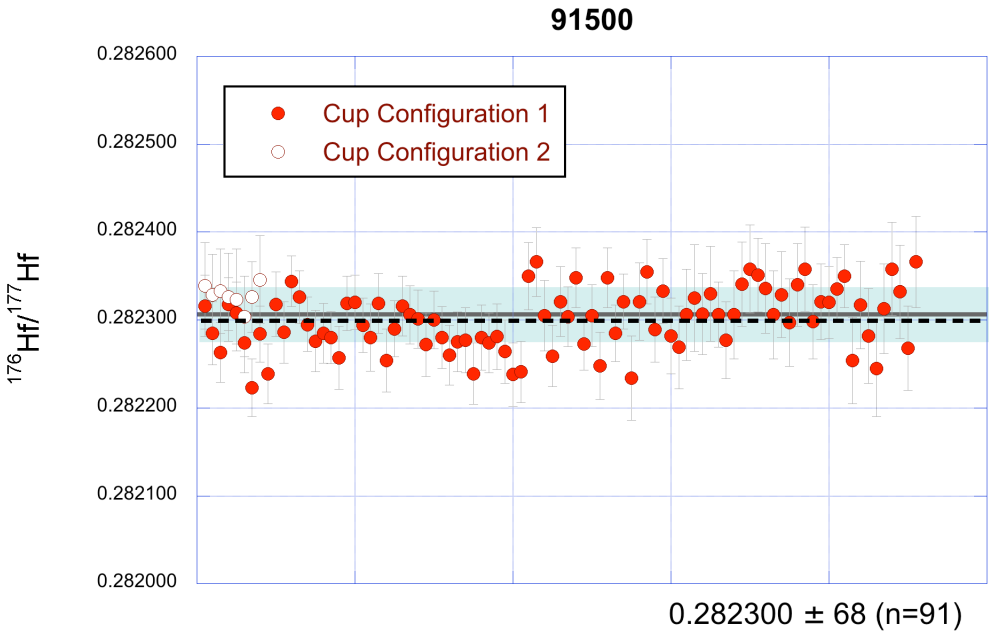

Figure 4. Results of $^{176}Hf/^{177}Hf$ ratios in 91500 for this study. Error bars are given as 2 s.e. The grey bar and green shaded region indicate the accepted literature value and 2 standard deviations (2σ), respectively (Wu *et al.*, 2006). The dashed, black bar represents the reported mean for Cup Configuration 1 with errors given as 2σ.

Mudtank

The Mud Tank standard from the Mud Tank carbonatite in Australia is in abundant supply (Woodhead & Hergt, 2005). Unfortunately for dating purposes, its concentration of U is low (~6.1-36.5 ppm). Large errors associated with low signal intensities can be seen in Run 1 of 3 runs made over one a one-month period (Figure 5A). The resulting weighted mean $^{206}Pb/^{238}U$ age, excluding a single analysis and calculated from the remaining 12, is 727.4 ± 5.7 Ma with a mean standard weighted deviation (MSWD) of 0.88. This is 0.6% lower than the published age of 732 Ma (Black & Gulson, 1978).

The Mud Tank zircons have low REE values making them well suited to monitor raw $^{176}Hf/^{177}Hf$ ratios. Analyses were made on colorless to faintly colored crystals of the Mud Tank standard as Woodhead & Hergt (2005) report heterogeneity in colored grains. Over a period of one month, the mean of $^{176}Hf/^{177}Hf$ isotope ratios for Cup Configuration 1 (Table 1) is 0.282507 ± 60 (2σ, n = 38) with an average internal reproducibility of 1.0 εHf unit (Figure 5B). This is in excellent agreement with the literature LA-ICPMS value of 0.282504 ± 44 (Woodhead & Hergt, 2005). The mean of a single run for cup configuration 2 is 0.282529 ± 36 (2σ, n = 7) with an average internal reproducibility of 1.8 εHf units. This is higher than the value from Woodhead & Hergt (2005) by 0.9 εHf units, although still within error.

MUNZirc 1, 3, 4

MUNZircs 1, 3, and 4 are synthetic zircons developed at the Memorial University of Newfoundland, Canada, to monitor isobaric interference corrections for Hf isosope

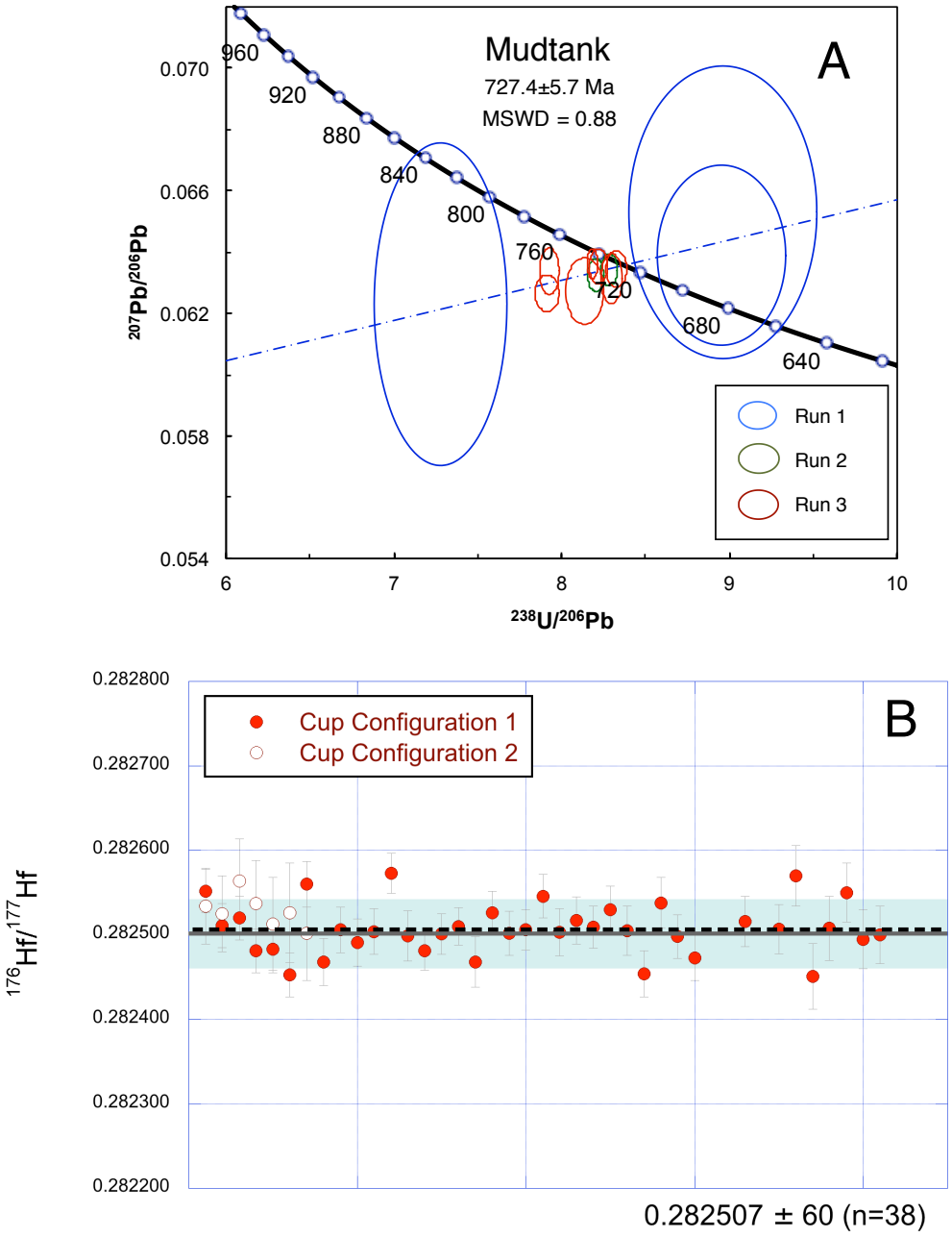

Figure 5. Results of $^{206}Pb/^{238}U$ ages and $^{176}Hf/^{177}Hf$ ratios in this study for the Mudtank zircon. A) Comparison of $^{206}Pb/^{238}U$ ages in Mudtank over multiple runs for this study. Runs were made over a one-month period. Error ellipses are given as 2 standard deviations (2σ). B) Results of $^{176}Hf/^{177}Hf$ ratios in Mudtank for this study. Error bars are given as 2 s.e. The grey bar and green shaded region indicate the accepted literature value and 2 standard deviations (2σ), respectively (Woodhead & Hergt, 2005). The dashed, black bar represents the reported mean for cup configuration 1 with errors given as 2σ.

measurements (Fisher *et al.*, 2011). MUNZirc zircons do not contain U or Pb, and therefore yield no age information. All zircons of the MUNZirc series have homogeneous $^{176}Hf/^{177}Hf$ isotope ratios, but distinctly different REE concentrations. Their value lies in monitoring the accuracy of correcting for ^{176}Yb over a wide range of $^{176}Yb/^{177}Hf$ concentrations (Fisher *et al.*, 2011; Fisher *et al.*, 2014). In particular, MUNZirc 4, with the highest REE content, has a $^{176}Yb/^{177}Hf$ isotope ratio of 0.44, double that of MUNZirc 3 and greatly exceeding that of natural zircons. Though corrections as high of those in MUNZirc 4 are unnecessary for natural zircons, reproducing accurate values for MUNZirc 4 indicates the robustness of correcting for ^{176}Yb even in the most extreme cases.

For Cup Configuration 1, the mean $^{176}Hf/^{177}Hf$ isotope ratio measured over a period of 10 days for MUNZirc 1 and 3 is 0.282133 ± 71 (2σ, n = 30) (Figure 6). One outlier was excluded from analysis of MUNZirc 3. This is in excellent agreement with the literature solution value of 0.282135 ± 31 (Fisher *et al.*, 2011). Including MUNZirc 4 increases the mean $^{176}Hf/^{177}Hf$ isotope ratio in this study to 0.282141 ± 124 (2σ, n = 56). While this number is still in good agreement, the 2σ represents a correction of >4 εHf units. Average internal reproducibility is 0.8 εHf, 1.0 εHf, and 1.8 εHf units for MUNZirc 1, 3, and 4, respectively. For Cup Configuration 2, the mean $^{176}Hf/^{177}Hf$ isotope ratio of a single run is 0.282146 ± 33 (2σ, n = 14) for MUNZirc 1 and 3 and 0.282142 ± 53 (2σ, n = 21) for MUNZirc 1, 3, and 4. These numbers are both in good agreement with Fisher *et al.* (2011) and the 2σ represents a correction of <2 εHf units. Average internal reproducibility is 1.3 εHf, 1.8 εHf, and 3.9 εHf units for MUNZirc 1, 3 and 4, respectively.

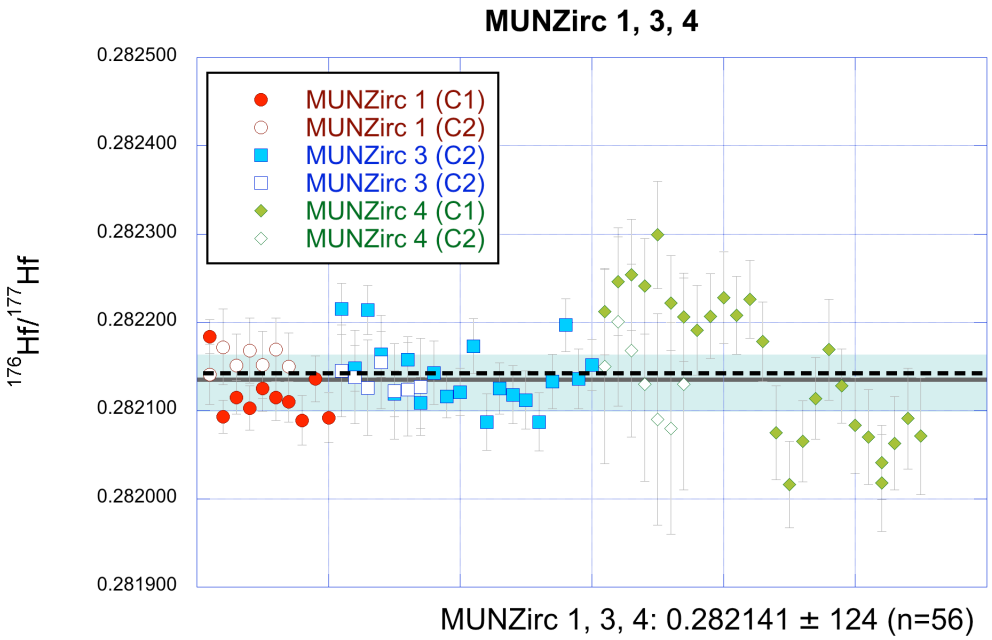

Figure 6. Results of $^{176}Hf/^{177}Hf$ ratios in MUNZirc 1, 3, and 4 for this study. Error bars are given as 2 s.e. The grey bar and green shaded region indicates the accepted literature value and 2 standard deviations (2σ) respectively (Fisher *et al*., 2011). The dashed, black bar represents the reported mean for cup configuration 1 (C1) with errors given as 2σ. See text for more detail.

Plešovice

The Plešovice zircon is from a potassic granulite in the Czech Republic. With high U concentrations (465-3080 ppm) and concordant $^{206}Pb/^{238}U$ ages, the Plešovice zircon is a good secondary standard for U-Pb analysis (Sláma *et al.*, 2008; Cottle *et al.*, 2012; Tollstrup *et al.*, 2012). The weighted mean $^{206}Pb/^{238}U$ age from 72 analyses over a one-month period is 336.3 ± 0.94 Ma (MSWD = 1.3) (Figure 7). Seven analyses proximal to fractures were discarded. When included, the weighted mean $^{206}Pb/^{238}U$ age from 79 analyses is 336.9 ± 1.7 Ma (MSWD = 0.89). Both ages are in excellent agreement with the published ID-TIMS age of 337.13 ± 0.37 Ma (Sláma *et al.*, 2008).

Plešovice was chosen as our primary standard for Hf because of reported homogenous $^{176}Hf/^{177}Hf$ isotope ratios from analyses across multiple laboratories (Sláma *et al*., 2008). All other Lu-Hf standards are normalized to this standard, thus, we are unable to assess the accuracy of measuring $^{176}Hf/^{177}Hf$ using DM-LASS-ICPMS on this zircon.

R33

The R33 zircon standard is from a biotite-hornblende monzodiorite in Vermont, United States with a U concentration of ~148 ppm. However, some grains contain older inherited regions, or are younger due to Pb loss (Black *et al.*, 2004). In addition, SEM images taken postablation show fracturing through several ablation pits and throughout grains of R33. Therefore, we excluded 5 concordant analyses and 2 discordant analyses that lie at ~450 Ma. The remaining 19, taken over a one-month period, give a weighted mean $^{206}Pb/^{238}U$ age of 419.7 ± 4.1 Ma (MSWD = 1.18) (Figure 8A). This is in good

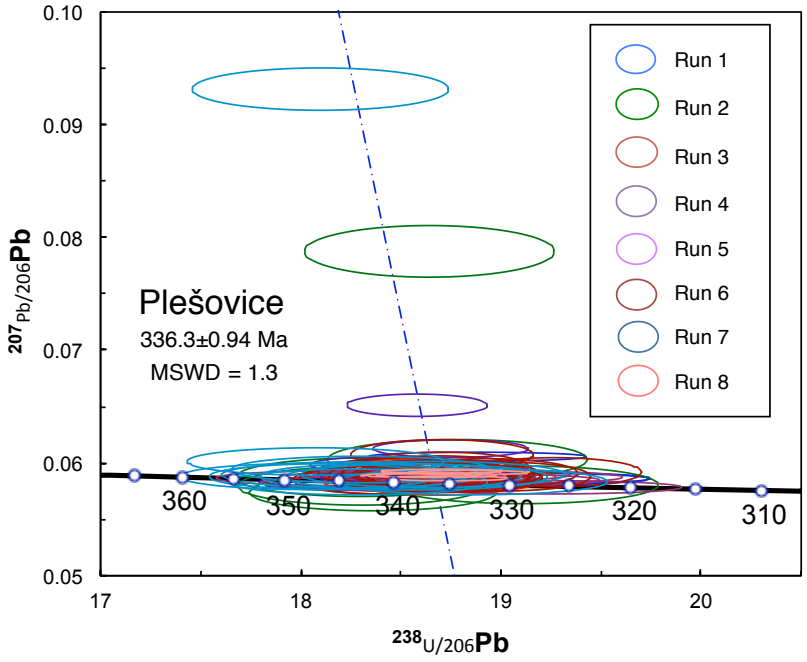

Figure 7. Comparison of $^{206}PB/^{238}U$ ages over multiple runs on the Plešovice standard. Runs were made over a one-month period. Error ellipses are given as 2 standard deviations (2σ).

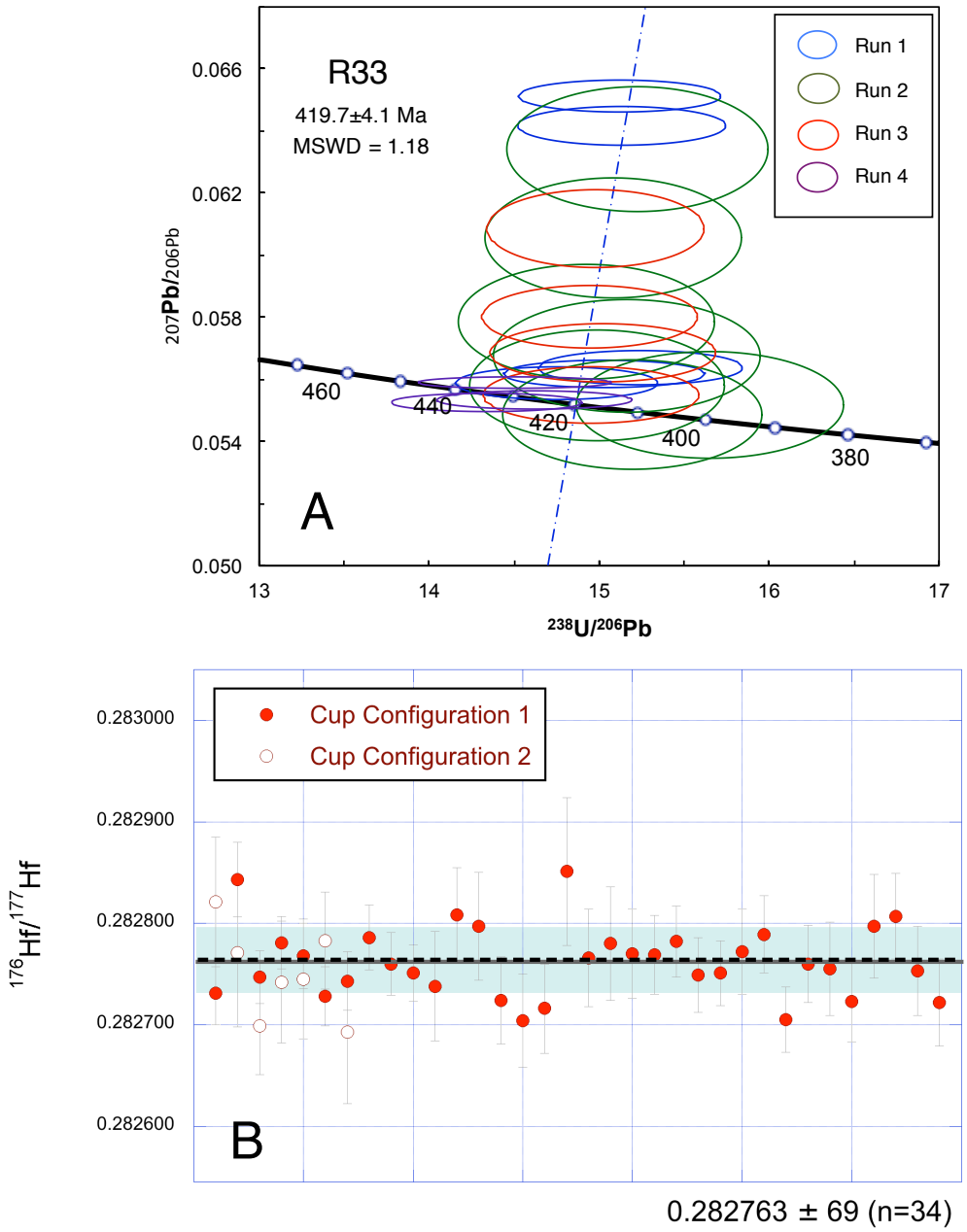

Figure 8. Results of $^{206}Pb/^{238}U$ ages and $^{176}Hf/^{177}Hf$ ratios in this study for the R33 zircon. A) Comparison of $^{206}Pb/^{238}U$ ages in R33 over multiple runs for this study. Runs were made over a one-month period. Error ellipses are given as 2 standard deviations (2σ). B) Results of 176Hf/177Hf ratios in R33 for this study. Error bars are given as 2 s.e. The grey bar and green shaded region indicate the accepted literature value and 2 standard deviations (2σ), respectively (Fisher *et al.*, 2014). The dashed, black bar represents the reported mean for cup configuration 1 with errors given as 2σ.

agreement with the reported ID-TIMS age of 419.26 ± 0.39 Ma (Black *et al.*, 2004).

Of all the natural zircon standards, R33 has the highest $^{176}Yb/^{177}Hf$ and $^{176}Lu/^{177}Hf$ isotope ratios and is thus invaluable for monitoring the application of interference corrections on mass 176 in high REE zircons. The mean of $^{176}Hf/^{177}Hf$ isotopes for one-month of measurements for cup configuration 1 is 0.282763 ± 69 (2σ, n = 34) with an average internal reproducibility of 1.4 εHf units. This is in excellent agreement with the literature value 0.282764 ± 14 (Fisher *et al.*, 2014). A single analysis with erroneously high internal error (>2 εHf units) was discarded. For Cup Configuration 2, the mean is 0.282751 ± 85 (2σ, n = 7) with an internal reproducibility of 2.1 εHf units. The mean is lower than the accepted value by 0.5 εHf units, but still in good agreement.

Temora-2

Temora-1 and Temora-2 are from a gabbroic diorite in Eastern Australia, though Temora-2 shows more deuteric alteration (Black *et al.*, 2004). The weighted mean $^{206}Pb/^{238}U$ age from 19 analyses taken over a one-month period is 431 ± 12 (MSWD = 1.17) (Figure 9A). This is 3.4% higher than the literature ID-TIMS value 416.8 ± 0.33 Ma (Black *et al.*, 2004).

Published $^{176}Hf/^{177}Hf$ ratios for Temora-2 vary between 0.282672 and 0.28706 (Woodhead *et al.*, 2005; Wu *et al.*, 2006; Yuan *et al.*, 2008; Kemp *et al.*, 2009). In addition, possible heterogeneity has been reported in Temora-1 (Fisher *et al.*, 2014) and due to similar formation histories, may also be present in Temora-2. The mean $^{176}Hf/^{177}Hf$ isotope ratio for Temora-2 using Cup Configuration 1 is 0.282710 ± 81 (2σ, n = 40). The mean for Cup Configuration 2 is 0.282687 ± 35 (2σ, n = 7) with an average

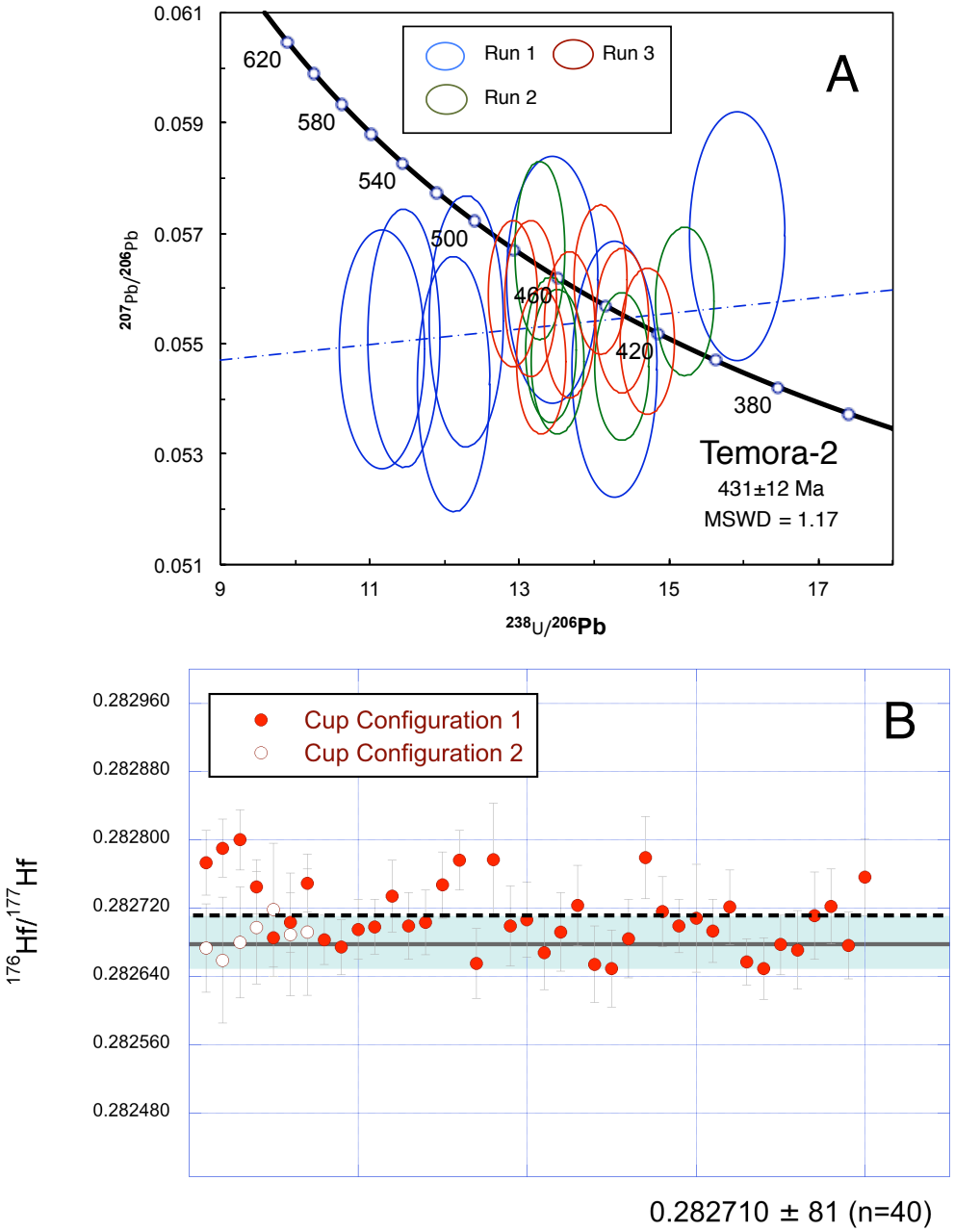

Figure 9. Results of $^{206}Pb/^{238}U$ ages and $^{176}Hf/^{177}Hf$ ratios in this study for the Temora-2 zircon. A) Comparison of $^{206}Pb/^{238}U$ ages in Temora2 over multiple runs for this study. Runs were made over a one-month period. Error ellipses are given as 2 standard deviations (2σ). B) Results of $^{176}Hf/^{177}Hf$ ratios in Temora2 for this study. Error bars are given as 2 s.e. The grey bar and green shaded region indicate the accepted literature value and 2 standard deviations (2σ), respectively (Wu *et al.*, 2006). The dashed, black bar represents the reported mean for cup configuration 1 with errors given as 2σ.

internal reproducibility of 2.4 εHf units (Figure 9B). These are both in good agreement with literature values for Temora-2, and the value from Cup Configuration 2 is nearly identical to the literature value 0.282686 ± 8 of Woodhead *et al.* (2005).

Discussion

Analysis of standards using the DC-LASS-ICMPS method yields $^{206}Pb/^{238}U$ ages and $^{176}Hf/^{177}Hf$ ratios within error for all standards except Temora-2 and MUNZirc 4. Postablation examination of the Temora-2 standard shows no exceptionally fractioned regions or anomalous pit shapes. The 431 Ma age in this study is therefore either 1) analytically induced error or 2) real grain-to-grain heterogeneity within Temora-2. Age heterogeneity is not reported for Temora-1 or Temora-2 (Black *et al.*, 2004; Yuan *et al.*, 2008; Tollstrup *et al.*, 2012; Fisher *et al.*, 2014), so analytical error is the more probable cause. While offset towards lower ages have been reported for laser ablation measurements of Temora-2 on an Agilent 7500 (Black *et al.*, 2004), we see an offset towards higher values. A possible source of analytical error lies in the high frequency and laser fluence needed to ionize Hf in zircons. Other split-stream studies have analyzed Temora-1 with similar parameters (Yuan *et al.*, 2008; Tollstrup *et al.*, 2012; Fisher *et al.*, 2014), but none have used Temora-2 and a ThermoFinnigan Neptune Plus for U-Pb analysis. In this study, we found the baseline and downhole-fractionation-corrected $^{238}U/^{206}Pb$ ratio of Temora-2 was erratic compared to other standards. Therefore, the zircon standard 91500 is an unreasonable model for downhole fractionation of Temora-2 at the laser energies and fluences in this study and may be responsible for elevated ages.

External error of Lu-Hf analysis for Temora-2 using Cup Configuration 1 is the

greatest (~2.9 εHf units) of the natural zircon standards measured in this study. As the $^{176}Yb/^{177}Hf$ ratio in Temora-2 is much lower than that of the accurately measured R33, this discrepancy is not a result of improper interference corrections. Like Fisher *et al*., we suggest the error is due to heterogeneity in Temora-2 (2014). Analyses in this study show two populations (Figure 10). The first and largest population has a $^{176}Hf/^{177}Hf$ ratio of ~0.282690, which is in close agreement with the value of Woodhead *et al.* (2005). The second population is much smaller and has a $^{176}Hf/^{177}Hf$ ratio of ~0.28770. If only scantly analyzed, this population of Temora-2 might produce the large errors seen without largely affecting the accuracy of the calculated mean $^{176}Hf/^{177}Hf$ ratio.

Of the three synthetic standards, MUNZirc 4 shows the greatest range of error and poorest external reproducibility. We attribute this to improper correction for ^{176}Yb. The synthetic zircons have increasing $^{176}Yb/^{177}Hf$ concentrations of 0.06, 0.22, and 0.44 for MUNZirc 1, 3, and 4, respectively (Fisher *et al.*, 2011). The correction for ^{176}Yb in MUNZirc 4 represents 10,000 εHf units (Fisher *et al.*, 2014), so even small variations in intensities of ^{176}Yb may cause erroneous internal and external errors. The ~20 m distance from laser ablation to the Lu-Hf Neptune (Figure 1) may exacerbate irregularity in analyte flow from laser pulses. As the Lu-Hf Neptune cannot be moved closer, a gas mixing bulb could be employed ~20 cm from the addition of Ar sample gas to homogenize gas flows before analysis.

Conclusions

The DC-LASS-ICPMS method can accurately measure U-Th-Pb and Lu-Hf isotopes for zircon samples as long as 1) the U-Pb standards properly correct for

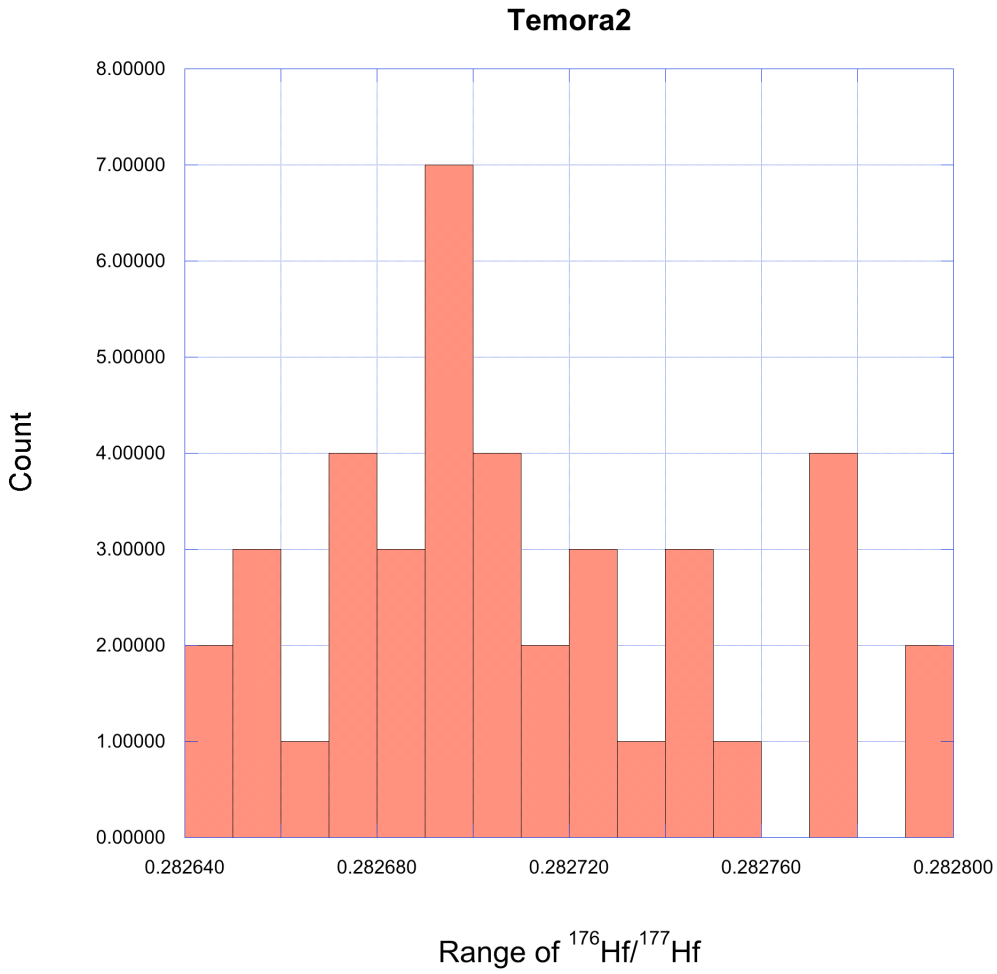

Figure 10. Histogram of $^{176}Hf/^{177}Hf$ ratios for the Temora2 standard showing grain heterogeneity.

downhole fractionation in the unknowns, and 2) the $^{176}Yb/^{177}Hf$ ratios are less than or equal to those of the natural zircon standard R33. A case study testing the DM-LASS-ICPMS method on the zircons of the Yellowstone Snake River Plain can be found in Chapter 2. Further work needs to be done to improve the analytical setup to fully correct for $^{176}Yb/^{177}Hf$ at very high REE concentrations.

References

Black, L. P. & Gulson, B. L. (1978). The age of the Mud Tank Carbonitite, Strangways Range, Northern Territory. *BMR Journal of Australian Geology & Geophysics* **3**, 227-232.

Black, L. P., Kamo, S. L., Charlotte, M. A., Davis, D. W., Aleinikoff, J. N., Valley, J. W., Mundil, R., Campbell, I. H., Korsch, R. J., Williams, I. S., Foudoulis, C. (2004). Improved 206Pb/238U microprobe geochronology by the monitoring of a trace-element-related matrix effect; SHRIMP, ID–TIMS, ELA–ICP–MS and oxygen isotope documentation for a series of zircon standards. *Chemical Geology* **205**, 115-140.

Blichertt-Toft, J. (2008). The Hf isotopic composition of zircon reference material 91500. *Chemical Geology* **253**, 252-257.

Chu, N., Taylor, R.N., Chavagnac, V., Nesbitt, R.W., Boella, R.M., Milton, J.A., German, C.R., Bayon, G., Burton, K., (2002). Hf isotope ratio analysis using multicollector inductively coupled plasma mass spectrometry: an evaluation of isobaric interference corrections. *Journal of Analytical Atomic Spectrometry* **17**, 1567–1574.

Cottle, J. M., Kylander-Clark, A. R., Vrijmoed, J. C. (2012). U–Th/Pb geochronology of detrital zircon and monazite by single shot laser ablation inductively coupled plasma mass spectrometry (SS-LA-ICPMS). *Chemical Geology* **332-333**, 136-147.

Fisher, C. M., Hanchar, J. M., Samson, S. D., Dhuime, B., Blichert-Toft, J., Vervoort, J. D., Lam, R. (2011). Synthetic zircon doped with hafnium and rare earth elements: A reference material for in situ hafnium isotope analysis. *Chemical Geology* **286**, 32-47.

Fisher, C. M., Vervoort, J. D., Dufrane, S. A. (2014). Accurate Hf isotope determinations of complex zircons using the ‘‘laser ablation split stream’’ method. *Geochemistry, Geophysics, Geosystems* **15**, doi: 10.1002/2013GC004962.

Hoskin, P. W. O, Schaltegger, U. (2003). The composition of zircon in igneous and metamorphic petrogenesis. In: Hanchar, J. M., Hoskins, P. W. O (Eds). *Zircon: Reviews in Mineralogy and Geochemistry* **53**, 27-62.

Hu, Z., Liu, Y. Gao, S., Lui, W., Zhang, W., Tong, X., Lin, L., Zong, K., Li, M., Chen, H., Zhou, L., Yang, L. (2012). Improved in situ Hf isotope ratio analysis of zircon using newly designed X skimmer cone and jet sample cone in combination with the addition of nitrogen by laser ablation multiple collector ICP-MS. *Journal of Analytical Atomic Spectrometry* **27**, 1391-1399.

Iizuka, H. & Hirata, T. (2005). Improvements of precision and accuracy in in situ Hf isotope microanalysis of zircon using the laser ablation-MC-ICPMS technique. *Chemical Geology* **220**, 121-137.

Kemp, A. I. S., Foster, G. L., Scherstén, A., Whitehouse, M. J., Darling, J., Storey, C. (2009). Concurrent Pb–Hf isotope analysis of zircon by laser ablation multicollector ICP-MS, with implications for the crustal evolution of Greenland and the Himalayas. *Chemical Geology* **261**, 244-260.

Kinney, P. D. & Maas, R. (2003). Lu-Hf and Sm-Nd isotopes in zircon. *Zircon: Reviews in Mineralogy and Geochemistry* **53**, 327-341.Kylander-Clark, A. R. C., Hacker, B. R., Cottle, J. M. (2013). Laser-ablation split-stream ICP petrochronology. *Chemical Geology* **345**, 99-112.

Nowell, G. M., Kempton, P. D., Noble, S. R., Fitton, J. G., Saunders, A. D., Mahoney, J. J., Taylor, R. N. (1998). High precision Hf isotope measurements of MORB and OIB by thermal ionisation mass spectrometry: insights into the depleted mantle. *Chemical Geology* **149**, 211-233.

Patchett, P. J. & Tatsumoto, M. (1980). A Routine High-Precision Method for Lu-Hf Geochemistry and Chronology. *Contributions to Mineralogy and Petrology* **75**, 263-267.

Paton, C., Woodhead, J. D., Hellstrom, J. C., Hergt, J. M., Greig, A., Maas, R. (2010). Improved laser ablation U!Pb zircon geochronology through robust downhole fractionation correction. *Geochemistry, Geophysics, Geosystems* **11**, Q0AA06, doi:10.1029/2009GC002618.

Payne, J. L., Pearson, N. J., Grant, K. J., Halverson, G. P. (2013). Reassessment of relative oxide formation rates and molecular interferences on in situ lutetium–hafnium analysis with laser ablation MC-ICP-MS. *Journal of Analytical Atomic Spectrometry* **28**, 1068-1079.

Sláma, J., Košler, J., Condon, D. J., Crowley, J. L., Gerdes, A., Hanchar, J. M., Horstwood, M. S. A., Morris, G. A., Nasdala, L., Norberg, N., Schaltegger, U., Schoene, B., Tubrett, M. N., Whitehouse, M. J. (2008). Plešovice zircon — A new natural reference material for U–Pb and Hf isotopic microanalysis. *Chemical Geology* **249**, 1-35.

Stearns, M.A., Hacker, B.R. Ratschbacher, L., Rutte, D., Kylander-Clark, A.R.C. (2015). *Titanite petrocrhonology of the Pamir gneiss domes: Implications for middle to deep crust exhumation and titanite closure to Pb and Zr diffusion* **34**, 784-802.

Tollstrup, D. L., Xie, L., Wimpenny, J. B., Chin, E., Lee, C., Yin, Q. (2012). A trio of laser ablation in concert with two ICP-MSs: Simultaneous, pulse-by-pulse determination of U-Pb discordant ages and a single spot Hf isotope ratio analysis

in complex zircons from petrographic thin sections. *Geochemistry, Geophysics, Geosystems* **13**, Q03017, doi: 10.1029/2011GC004027.

Wiedenbeck, M., Allé, P., Corfu, F., Griffin, W. L., Meier, M., Oberli, F., Quadt, A. V., Roddick, J. C., Spiegel, W. (1995). Three Natural Zicron Standards for U-Th-Pb, Lu-Hf, Trace Element, and REE analysis. *Geostandards Newsletter* **19**, 1-23.

Wiedenbeck, M., Hanchar, J. M., Peck, W. H., Sylvester, P., Valley, J., Whitehouse, M., Kronz, A., Morishita, Y., Nasdala, L., Fiebig, J., Franchi, I., Girard, J.-P., Greenwood, R. C., Hinton, R., Kita, N., Mason, P. R. D., Norman, M., Ogasawara, M., Piccoli, P. M., Rhede, D., Satoh, H., Schulz-Dobrik, B., Skår, Ø., Spicuzza, M. J., Terada, K., Tindle, A., Togashi, S., Vennemann, T., Xie, Q., Zheng, Y.-F. (2004). Further characterization of the 91500 Zircon Crystal. *Geostandards and Geoanalytical Research* **28**, 9-39.

Woodhead, J., Hergt, J., Shelley, M., Eggins, S., Kemp, R. (2004). Zircon Hf-analysis with an excimer laser, depth profiling, ablation of complex geometries, and concomitant age estimation. *Chemical Geology* **209**, 121-135.

Wu, F., Yang, Y., Xie, L., Yang, J., Xu, P. (2006). Hf isotopic compositions of the standard zircons and baddeleyites used in U–Pb geochronology. *Chemical Geology* **234**, 105-126.

Yuan, H., Gao, S., Dai, M., Zong, C., Günther, D., Fontaine, G. H., Liu, X., Diwu, C. (2008). Simultaneous determinations of U–Pb age, Hf isotopes and trace element compositions of zircon by excimer laser-ablation quadrupole and multiple-collector ICP-MS. *Chemical Geology* **247**, 100-118.

CHAPTER II

APPLICATION OF THE DUAL MULTICOLLECTOR LASER ABLATION SPLIT STREAM ICPMS METHOD TO MEASURE Hf, U, Th, AND Pb ISOTOPES IN RHYOLITES OF THE YELLOWSTONE HOTSPOT

Introduction

The Bruneau-Jarbidge volcanic center, located in the Yellowstone Snake River Plain, is well suited for application of the dual multicollector laser ablation split stream ICPMS (DM-LASS-ICPMS) method. Two recent studies by Cathey *et al.* (2011) and Seligman (2012) use *in situ* analysis to measure oxygen isotope ratios and U-Th-Pb ages in zircons separated from rhyolite tuffs and lavas. Cathey *et al.* found $\delta^{18}O$ of tuffs ranged -3.0 to 6.4 ‰ (2011) and averaged ~1.0 ‰, while Seligman found the $\delta^{18}O$ of lavas ranged -3.4 to 8.1 ‰ and averaged 1.5 ‰ (2012). To date, the Bruneau-Jarbidge volcanic center is the largest recorded low $\delta^{18}O$ volcanic province (Boroughs et al., 2005; Cathey et al., 2007; Seligman, 2012), indicating magma origination from a hydrothermally altered crustal protolith. However, there is still discrepancy in the literature between eruption ages of Bruneau-Jarbidge tuffs and lavas. For example, the Triguero Homestead rhyolite was first estimated stratigraphically to be between 9.5-10 Ma (Bonnichsen, 2008) and later found to be 10.52 Ma using $^{206}Pb/^{238}U$ (Seligman, 2012). In this study, we use DM-LASS-ICMPS to measure temporal variation of Hf within zircon on the same collection of zircons analyzed by Seligman (2012). As some ablation sites in this study are congruent to U-Pb ablation sites from the oxygen studies, we can compare the precision of U-Th-Pb ages obtained with ICPMS techniques in this study to ion microprobe techniques. We choose to analyze hafnium geochemistry as a compliment to oxygen geochemistry because mantle and crustal rocks have distinctive Hf isotope signatures (Kinney & Maas, 2003). Therefore, the temporal variation in contribution of crustal and mantle components to magmas of the Yellowstone Volcanic Province can be discerned from the variation of hafnium isotopes in zircons.

Geologic Setting

The production of voluminous rhyolite magmatism associated with the Yellowstone hotspot began contemporaneously with the eruption of the Columbia River Flood Basalts (CRB) ~16 Ma ago in Eastern Oregon (Camp & Ross, 2004). The track of the hotspot is marked by a series of eruptive centers with the most recent being located on the Yellowstone volcanic plateau. Each center was active for 2-4 m.y. with explosive events recurring every 200-300 ka. Of an estimated 142 explosive events, eruption volumes range from 250 to 600 km^3 and larger volume eruptions are characterized by higher magma temperatures (Perkins & Nash, 2002; Nash *et al.*, 2006; Bonnichsen *et al.*, 2008). The unusually high rhyolite temperatures and eruption volumes lead to a new classification of volcanics, termed "Snake River (SR)-type" volcanism by Branney *et al*. (2008). Both plume and nonplume mechanisms have been proposed to explain the high heat flow and space required to form these large igneous provinces. A summary of each mechanism can be found in the review of the central Snake River Plain (CSRP) by Ellis *et al.* (2013) and the references therein. We conclude, however, that the thermal source of Yellowstone Snake River Plain (YSRP) volcanism is consistent with a hotspot plume model. Rhyolite formation in the YSRP originates from both crustal melting and integration of mantle-derived basalts, however the contributions of each are poorly constrained. Previous εNd isotopic studies by Nash *et al.* (2006) estimate a minimum mantle contribution between 20-40%, although the crustal contribution varies spatially. Magmas west and east of the 0.704 and 0.706 Sr isopleths respond to differences in the lithospheric basement of Mesozoic plutonic rocks and Precambrian crust, respectively (Leeman, 1992) (Figure 11).

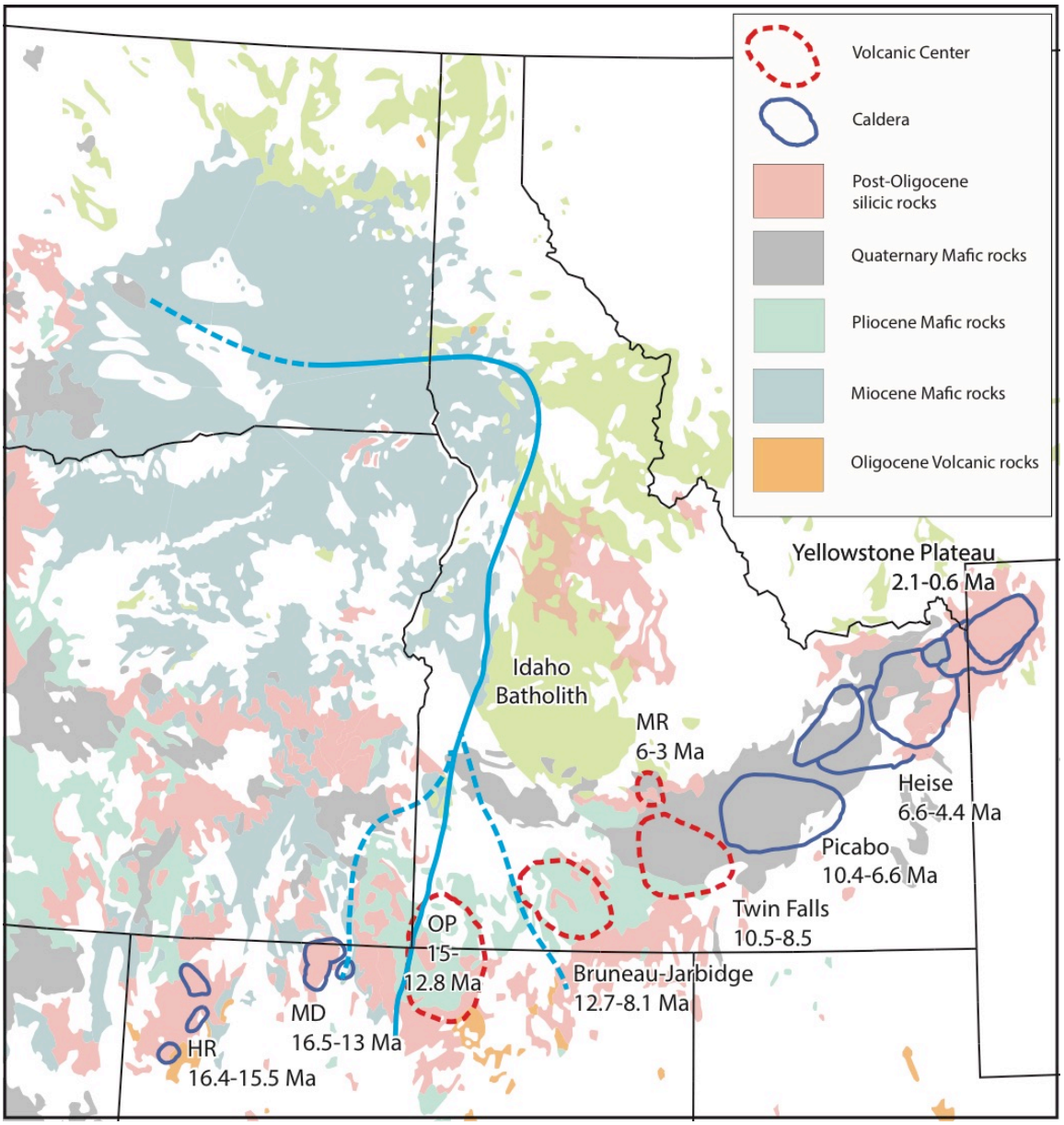

Figure 11. Map showing the track of the Yellowstone Snake River Plain. Initials stand for High Rock caldera complex (HR), McDermitt volcanic field (MD), Owyhee-Humboldt volcanic field (OP), and Magic Reservoir (MR). The 0.704 Sr isopleth is shown in blue. Transitional lithosphere is located between the dashed blue lines in the southern part of the map. $^{87}Sr/^{86}Sr$ ratios ≤ 0.704 attributed to Mesozoic plutonic rocks lie west of the transition and $^{87}Sr/^{86}Sr$ ratios ≥ 0.706 attributed to Archean basement lie east of the transition (Leeman *et al.*, 1992). Map from Eric Christiansen (personal communication). Strontium isopleth locations compiled from Leeman & Manton (1971), Leeman *et al.* (1992), Manduca *et al.* (1992), and Shoemaker & Hart (2002).

Bruneau-Jarbidge

The Bruneau-Jarbidge Volcanic Province (BJVP) encompasses a heightened period of silicic magmatism (13.0-8Ma) in the Yellowstone - Snake River Plain system with a mean recurrence interval of 250ka (Perkins & Nash, 2002; Cathey & Nash, 2004) and an estimated total eruptive volume of 7,000–10,000 km^3 (Perkins & Nash, 2002; Bonnichsen *et al*., 2008) with lavas composing 15% of the estimated volume. BJVP volcanic activity can be divided into two phases: 1) the production of ash-flow tuffs during explosive volcanism between 12.7 and 10.5 Ma followed by 2) the eruption of rhyolite lavas during effusive volcanism between ~10 and 8.1 Ma (Cathey & Nash, 2004; 2009). Pre-eruptive temperatures of the BJVP are in the 900-1000°C range, and they commonly exceed 950°C in both tuffs and lavas (Cathey & Nash, 2004; Cathey & Nash, 2009). High pressure and temperature melting experiments indicate that magmas from the BJVP formed at pressures of 300-400 MPa and with low water contents of < 1.5 % by weight (Almeev *et al*., 2012). The BJVP constitutes the largest known low $\delta^{18}O$ volcanic center known as shown in feldspars (Boroughs *et al*., 2005), quartz (Cathey *et al.*, 2007), and zircon (Seligman, 2012).

Units of the BJVP were first described by Citron (1976) and later by Bonnichsen and Citron (1982). Currently, there are 8 described tuffs and at least 13 rhyolite lavas. Tuffs are designated by roman numerals III, V, VII, IX, X, XI, XIII, and XV from oldest to youngest and collectively are assigned to the Cougar Point Tuff (CPT). Previous work by Bonnichsen *et al.* provides $^{40}Ar/^{39}Ar$ eruption ages for most of the tuffs and lavas. Additional constraints are provided by ion microprobe measurements of $^{206}Pb/^{238}U$ ages in zircons for both CPT units (Cathey *et al.*, 2011) and lavas (Seligman, 2012). In this

study, we analyze zircons from CPT X and 4 lava flows (Table 3) for Lu-Hf and U-Th-Pb isotopes.

Lu-Hf System

The usefulness of the Lu-Hf system lies in the β-decay of ^{176}Lu to ^{176}Hf. The evolution of the Lu-Hf system is evaluated by taking the ratio of the daughter ^{176}Hf isotope and the stable ^{177}Hf isotope. This ratio is then normalized to the chondritic uniform reservoir (CHUR) (Bouvier *et al.*, 2008). Deviation from the $^{176}Hf/^{177}Hf$ of chondrites, assumed to be the initial $^{176}Hf/^{177}Hf$ ratio of Earth, is given as εHf, where the bulk Earth value = 0. As the heaviest REE, Lu is more incompatible in melts than Hf. During a melting event in the mantle, Lu is relatively depleted in the melt and enriched in the mantle. Positive εHf indicates Lu enrichment (mantle-derived melts) and negative εHf indicates depletion of Lu (crust-derived melts) (Figure 12). Zircon contains between 0.5-2 weight % HfO_2, making it ideal for analysis of $^{176}Hf/^{177}Hf$ isotope ratios (Hoskin & Schaltegger, 2003). In addition, zircons are highly resistant to resorption and melting, and multiple magmatic events may result in new zircon growth around earlier formed zircons. In this way, zircons not only preserve the initial $^{176}Hf/^{177}Hf$ isotope ratios during formation, but also may have several zones of growth, each with its own εHf signature that provides a record of magmatic processes. This temporal variation in $^{176}Hf/^{177}Hf$ is accessible using *in situ* methods such as laser ablation or ion-microprobe. As indicated by complex geochemistry (Nash *et al.*, 2002) and oxygen isotopes (Cathey, 2011; Seligman, 2012), volcanic rocks erupted from the Yellowstone Snake River Plain offer an opportunity to piece together coupled interactions between mantle and crust. Though the

Table 3. Summary of analyzed samples

Unit	Sample	Type	Eruption Age (Ma)	Range $\delta^{18}O$ ‰	
				Low	High
Cougar Point Tuff Unit X	95-CPT-CP-39	Tuff	11.45[1], 10.9±0.27[2]	-1.0	1.0
Lower lava flow	11-ULF/BR-02	Lava	10.93±0.23[3]	0.0	2.0
Upper lava flow	10-ULF/BR-02	Lava	10.89±0.25[3]	-3.1	1.5
Triguero Homestead rhyolite	08-THR/THT-02	Lava	9.5-10[4], 10.52±0.13[3]	-1.0	1.6
Marys Creek rhyolite	01-MCR-02	Lava	~11[4], 10.29±0.2[3]	-1.1	3.1

Values of $\delta^{18}O$ for tuffs and lavas are from Cathey (2011) and Seligman (2012) respectively.

1. (Perkins and Nash, 2002)
2. $^{206}Pb/^{238}U$ Age (Cathey, 2011)
3. $^{206}Pb/^{238}U$ Age (Seligman, 2012)
4. Estimated from stratigraphy (Bonnichsen, 2008)

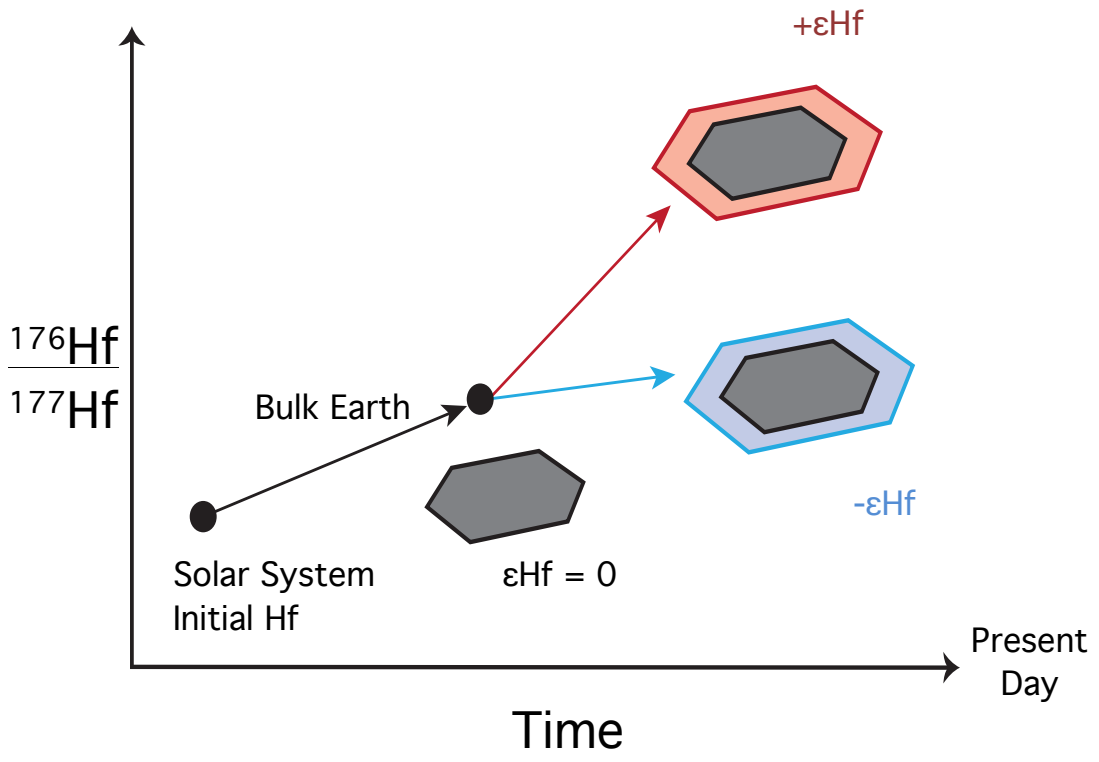

Figure 12. Schematic diagram of the evolution of the $^{176}Hf/^{177}Hf$ ratio in the earth over time. The black arrow indicates increase in the bulk earth ratio of $^{176}Hf/^{177}Hf$ due to the decay of 176Lu. The red and blue arrows represent trends of the $^{176}Hf/1^{77}Hf$ ratio post mantle-melting in the mantle and crust, respectively. See text for more details. Modified after Kinney & Maas (2003).

thermal source for the YSRP is constrained to the mantle, the Bruneau-Jarbidge volcanic center lies within transitional lithosphere (Figure 11). Potential crustal sources include Mesozoic plutonic rocks, Archean basement, Proterozoic and Mesozoic mid-upper crust, previously emplaced YSRP magmas, and coeval basalts (Figure 13).

Methods

Zircons in this study were mounted in two epoxy plugs previous to this study. For the detailed procedure, see Cathey *et al.* (2007) for CPT zircons and Seligman (2012) for BJ lava zircons. Zircon standards Mudtank and Plešovice were added to the mounts by drilling a continuous pit parallel to samples, remaining within 5 mm of the mount center. Standards were covered by a thin film of epoxy before the both mounts were reground and polished until flat. Before analysis, zircons with well-defined domains were located in cathodoluminescence (CL) images taken in previous studies (Cathey 2011; Seligman, 2012). To assess zircon heterogeneity, ablation sites were chosen on cores, rims, and mantles (defined as any site between core and rim). Where possible, multiple ablations were made in a single CL zone to assess reproducibility of $^{176}Hf/^{177}Hf$ ratios and $^{206}Pb/^{238}U$ ages. Additional ablation sites were chosen between prior oxygen and U-Pb analysis pits to compare U-Pb ages with previous studies (Cathey 2011; Seligman, 2012) (Figure 14). U-Pb and Lu-Hf isotopic ratios in zircons were simultaneously measured using the Dual Multicollector Laser Ablation Split Stream ICPMS (DM-LASS-ICPMS) method developed at the University of Utah. The U-Pb standard 91500 and the Lu-Hf standard Plešovice were measured every 6 unknowns. Mudtank zircon was analyzed every 12 unknowns in order to monitor instrument drift and sensitivity. Synthetic zircons

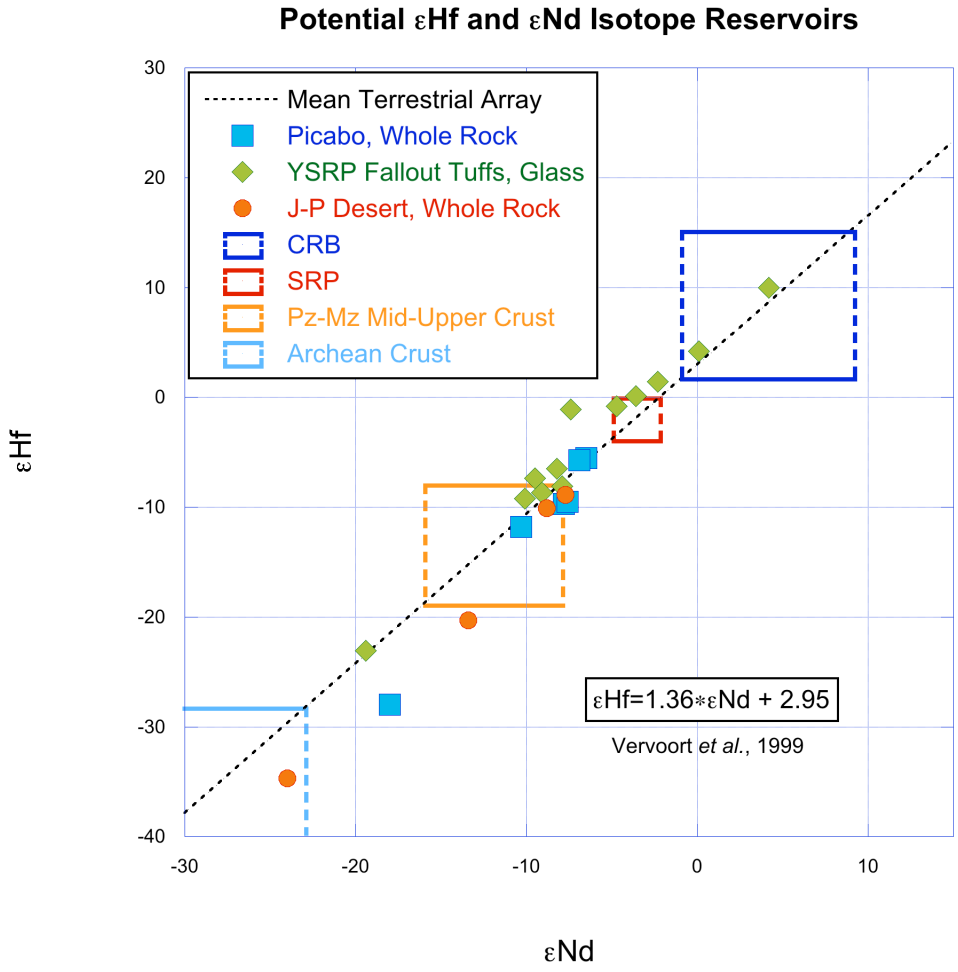

Figure 13. Potential sources of εHf signatures in Bruneau-Jarbidge (BJ) volcanics plotted versus εNd. Where both εHf and εNd are available, data are plotted as solid, colored symbols. Where only εNd data is available, the εHf is estimated using the mean terrestrial array of Vervoort *et al.* (1999) and plotted as a box representing the potential range of both εHf and εNd. Whole rock values of rhyolites from the Picabo caldera from Drew *et al.* (2013), glasses from fallout tuffs of the Yellowstone Snake River Plain (YSRP) from Nash *et al.* (2006), whole rock values from rhyolites of the J-P Desert from Colón *et al.* (2015), Columbia River Basalts (CRB) from Hanan *et al.* (2008), Snake River Plain Basalts (SRP) from Leeman *et al.* (1992), and Proterozoic to Mesozoic (Pz-Mz) mid-upper crust and Mesozoic (Mz) granitoids from DePaolo and Farmer (1984) and Fleck *et al.* (1990). The Archean crust from Leeman has a range of -23 to -52 εNd units (1985), but is only partially shown here.

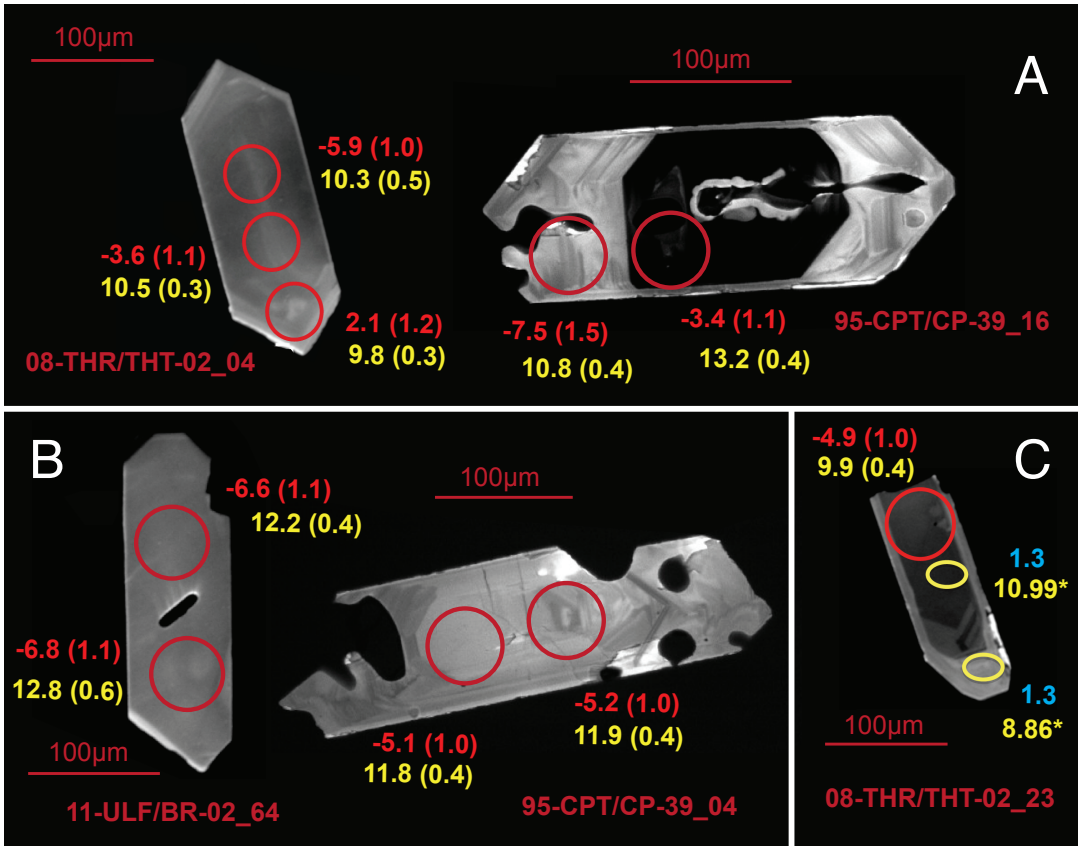

Figure 14. Bruneau-Jarbidge (BJ) zircons from tuffs and lavas showing A) heterogeneity in εHf and U-Pb ages B) homogenous εHf and U-Pb ages and C) agreement between U-Pb ages in this study and those of Seligman (2012). Red numbers are εHf values with 2 s.e. in parenthesis. Yellow numbers are U-Pb ages from this study with 2 s.e. in parenthesis. Yellow numbers with asterisks and blue numbers are U-Pb ages and $\delta^{18}O$ weight values, respectively, from Seligman (2012).

MUNZirc 1, 3, and 4 (Fisher *et al.*, 2011) were analyzed at the beginning, middle, and end of each analysis run to monitor corrections for a range of Yb concentrations. Both Lu-Hf and U-Pb data were reduced using Iolite (version 2.4). See Chapter I for a detailed description of the instrumentation, method, and data reduction protocols. Additionally, U-Pb data indicates ternary mixing between multiple radiogenic Pb populations and an initial Pb that was incorporated either during growth or with common Pb during ablation. The composition of the initial or common Pb was determined by linear fit of the most collinear array of data and was compared to Stacey-Kramer common-Pb composition for the sample age (Ludwig, 1998). The uncertainty in the initial or common-Pb composition is propogated into the error reported on each ^{207}Pb-corrected single-spot date. Zircon samples showed partial-Pb isochrons, so single-spot ages were determined following the method found in Stearns *et al.* (2015).

Results

Range of εHf and Age

Results of Lu-Hf and U-Pb analyses of zircons for one tuff and four lavas are provided in tables in Appendix A and on CL images in Appendix B. Average εHf is -6.2 units for all analyzed zircons of the BJ. Zircons show a range of -15.1 to -1.5 εHf units (Figure 15) with one value of -31.9. Nine ablation sites with εHf values >0 were excluded due to high uncertainties of the ^{176}Yb/^{177}Hf correction.

The average ^{206}Pb/^{238}U age is 11.8 Ma for all tuffs and lavas. Ages range from 8.7 Ma at the youngest to 15.3 Ma for the oldest. For consistency, values excluded from Lu-Hf calculations were also excluded from U-Pb. Of the eight analyses taken in

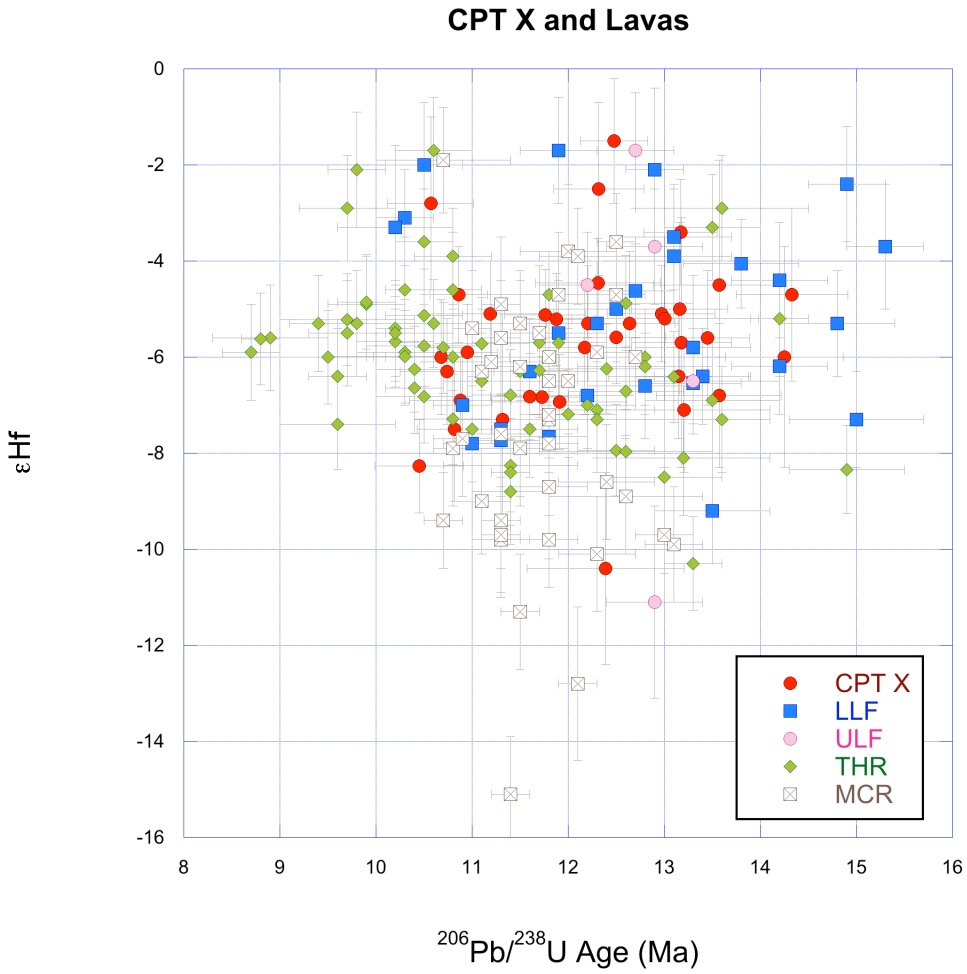

Figure 15. Ages and εHf of tuffs and rhyolites of the Bruneau-Jarbidge volcanic center. Errors bars are given as 2 s.e.

proximity to SHRIMP sites on the same zircon, four $^{206}Pb/^{238}U$ ages are within error of those of Seligman (2012), 2 are nearly within error, and 2 represent nominally different ages (Figure 16).

Zircons of the Cougar Point Tuff Unit X (CPT X) average -6.1 εHf units and range -12.7 to -1.5 εHf units. The average $^{206}Pb/^{238}U$ age for CPT X zircons is 12.2 Ma. Ages range from 10.4 ± 0.5 Ma to 14.3 ± 0.6 Ma. The youngest age is in good agreement with the most recently published eruption age of 10.9 ± 0.27 Ma for CPT X (Cathey, 2011).

Lower Lava flow (LLF) zircons average -5.3 εHf units and range from -9.2 to -1.7 εHf units. The average $^{206}Pb/^{238}U$ age for LLF zircons is 12.7 Ma. Ages range from 10.2 ± 0.6 Ma to 15.6 ± 0.4 Ma. The youngest age is 6% lower than the most recent published eruption age of 10.93 ± 0.23 Ma for LLF (Seligman, 2012). However, the zircons with the youngest three ages have high εHf values compared to other LLF zircons of similar ages. This discrepancy may indicate ablation sites that sampled multiple zones of zircon growth. If these three are excluded, the youngest age is 10.9 ± 0.3 Ma, which is in excellent agreement with the published eruption age.

Upper Lava flow (ULF) zircons average -5.5 εHf units and range from -11.1 to -1.7 εHf units. The average $^{206}Pb/^{238}U$ age for ULF zircons is 13.1 Ma. Ages range from 12.2 ± 0.5 Ma to 14.8 ± 0.7 Ma. The youngest age is 12% higher than the published eruption of 10.89 ± 0.25 Ma for ULF (Seligman, 2012). As only 5 grains of ULF were analyzed in this study, these grains are likely to be antecrysts and therefore provide poor estimates of eruption age.

Zircons of the Triguero Homestead rhyolite (THR) average -6.0 εHf units and

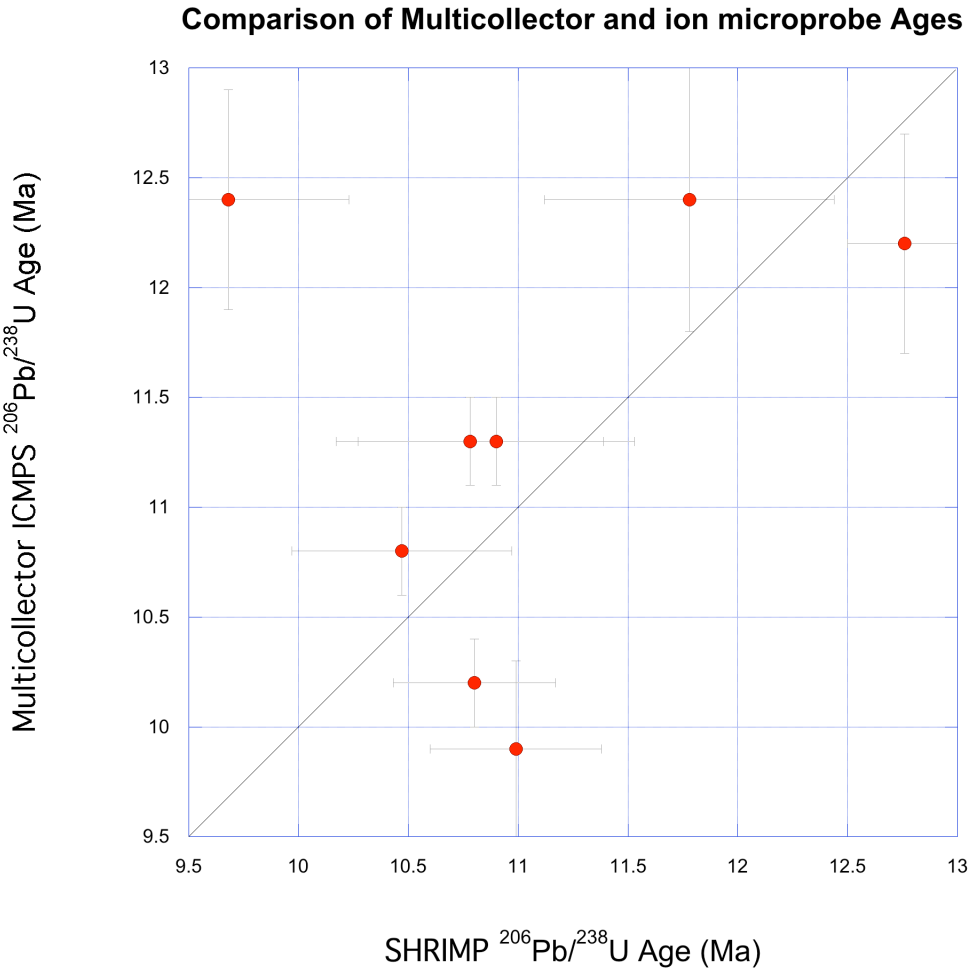

Figure 16. Comparison of $^{206}Pb/^{238}U$ ages in this study to SHRIMP $^{206}Pb/^{238}U$ ages of Seligman (2012) from adjacent spots on single zircon grains.

range from -10.3 to -1.7 εHf units. The average $^{206}Pb/^{238}U$ age for THR zircons is 11.2 Ma. Ages range from 8.7 ± 0.3 Ma to 14.9 ± 0.6 Ma. The youngest age is 17% lower than the most recently published eruption age of 10.51 ± 0.13 Ma for THR (Seligman, 2012).

Marys Creek rhyolite (MCR) zircons average -7.4 εHf units and range from -15.1 to -1.9 εHf units. A single zircon site measures -39.1 εHf units. The average $^{206}Pb/^{238}U$ age for MCR zircons is 11.9 Ma. Ages range from 10.7 ± 0.4 Ma to 13.1 ± 0.3 Ma. The youngest age is in good agreement to the most recently published eruption age of 10.29 ± 0.20 Ma for MCR (Seligman, 2012).

Zoning

Small grain sizes (<100 μm) limited multiple analyses on single zircon grains to five grains of CPT X, three grains of LLF, fifteen grains of THR, and fourteen grains of MCR (Figures 17 and 18). ULF zircons are too small to separately measure cores, rims, or mantles, so no determination of zoning can be made. Two grains of CTP X, one grain of LLF, six grains of THR, and five grains of MCR are homogeneous in εHf (within error) between cores and rims or cores and mantles.

Zircons of CPT X exhibit negative zoning in one grain between core and rim and two grains between core and mantle. Two LLF zircons are zoned between core and mantle. One grain exhibits negative zoning (higher εHf values in older growth zones) and one grain exhibits positive zoning (higher εHf values in younger growth zones). THR zircons exhibit negative zoning in three grains between core and rim, negative zoning in two grains between core and mantle, positive zoning in one grain between core and rim,

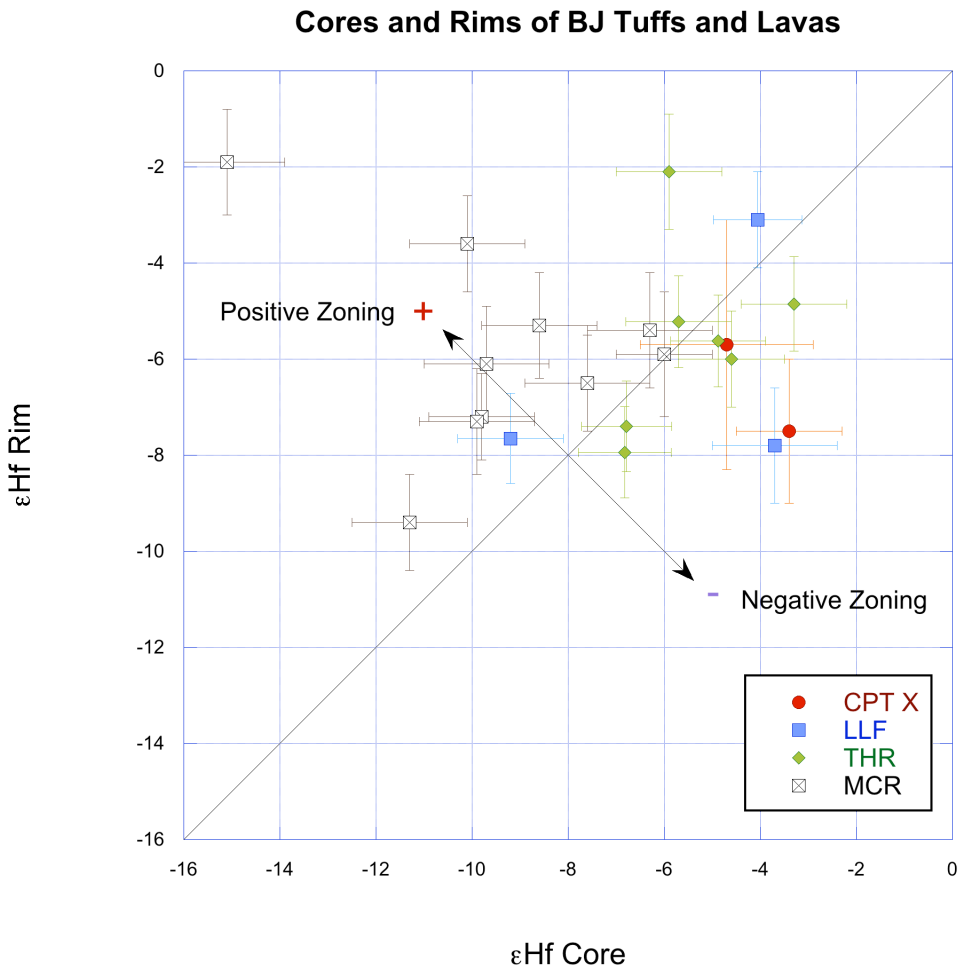

Figure 17. Comparison of cores and rims on singles grains of Cougar Point Tuff Unit X (CPT X), Lower lava flow (LLF), Triguero Homestead rhyolite (THR), and Marys Creek rhyolite (MCR). Error bars are given as 2 s.e.

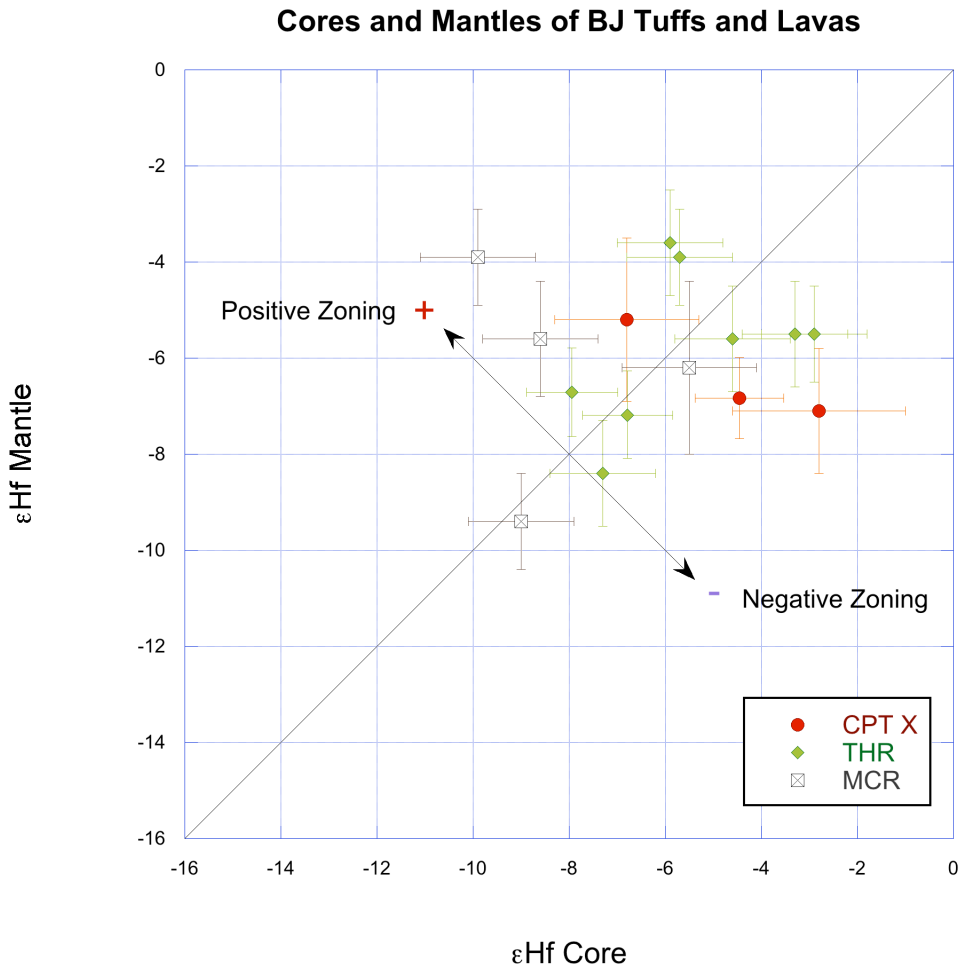

Figure 18. Comparison of cores and mantles on singles grains of Cougar Point Tuff Unit X (CPT X), Triguero Homestead rhyolite (THR), and Marys Creek rhyolite (MCR). Error bars are given as 2 s.e.

and positive zoning in three grains between core and mantle. All heterogeneous MCR zircons exhibit positive zoning. Seven grains are positively zoned between core and rim and two grains between core and mantle.

Cores and Rims

Individual grains show both heterogeneity and homogeneity in Pb and Hf isotopic ratios (Figure 14), but there is no distinctive trend between cores and rims shared by tuffs and lavas. In zircons of CPT X, the overall trend is toward higher εHf in cores versus rims (Figure 19). On average, εHf in LLF and ULF zircons does not differ between cores and rims or cores and mantles, although rims of LLF zircons are younger than the majority of cores (Figure 20 and 21). The εHf values of THR zircons generally increase with decreasing age (Figure 22), although there is no systematic difference in eHf between cores and rims. MCR zircons show lower εHf units in the core versus rims (Figure 23).

Discussion

Hafnium Isotopes and the Yellowstone Hotspot

Hafnium isotope ratios in volcanic rocks erupted from the YHS span the entire terrestrial array and reflect the relative roles of the mantle and crust in the formation of these silicic magmas (Figure 24). Magmatism began at 16.7 Ma with production of Columbia River Basalts west of the 0.706 Sr isopleth (Figure 11). A single whole rock value of +3 εHf units is known for the CRB (Prytulak *et al.*, 2006). We believe this represents a lower εHf value for the CRB as εNd for CRB basalts ranges from -1 to 9

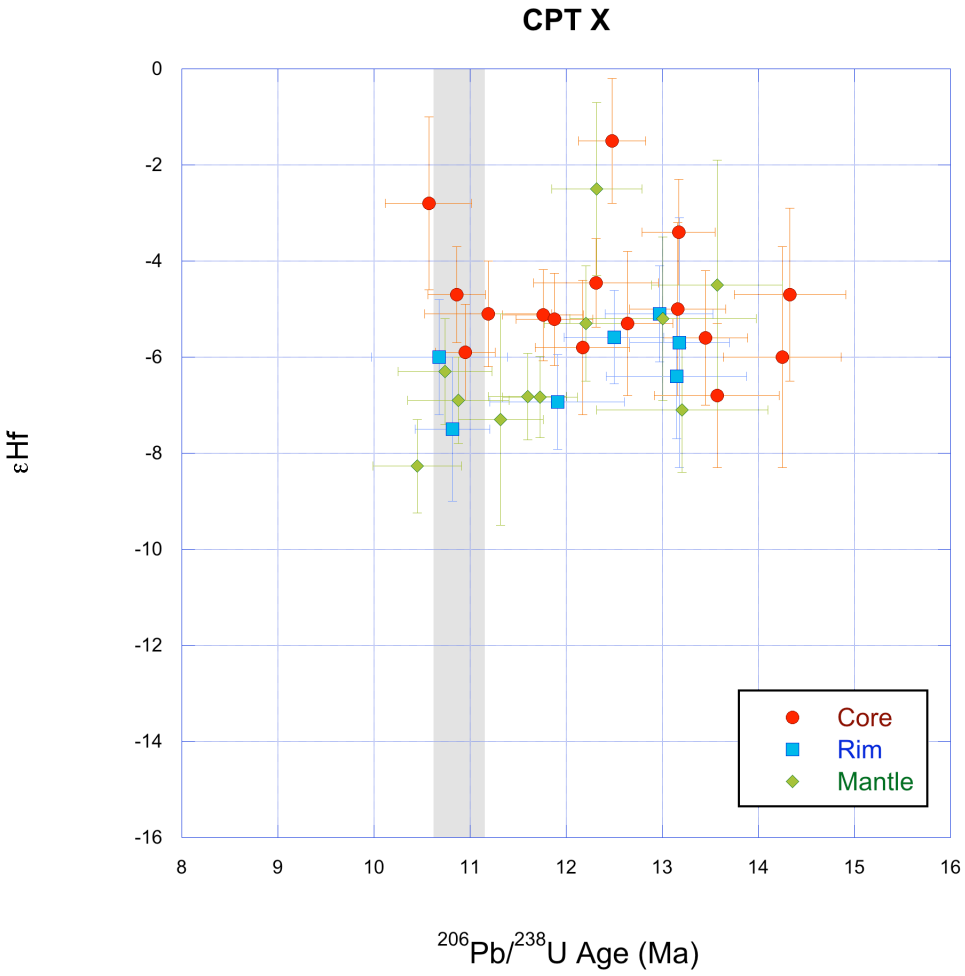

Figure 19. Plot of $^{206}Pb/^{238}U$ ages and εHf values for core, rim, and mantle on zircons of the Cougar Point Tuff Unit X (CPT X). Error bars for both ages and εHf are given as 2 s.e. The grey bar shows the most recently published eruption age of 10.9 ± 0.27 Ma (Cathey, 2011).

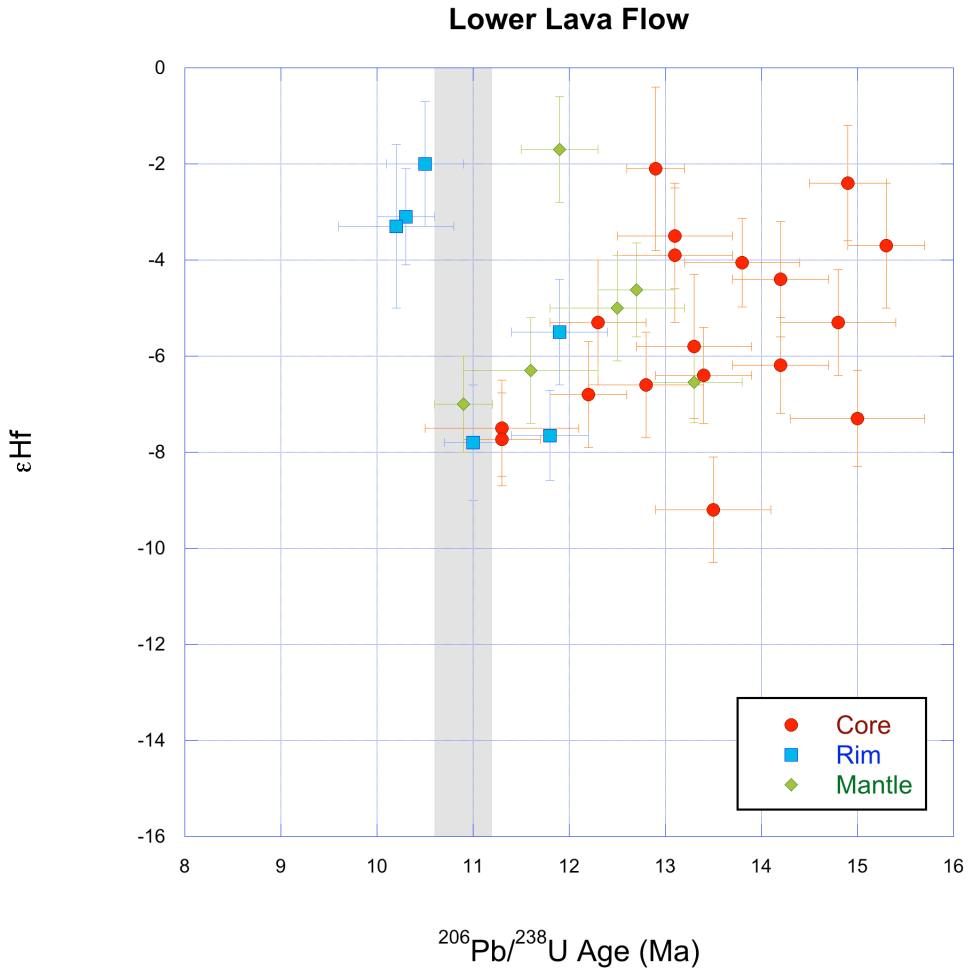

Figure 20. Plot of $^{206}Pb/^{238}U$ ages and εHf values for core, rim, and mantle on zircons of the Lower lava flow (LLF). Error bars for both ages and εHf are given as 2 s.e. The grey bar shows the most recently published eruption age of 10.9 ± 0.3 Ma (Seligman, 2012).

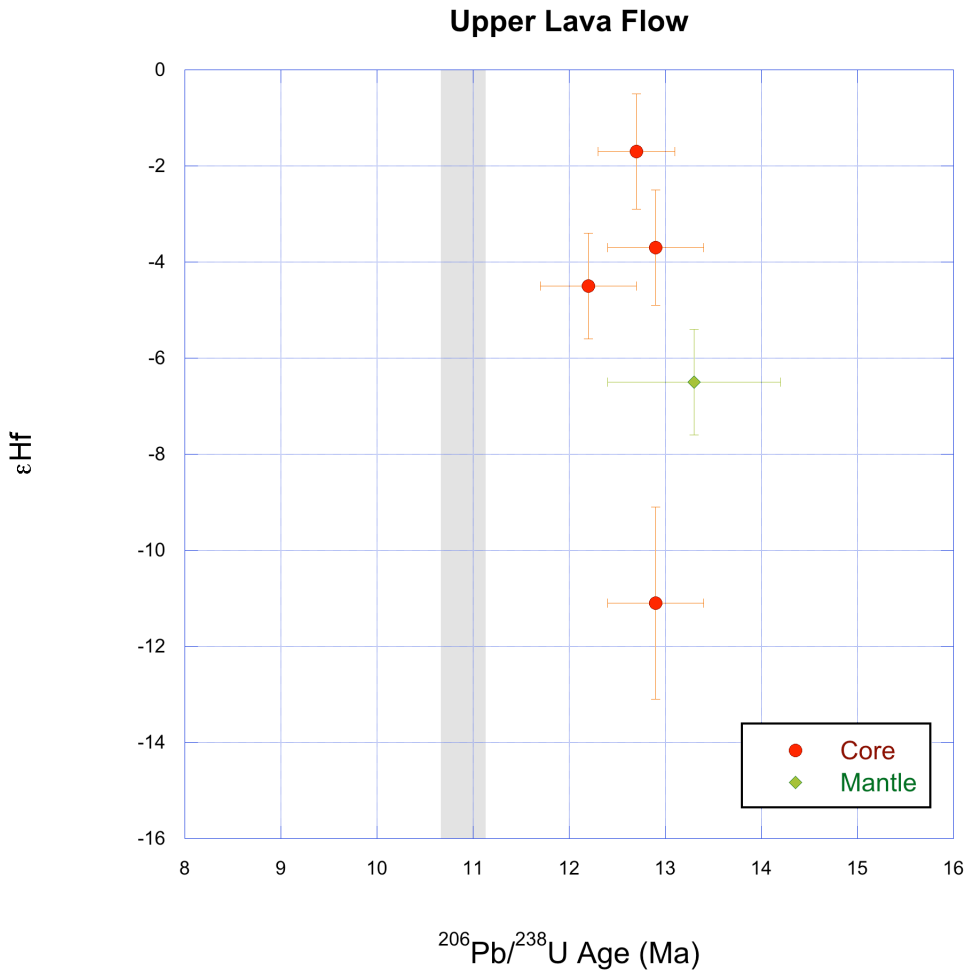

Figure 21. Plot of $^{206}Pb/^{238}U$ ages and εHf values for core, rim, and mantle on zircons of the Upper lava flow (ULF). Error bars for both ages and εHf are given as 2 s.e. The grey bar shows the most recently published eruption age of 10.89 ± 0.25 Ma (Seligman, 2012).

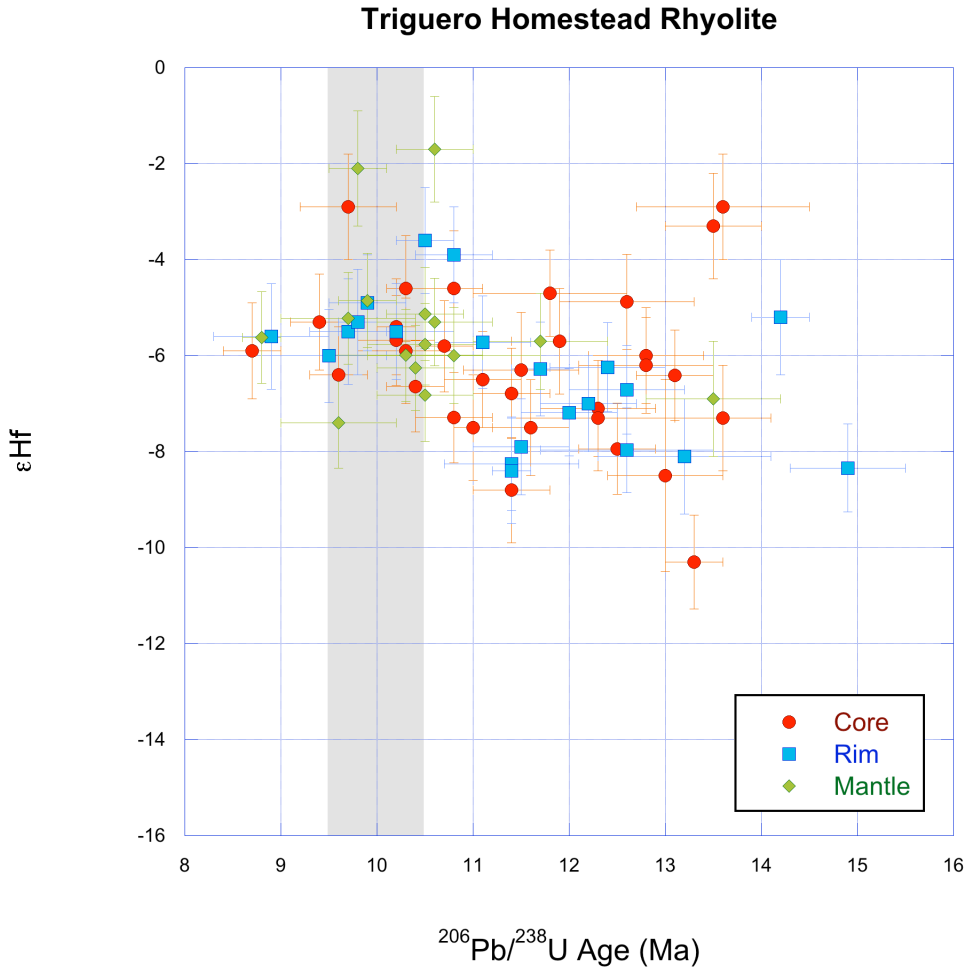

Figure 22. Plot of $^{206}Pb/^{238}U$ ages and εHf values for core, rim, and mantle on zircons of the Triguero Homestead rhyolite (THR). Error bars for both ages and εHf are given as 2 s.e. The grey bar shows the range of reported eruption ages from 9.5-10 Ma (Bonnichsen *et al.*, 2008; Seligman, 2012).

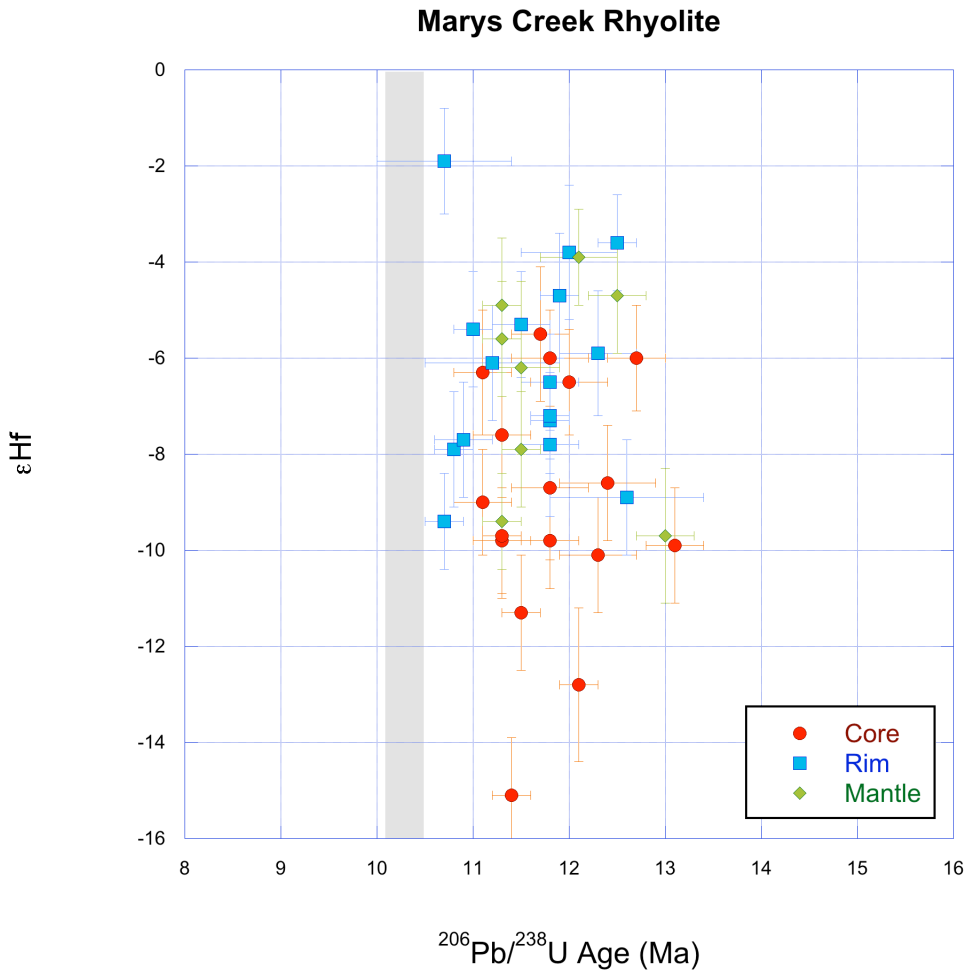

Figure 23. Plot of $^{206}Pb/^{238}U$ ages and εHf values for core, rim, and mantle on zircons of the Marys Creek rhyolite (MCR). Error bars for both ages and εHf are given as 2 s.e. The grey bar shows the most recently published eruption age of 10.29 ± 0.20 Ma (Seligman, 2012).

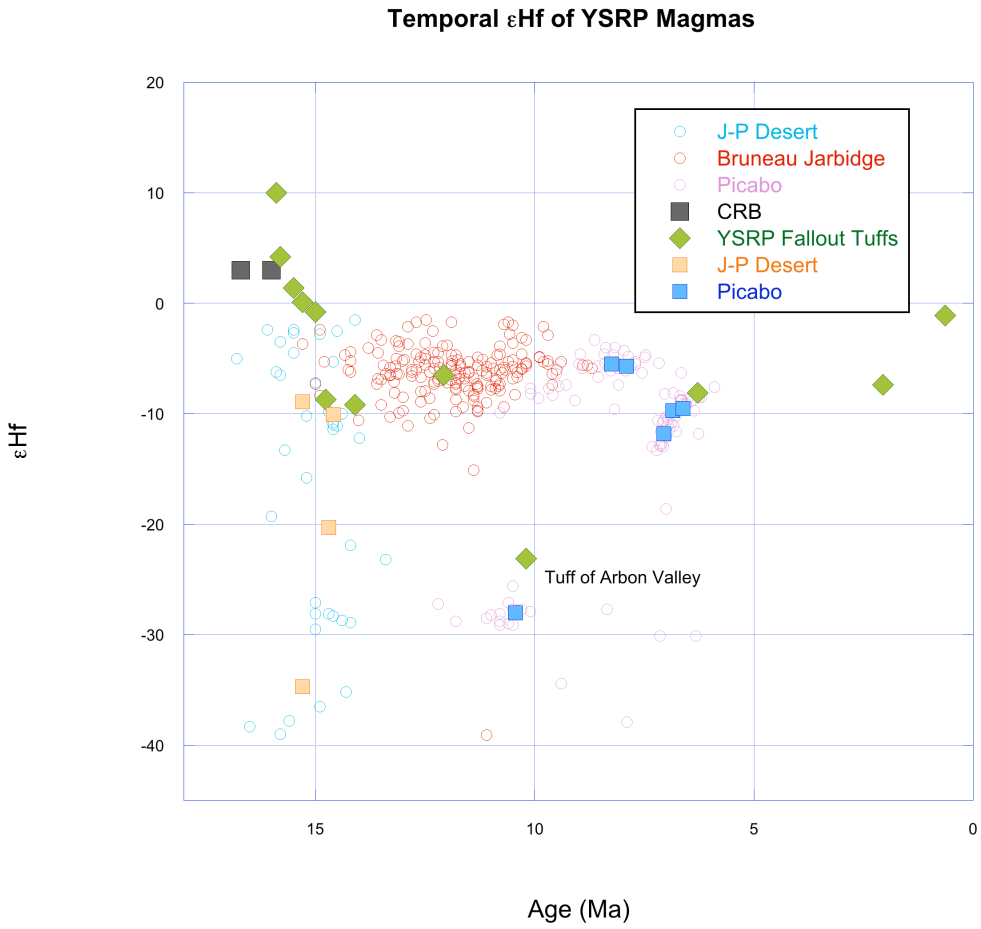

Figure 24. Ages and εHf for rhyolites of the Snake River Plain and associated Columbia River basalts. We excluded 2 xenocrysts with age values >16Ma. Open circles denote zircon values, squares denote whole rock values, and diamonds denote glass values. A single value of +3 εHf for the CRB from Prytulak *et al.* is shown spanning CRB activity from 16.7 to 16 Ma (2006). Values for J-P Desert are from Colón *et al.* (2015), Bruneau-Jarbidge from this study, Picabo from Drew *et al.* (2013), and YSRP fallout tuffs from Nash *et al.* (2006).

(Hanan *et al.*, 2008) and εHf is ~1.36 times greater than εNd along the terrestrial array (Vervoort *et al.*, 1999). That +3 εHf represents an underestimate of εHf for the CRB is supported by the +10 εHf value at 15.9 Ma for glass from YSRP fallout tuffs (Nash *et al.*, 2006). Positive εHf values imply basaltic input dominates in production of early-stage YSRP rhyolites.

Beginning at ~15 Ma, rapidly decreasing εHf values (from -0.8 to -8.7 εHf between 15.0 and 14.77 Ma) reflect increased fraction of continental crustal input as mantle-derived basalts began interacting with crust east of the transitional lithosphere. Strong crustal signatures are present at the same age for both whole rock and zircon data for the J-P desert volcanic center (Colón *et al.*, 2015), supporting crustal input from a highly negative εHf Archean basement (Figure 13).

From ~ 14 to 8 Ma, average εHf values of YSRP rhyolites show a slight increase to -6.5 for silicic glass at the Bruneau-Jarbidge volcanic center (Nash *et al.*, 2006) and rhyolite at the Picabo volcanic center (Drew *et al.*, 2013), indicating either a greater contribution of mantle-derived basalt or melting of a younger crustal protolith. This is contemporaneous with the increased volumetric rate of volcanism in the YSRP from 13.0 to 8.0 Ma (Perkins & Nash, 2002). Another stage of increased crustal input occurs from ~ 8.0 to 6.0 Ma when average εHf values fall to about -10. Only two data points lie between 6 Ma and the present day, so additional information is needed before any conclusions can be made concerning source inputs for the more recent time interval.

DM-LASS-ICPMS versus SHRIMP $^{206}Pb/^{238}U$ ages

Caution should be taken when comparing DM-LASS-ICPMS and SHRIMP $^{206}Pb/^{238}U$ ages as they consume different sample volumes. Laser-ablation spots are 53 μm in diameter and ~24 μm deep, while ion-microprobe sites are shallower and only 25 μm diameter (Seligman 2012). Thus, the analyte from DM-LASS-ICPMS is more likely to represent an average of different growth ages compared to the ion-microprobe. In addition, samples were repolished between ion-microprobe and laser ablation analysis, possibly exposing new zones within the zircons. Even so, 6 of the 8 laser ablation sites in close proximity to ion-microprobe pits show ages either within or very close to within analytical error of one another (Figure 16). Of these, the rim age determined by ion microprobe for 1 grain (01-MCR-02_87, Appendix B) is older than ion-microprobe sites located in the interior. The DM-LASS-ICPMS analysis of the other grain (08-THR/THT-02_23, Figure 14C) crosses multiple zones in the CL image and its age likely represents an average of the two zones dated by ion-microprobe. Therefore, 7 out of 8 laser ablation ages are in good agreement with those of ion-microprobe and give credence to the accuracy of ages obtained with DM-LASS-ICPMS method.

Eruption Age of the Triguero Homestead Rhyolite

The eruption age of the Triguero Homestead rhyolite was estimated to be 9.5-10 Ma based on its stratigraphic position (Bonnichsen *et al.*, 2008). Seligman (2012) reported an older $^{206}Pb/^{238}U$ age of 10.52 ± 0.13 Ma based on the weighted mean of 12 ages. However, three of the ages are <10 Ma. While most of the zircons analyzed in this study had ages ≥10.5 Ma, we observe another cluster in the range ~8.5 - 10 Ma (Figure

22). The weighted mean of this cluster is 9.48 ± 0.25 Ma (n = 14, MSWD = 6.7). If the three lowest ages (0.5 Ma younger than all others) are discarded on assumption of analytical error, the weighted mean becomes 9.71 ± 0.10 Ma (n = 11, MSWD = 0.83). These ages are within error of one another and consistent with the stratigraphic position of the Triguero Homestead rhyolite. Therefore, we believe the previously reported U-Pb age from Seligman (2012) is an artifact of a small sample population and recommend 9.71 ± 0.10 Ma as the new eruption age of the Triguero Homestead rhyolite.

Antecrysts

Out of the 190 sites on zircon that yielded data for both Lu-Hf and U-Pb isotopes, 148 (78%) are antecrysts (Figure 25). We define an antecryst age as > 4% of a unit's reported eruption age. This range is chosen based on the average error of age analyses in this study (~ 0.5 my). In addition, there are 25 antecrysts (13% of all zircons) with ages exceeding the first eruption at the Bruneau-Jarbidge volcanic center (Cougar Point Tuff III at 12.7 Ma). They range between -10.6 and -2.4 εHf units and average -6 εHf units. These earlier antecrysts (>13.2 Ma) are present in every unit with the exception of the youngest, MCR, and record the initiation of zircon crystallization at Bruneau-Jarbidge. However, the absence of antecryst-age tuffs and lavas indicates the first partial melts were of low volume and therefore failed to erupt.

In later-forming antecrysts (<13.2 Ma), the average for all antecrysts has a slightly higher crustal signature at -6.4 εHf units. However, the range spans -15.1 to -1.5 εHf units, which is near the upper and lower limits of the inferred εHf values of Pz-Mz crustal rocks and SRP basalts, respectively.

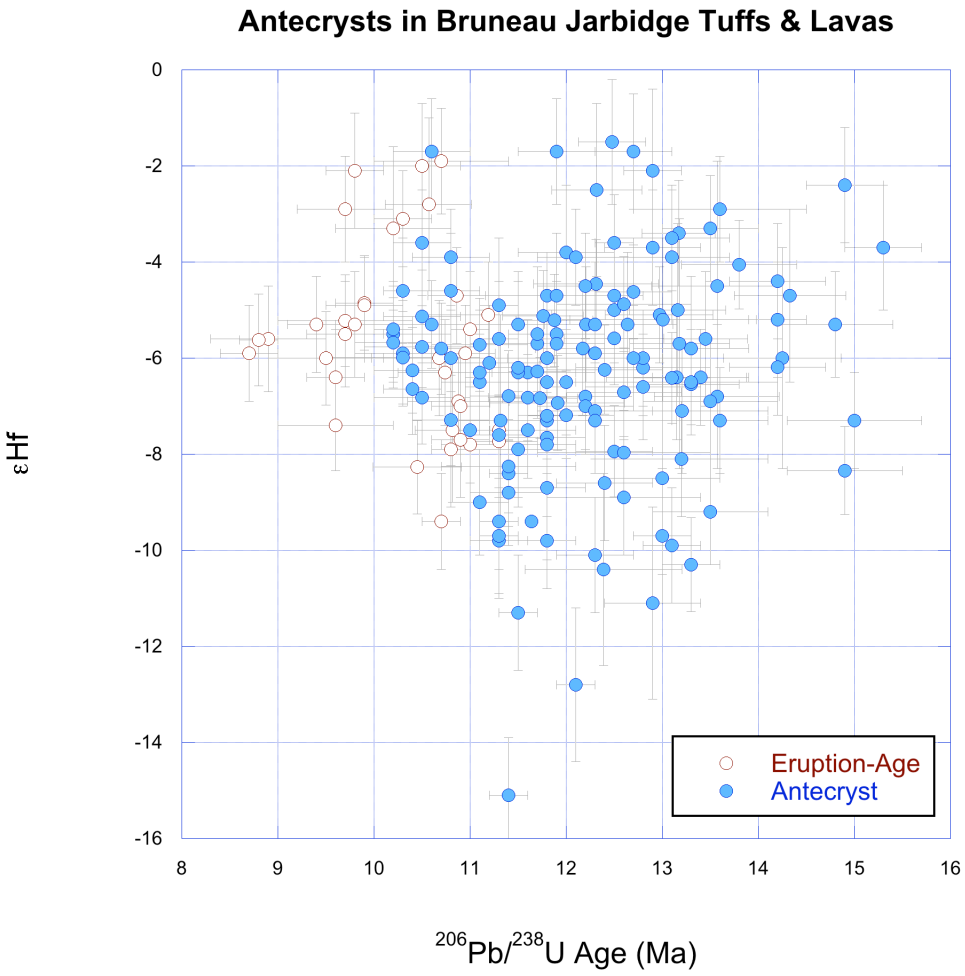

Figure 25. Ages and εHf of zircons of tuffs and lavas of the Bruneau Jarbige volcanic center, separated by eruption age zircons and antecrysts. See text for more details.

Crustal and Mantle Assimilation

Tuffs and rhyolites of the Central Snake River Plain appear to follow three main stages (Figure 26):

1) At the J-P volcanic center from 16.5 to 15 Ma, there are both hybrid and dominantly crustal melts. Hafnium isotopes document a bimodal melt source with little apparent mixing (5 grains) between the two. The population dominated by basaltic input ranges from ~ -2 to -12 εHf units and the population dominated by crustal input ranges from ~ -27 to -40 εHf units (Colón *et al.*, 2015).

2) At the Bruneau-Jarbidge volcanic between 14 and 8 Ma, magmas have a significant basaltic input. With the exception of a single value of -31.9 εHf units, the Archaen crustal signature present in the J-P volcanic center is overwhelmed by the strong mantle contribution in BJ rhyolites. The peak basaltic input occurs at the end of explosive volcanism at ~ 10.5 Ma, where εHf values are the highest (~ -2) and the range of εHf is the most narrow of all the CRP volcanics.

3) At the Picabo volcanic center between 10.4 and 8 Ma, the Archean crustal signature reappears with the eruption of the Tuff of Arbon Valley. However, like the BJ volcanics, the majority of Picabo magmas continue to show a significant basaltic input.

The average of εHf value of Picabo rhyolites excluding AV is -6.4 compared to -4.7 for BJ during approximately the same period. After 8 Ma, εHf values decline, indicating a smaller basaltic component in magmas. Declining basaltic input may be responsible for the lower temperatures and more highly evolved nature of the magmas in the eastern Snake River Plain (ESRP) and the Yellowstone Plateau (YP).

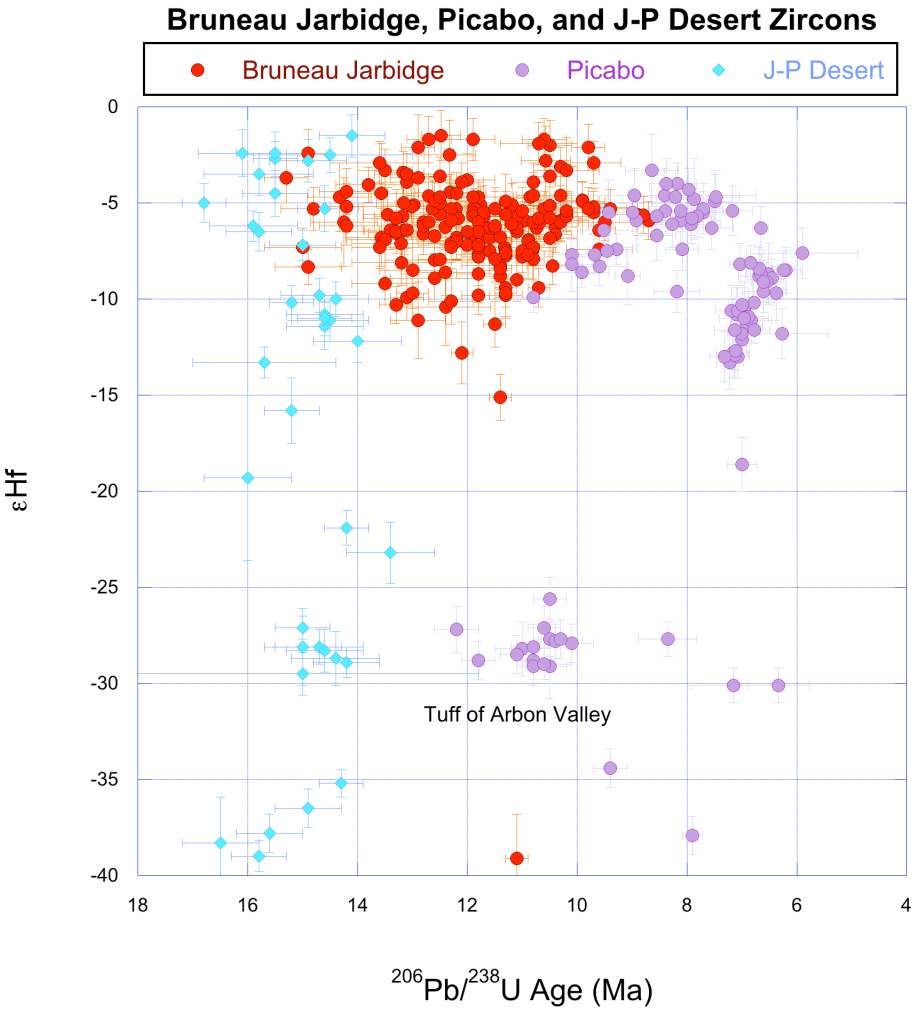

Figure 26. Ages and εHf of tuffs and rhyolites of the Bruneau-Jarbidge volcanic center from this study, Picabo caldera from Drew *et al.* (2013), and J-P Desert from Colón *et al.* (2015). We excluded 2 xenocrysts with age values >16Ma. Errors bars are given as 2 s.e.

References

Almeev, R. R., Bolte, T., Nash, B. P., Holtz, F., Erdmann, M., Cathey, H. (2012). High-temperature, low-H2O silicic magmas of the Yellowstone hotspot: an experimental study of rhyolite from the Bruneau-Jarbidge Eruptive Center, Central Snake River Plain, USA. *Journal of Petrology* **53**, 1837-1866.

Bonnichsen, B. and Citron, G. P. (1982). The Cougar Point Tuff, southwestern Idaho and vicinity. In: Bonnichsen, B. & Breckenridge, R. M. (eds) *Cenozoic Geology of Idaho, Idaho Bureau of Mines and Geology Bulletin* **26**, 255-281.

Bonnichsen, B., Leeman, W. P., Honjo, N., McIntosh, W. C., Godchaux, M. M. (2008). Miocene silicic volcanism in southwestern Idaho: geochronology, geochemistry, and evolution of the central Snake River Plain. *Bulletin of Volcanology* **70**, 315-342.

Boroughs, S., Wolff, J., Bonnichsen, B., Godchaux, M., Larson, P. (2005). Large-volume, low-δ18O rhyolites of the central Snake River Plain, Idaho, USA. *Geological Society of America* **33**, 821-824.

Branney, M. J., Bonnichsen, B., Andrews, G. D. M., Ellis, B., Barry, T. L., McCurry, M. (2008). 'Snake River (SR)-type' volcanism at the Yellowstone hotspot track: distinctive products from unusual, high-temperature silicic super-eruptions. *Bulletin of Volcanology* **70**, 293-314.

Camp, V. E. and Ross, M. E. (2004). Mantle dynamics and genesis of mafic magmatism in the intermontane Pacific Northwest. *Journal of Geophysical Research* **109**, 1-14.

Cathey, H. E., Nash, B. P. (2004). The Cougar Point Tuff: Implications for thermochemical zonation and longevity of high-temperature, large-volume silicic magmas of the Miocene Yellowstone hotspot. *Journal of Petrology* **45**, 27-58.

Cathey, H., Nash, B., Valley, J., Kita, N., Ushikubo, T., Spicuzza, M. (2007). Pervasive and persistent large-volume, low $\delta^{18}O$ silicic magma generation at the Yellowstone hotspot, 12.7-10.5 Ma: ion microprobe analyses of zircon in the Cougar Point Tuff. *AGU Fall Meeting Abstracts* **88**, 52. Abstract V51C-0708C.

Cathey, H. E., Nash, B. P. (2009). Pyroxene thermometry of rhyolite lavas of the Bruneau–Jarbidge eruptive center, Central Snake River Plain. *Journal of Volcanoogy and Geothermal Research* **188**, 173-185.

Cathey, H. E., Nash, B. P., Seligman, A. N., Valley, J. W., Kita, N., Allen, C. M., Campbell, I. H., Vazquez, J. A., Wooden, J. L. (2011). Low $\delta^{18}O$ zircons from the Bruneau-Jarbidge eruptive center: a key to crustal anatexis along the track of the Yellowstone hotspot. *AGU Fall Meeting Abstracts*. Abstract V11A-2510C.

Citron, G. P. (1976). Idavada ash-flows in the Three Creek area, southwestern Idaho, and their regional significance. Masters thesis, Cornell University, Ithaca, NY.

DePaolo, D. J. & Farmer, G. L. (1984). Isotopic data bearing on the origin of Mesozoic and Tertiary granitic rocks in the western United States. *Philosophical Transactions of the Royal Society of London. Series A, Mathematical and Physical Sciences* **310**, 743-753.

Drew, D. L., Bindeman, I. N., Watts, K. E., Schmitt, A. K., Fu, B., McCurry, M. (2013). Crustal-scale recycling in caldera complexes and rift zones along the Yellowstone hotspot track: O and Hf isotopic evidence in diverse zircons from voluminous rhyolites of the Picabo volcanic field, Idaho. *Earth and Planetary Science Letters* **381**, 63-77.

Ellis, B. S., Wolff, J.A., Boroughs, S., Mark, D. F., Starkel, W. A., Bonnichsen, B. (2013) Rhyolitic volcanism of the central Snake River Plain: a review. *Bulletin of Volcanology* **75**, 1-19.

Fisher, C. M., Hanchar, J. M., Samson, S. D., Dhuime, B., Blichert-Toft, J., Vervoort, J. D., Lam, R. (2011). Synthetic zircon doped with hafnium and rare earth elements: A reference material for in situ hafnium isotope analysis. *Chemical Geology* **286**, 32-47.

Fleck, R. J. (1990). Nd, Sr, and trace element evidence of large-scale crustal contamination of magmas of the Idaho batholith. In: Anderson, J. L. (eds) *The nature and origin of Cordilleran magmatism: Geological Society of America Memoir* **174**, 359-373.

Hanan, B. B., Shervais, J. W., Vetter, S. K (2008). Yellowstone plume–continental lithosphere interaction beneath the Snake River Plain. *Geology* **36**, 51-54.

Hooper, P. R. & Hawkesworth, C. J. (1993). Isotopic and geochemical constraints on the origin and evolution of the Columbia River Basalt. *Journal of Petrology* **34**, 1203-1246.

Hoskin, P. W. O, Schaltegger, U. (2003). The composition of zircon in igneous and metamorphic petrogenesis. In: Hanchar, J. M., Hoskins, P. W. O (Eds). *Zircon: Reviews in Mineralogy and Geochemistry* **53**, 27-62.

Kinney, P. D. & Maas, R. (2003). Lu-Hf and Sm-Nd isotopes in zircon. *Reviews in Mineralogy and Geochemistry* **53**, 327-341.

Leeman, W. P. & Manton, W. I. (1971). Strontium isotopic composition of basaltic lavas from the Snake River Plain, Southern Idaho. *Earth and Planetary Science Letters* **11**, 420-434.

Leeman, W. P., Oldow, J. S., Hart, W. K. (1982). Lithosphere-scale thrusting in the wester U.S. Cordillera as constrained by Sr and Nd isotopic transitions in Neogene volcanic rocks. *Geology* **20**, 63-66.

Leeman, W. P., Menzies, M. A., Matty, D. J., Embree, G. F. (1985). Strontium, neodymium and lead isotopic compositions of deep crustal xenoliths from the Snake River Plain: evidence for Archaean basement. *Earth and Planetary Science Letters* **75**, 354-368.

Leeman, W. P., Oldow, J. S., Hart, W. K. (1992). Lithosphere-scale thrusting in the western U.S. Cordillera as constrained by Sr and Nd isotopic transitions in Neogene volcanic rocks. *Geology* **20**, 63-66.

Ludwig, K. R. (1998). On the treatment of concordant uranium-lead ages. *Geochimica et Cosmochimica Acta* **62**, 665-676.

Manduca, C. A., Silver, L.T. & Taylor, H.P. (1992). $^{87}Sr/^{86}Sr$ and $^{18}O/^{16}O$ isotopic systematics and geochemistry of granitoid plutons across a steeply-dipping boundary between contrasting lithospheric blocks in western Idaho. *Contributions to Mineralogy and Petrology* **109**, 355-372.

Nash, B. P., Perkins, M. E., Christensen, J. N., Lee, D-C., Halliday, A. N. (2006) The Yellowstone hotspot in space and time: Nd and Hf isotopes in silicic magmas. *Earth and Planetary Science Letters* **247**, 143-156.

Perkins, M. E. & Nash, B. P. (2002). Explosive silicic volcanism of the Yellowstone hotspot: The ash fall tuff record. *GSA Bulletin* **114**, 367-381.

Seligman, A. (2012). Generation of Low d18O Silicic Magmas, Bruneau-Jarbidge Volcanic Center, Yellowstone Hotspot: Evidence From Zircons, Including Oxygen Isotopes, U-Th-Pb Dating, and Melt Inclusions. Masters thesis, University of Utah, Salt Lake City, UT.

Shoemaker, K. A. & Hart, W. K. (2002). Temporal controls on basalt genesis and evolution on the Owyhee Plateau, Idaho and Oregon. In: Bonnichsen, B., White, C. M., McCurry, M. (eds) *Tectonic and Magmatic Evolution of the Snake River Plain Volcanic Province: Idaho Geological Survey Bulletin* **30**, 313-328.

Smith, R. B., Jordan, M., Steinberger, B., Puskas, C. M., Farrell, J., Waite, G. P., Husan, S., Chang, W-L., O'Connell, R. (2009). Geodynamics of the Yellowstone hotspot and mantle plume: Seismic and GPS imaging, kinematics, and mantle flow. *Journal of Volcanology and Geothermal Research* **188**, 26-56.

Stearns, M.A., Hacker, B.R. Ratschbacher, L., Rutte, D., Kylander-Clark, A.R.C. (2015). Titanite petrocrhonology of the Pamir gneiss domes: Implications for middle to deep crust exhumation and titanite closure to Pb and Zr diffusion. *American Geophysical Union* **34**, 784-802.

Vervoort, J. D., Patchett, P. J., Blichert-Toft, J., Albarède, F. (1999). Relationships between Lu-Hf and Sm-Nd isotopic systems in the global sedimentary system. *Earth and Planetary Science Letters* **168**, 79-99.

APPENDIX A

Lu-Hf AND U-Pb RESULTS OF BRUNEAU-JARBIDGE ZIRCONS

The following table (Table 4) includes εHf, εHf_i, and $^{206}Pb/^{238}U$ age results from this study. The $\delta^{18}O$ ‰ for tuffs (Cathey, 2011) and lavas (Seligman, 2012) are provided where analyses between studies were taken on the same grain. Additional $^{206}Pb/^{238}U$ ages on lava grains from Seligman (2012) are also given. Initial epsilon Hf values were calculated using the CHUR values of Bouvier *et al.* (2008) and the ^{176}Lu decay constant of Söderlund *et al.* (2004).

Table 4. Results of Lu-Hf and U-Pb analysis of BJ zircons

Unit	Sample #	εHf	εHf_i	2 s.e.	$^{206}Pb/^{238}U$ Age (Ma)	2 s.e.	Location	Age[2]	$\delta^{18}O$ ‰[1,2]
Cougar Point Tuff									
Unit X	95-CPT-CP-39_02	-1.5	-1.9	1.3	12.5	0.4	core		
Unit X	95-CPT-CP-39_03b	-5.6	-6.0	1.0	12.5	0.5	rim		
Unit X	95-CPT-CP-39_04a	-5.1	-5.5	1.0	11.8	0.4	core		
Unit X	95-CPT-CP-39_04b	-5.2	-5.6	1.0	11.9	0.4	core		
Unit X	95-CPT-CP-39_07	-5.1	-5.5	1.0	13.0	0.6	rim		
Unit X	95-CPT-CP-39_10	-5.6	-6.0	1.4	13.4	0.4	core		1.31
Unit X	95-CPT-CP-39_10						rim		1.98
Unit X	95-CPT-CP-39_11a	-6.3	-6.7	1.1	10.7	0.5	mantle		
Unit X	95-CPT-CP-39_11b	-6.9	-7.3	1.0	11.9	0.7	rim		
Unit X	95-CPT-CP-39_13a	7.6	7.1	1.5	10.2	0.3	core		
Unit X	95-CPT-CP-39_13b	5.2	4.7	1.9	11.7	0.3	core		
Unit X	95-CPT-CP-39_13c	6.7	6.2	1.8	11.7	0.3	mantle		
Unit X	95-CPT-CP-39_14a	-6.9	-7.3	0.9	10.9	0.5	mantle		
Unit X	95-CPT-CP-39_14b	-8.3	-8.7	1.0	10.4	0.5	mantle		
Unit X	95-CPT-CP-39_14c	-10.6		1.3			mantle		
Unit X	95-CPT-CP-39_14d	-9.4		1.2			mantle		
Unit X	95-CPT-CP-39_16a	3.1	2.7	1.5	10.6	0.2	core		
Unit X	95-CPT-CP-39_16b	-3.4	-3.8	1.1	13.2	0.4	core		
Unit X	95-CPT-CP-39_16c	-7.5	-7.9	1.5	10.8	0.4	rim		
Unit X	95-CPT-CP-39_17a				10.7	0.4	core		
Unit X	95-CPT-CP-39_17b	-2.8	-3.2	1.8	10.6	0.4	core		
Unit X	95-CPT-CP-39_17c	-7.3	-7.7	2.2	11.3	0.4	mantle		
Unit X	95-CPT-CP-39_17d	-7.1	-7.4	1.3	13.2	0.9	mantle		
Unit X	95-CPT-CP-39_19a	-5.3	-5.7	1.5	12.6	0.5	core		

Table 4 continued

Unit	Sample #	εHf	εHf_i	2 s.e.	$^{206}Pb/^{238}U$ Age (Ma)	2 s.e.	Location	Age[2]	$\delta^{18}O$ ‰[1,2]
Unit X	95-CPT-CP-39_19				12.8	0.5	core		1.55
Unit X	95-CPT-CP-39_19						rim		1.7
Unit X	95-CPT-CP-39_21	-2.5	-2.9	1.8	12.3	0.5	mantle		
Unit X	95-CPT-CP-39_25a	-6.8	-7.2	1.5	13.6	0.6	core		
Unit X	95-CPT-CP-39_25b	-5.2	-5.6	1.7	13.0	1.0	mantle		
Unit X	95-CPT-CP-39_25c	-5.7		2.1			mantle		
Unit X	95-CPT-CP-39_38a	2.6	2.3	1.8	11.9	0.4	mantle		
Unit X	95-CPT-CP-39_38b	-6.0	-6.4	1.2	10.7	0.7	rim		
Unit X	95-CPT-CP-39_47a				11.4	0.8	core		
Unit X	95-CPT-CP-39_47b	-5.3	-5.7	1.2	12.2	0.4	mantle		
Unit X	95-CPT-CP-39_47c	-10.4	-10.7	2.0	12.4	0.8	mantle		
Unit X	95-CPT-CP-39_49a	-5.7	-6.0	2.6	13.2	0.5	core		
Unit X	95-CPT-CP-39_49b				11.6	0.4	mantle		
Unit X	95-CPT-CP-39_49c	-4.7	-5.0	1.8	14.3	0.6	core		
Unit X	95-CPT-CP-39_50	-6.4	-6.7	1.3	13.2	0.7	rim		
Unit X	95-CPT-CP-39_51	-4.5	-4.8	2.6	13.6	0.6	mantle		
Unit X	95-CPT-CP-39_52	-5.0	-5.4	1.8	13.2	0.5	core		
Unit X	95-CPT-CP-39_54	-6.0	-6.3	2.3	14.2	0.6	core		
Unit X	95-CPT-CP-39_60a	-5.8	-6.2	1.4	12.2	0.5	core		
Unit X	95-CPT-CP-39_60b	-5.1	-5.4	1.1	11.2	0.7	core		
Unit X	95-CPT-CP-39_63	-5.6		1.7			mantle		
Unit X	95-CPT-CP-39_67	-12.7		2.6			rim		
Unit X	95-CPT-CP-39_70	-4.7	-5.1	1	10.9	0.3	core		
Unit X	95-CPT-CP-39_71a	-6.8	-7.2	0.8	11.7	0.4	mantle		
Unit X	95-CPT-CP-39_71b	-4.4	-4.8	0.9	12.3	0.6	core		

Table 4 continued

Unit	Sample #	εHf	εHf_i	2 s.e.	$^{206}Pb/^{238}U$ Age (Ma)	2 s.e.	Location	Age[2]	$\delta^{18}O$ ‰[1,2]
Unit X	95-CPT-CP-39_71c	-6.8	-7.2	0.9	11.6	0.4	mantle		
Unit X	95-CPT-CP-39_83a	-5.9	-6.3	1.0	11.0	0.3	core		
Unit X	95-CPT-CP-39_83b	2.4	2.0	2.5	11.1	0.3	core		
Rhyolite Lavas									
Lower lava flow	11-ULF/BR-02_02a	-4.0	-4.4	0.9	13.8	0.6	core		
Lower lava flow	11-ULF/BR-02_02b	-3.1	-3.5	1.0	10.3	0.3	rim		
Lower lava flow	11-ULF/BR-02_03	-7.5	-7.9	1.0	11.3	0.8	core		
Lower lava flow	11-ULF/BR-02_05	-6.2	-6.5	1.0	14.2	0.5	core		
Lower lava flow	11-ULF/BR-02_06	-4.4	-4.7	1.2	14.2	0.5	core		
Lower lava flow	11-ULF/BR-02_20	-7.7	-8.1	1.0	11.3	0.4	core		
Lower lava flow	11-ULF/BR-02_09	-6.5	-6.9	0.8	13.3	0.5	mantle		
Lower lava flow	11-ULF/BR-02_10	-2.1	-2.4	1.7	12.9	0.3	core		
Lower lava flow	11-ULF/BR-02_12	-3.9	-4.3	1.4	13.1	0.6	core		
Lower lava flow	11-ULF/BR-02_33a	-9.2	-9.5	1.1	13.5	0.6	core		
Lower lava flow	11-ULF/BR-02_33b	-7.6	-8.0	0.9	11.8	0.4	rim		
Lower lava flow	11-ULF/BR-02_35	-7.3	-7.6	1.0	15.0	0.7	core		1.3
Lower lava flow	11-ULF/BR-02_35						rim		1.3
Lower lava flow	11-ULF/BR-02_36	-6.3	-6.6	1.1	11.6	0.7	mantle		
Lower lava flow	11-ULF/BR-02_51	-5.5	-5.9	1.1	11.9	0.5	rim		
Lower lava flow	11-ULF/BR-02_52	3.1	2.7	1.8	12.8	0.9	core		
Lower lava flow	11-ULF/BR-02_53	-7.0	-7.4	1.0	10.9	0.3	mantle		
Lower lava flow	11-ULF/BR-02_39a	-3.7	-4.0	1.3	15.3	0.4	core		
Lower lava flow	11-ULF/BR-02_39b	-7.8	-8.2	1.2	11.0	0.3	rim		
Lower lava flow	11-ULF/BR-02_42	-3.5	-3.9	1.1	13.1	0.6	core		

Table 4 continued

Unit	Sample #	εHf	εHf_i	2 s.e.	$^{206}Pb/^{238}U$ Age (Ma)	2 s.e.	Location	Age[2]	$\delta^{18}O$ ‰[1,2]
Lower lava flow	11-ULF/BR-02_56a	-3.3	-3.7	1.7	10.2	0.6	rim		
Lower lava flow	11-ULF/BR-02_56b	-1.7	-2.1	1.1	11.9	0.4	mantle		
Lower lava flow	11-ULF/BR-02_56c	-4.6	-5.0	1.0	12.7	0.4	mantle		
Lower lava flow	11-ULF/BR-02_58	-2.4	-2.7	1.2	14.9	0.4	core		
Lower lava flow	11-ULF/BR-02_60	-5.8	-6.1	1.5	13.3	0.6	core		
Lower lava flow	11-ULF/BR-02_61a	-5.0	-5.4	1.1	12.5	0.7	mantle		
Lower lava flow	11-ULF/BR-02_61b	-2.0	-2.5	1.3	10.5	0.4	rim		
Lower lava flow	11-ULF/BR-02_64a	-6.8	-7.2	1.1	12.2	0.4	core		
Lower lava flow	11-ULF/BR-02_64b	-6.6	-7.0	1.1	12.8	0.6	core		
Lower lava flow	11-ULF/BR-02_67	-6.4	-6.8	1.0	13.4	0.5	core		
Lower lava flow	11-ULF/BR-02_69	-5.3	-5.6	1.3	12.3	0.5	core		
Lower lava flow	11-ULF/BR-02_74	-5.3	-5.7	1.1	14.8	0.6	core		
Upper lava flow	10-ULF/BR-02_21	-11.1	-11.5	2.0	12.9	0.5	core		
Upper lava flow	10-ULF/BR-02_15				14.8	0.7	core		
Upper lava flow	10-ULF/BR-02_01	-1.7	-2.0	1.2	12.7	0.4	core		
Upper lava flow	10-ULF/BR-02_57a	-4.5	-4.8	1.1	12.2	0.5	core		
Upper lava flow	10-ULF/BR-02_57b	-3.7	-4.0	1.2	12.9	0.5	core		
Upper lava flow	10-ULF/BR-02_55	-6.5	-6.8	1.1	13.3	0.9	mantle		
Triguero Homestead	08-THR/THT-02_02a	-5.5	-5.9	1.1	9.7	0.4	mantle		
Triguero Homestead	08-THR/THT-02_02b	-4.8	-5.3	1.0	9.9	0.3	rim		
Triguero Homestead	08-THR/THT-02_02c	-3.3	-3.6	1.1	13.5	0.5	core		

Table 4 continued

Unit	Sample #	εHf	εHf_i	2 s.e.	$^{206}Pb/^{238}U$ Age (Ma)	2 s.e.	Location	Age[2]	$\delta^{18}O$ ‰[1,2]
Triguero Homestead	08-THR/THT-02_03a	-1.7	-2.1	1.1	10.6	0.4	rim		
Triguero Homestead	08-THR/THT-02_03b	-4.9	-5.3	1.1			core		
Triguero Homestead	08-THR/THT-02_04a	-2.1	-2.5	1.2	9.8	0.3	rim		
Triguero Homestead	08-THR/THT-02_04b	-3.6	-4.0	1.1	10.5	0.3	mantle		
Triguero Homestead	08-THR/THT-02_04c	-5.9	-6.2	1.1	10.3	0.5	core		
Triguero Homestead	08-THR/THT-02_05	-5.3	-5.7	1.0	9.4	0.3	core		
Triguero Homestead	08-THR/THT-02_11a	-6.4		1.4			core		
Triguero Homestead	08-THR/THT-02_11b	-7.4	-7.8	0.9	9.6	0.6	rim		
Triguero Homestead	08-THR/THT-02_11c	-6.5	-6.9	1.0	11.1	0.4	core		
Triguero Homestead	08-THR/THT-02_11d	-7.5	-7.9	1.0	11.6	0.4	core		
Triguero Homestead	08-THR/THT-02_11e	-7.2	-7.6	0.9	12.0	0.5	mantle		
Triguero Homestead	08-THR/THT-02_11f	-6.8	-7.2	0.9	11.4	0.4	core		
Triguero Homestead	08-THR/THT-02_13a	-7.9	-8.3	1.0	11.5	0.5	mantle		
Triguero Homestead	08-THR/THT-02_13b	-6.3		1.1			rim		
Triguero Homestead	08-THR/THT-02_16	-7.5	-7.9	1.1	11.0	0.2	core		
Triguero Homestead	08-THR/THT-02_20						core	11.65	-1
Triguero Homestead	08-THR/THT-02_20a	-6.2	-6.6	0.9	12.4	0.6	mantle		
Triguero Homestead	08-THR/THT-02_20b	-8.1	-8.5	1.2	13.2	0.9	mantle		
Triguero Homestead	08-THR/THT-02_20c	-8.0	-8.3	0.9	12.6	0.9	mantle		
Triguero Homestead	08-THR/THT-02_20						mantle	11.78	0.9
Triguero Homestead	08-THR/THT-02_20						rim	10.62	1
Triguero Homestead	08-THR/THT-02_22	-6.2	-6.7	0.9	10.4	0.4	rim		
Triguero Homestead	08-THR/THT-02_22						core	10.99	1.3
Triguero Homestead	08-THR/THT-02_23	-4.9	-5.4	1.0	9.9	0.4	mantle		
Triguero Homestead	08-THR/THT-02_23						rim	8.86	1.3

Table 4 continued

Unit	Sample #	εHf	εHf_i	2 s.e.	$^{206}Pb/^{238}U$ Age (Ma)	2 s.e.	Location	Age[2]	$\delta^{18}O$ ‰[1,2]
Triguero Homestead	08-THR/THT-02_24a	-2.9	-3.3	1.1	9.7	0.5	core		
Triguero Homestead	08-THR/THT-02_24b	-5.5	-5.9	1.0	10.2	0.6	mantle		
Triguero Homestead	08-THR/THT-02_26	-5.3	-5.7	0.9	10.6	0.6	rim		
Triguero Homestead	08-THR/THT-02_27	-5.8	-6.3	1.0			core		
Triguero Homestead	08-THR/THT-02_28	-7.3	-7.7	0.9	10.8	0.4	core		
Triguero Homestead	08-THR/THT-02_34	-4.7	-5.1	0.9	11.8	0.8	core		
Triguero Homestead	08-THR/THT-02_37a	-4.8	-5.2	1.1			core		
Triguero Homestead	08-THR/THT-02_37b	-5.1	-5.5	1.0	10.5	0.4	rim		
Triguero Homestead	08-THR/THT-02_38	-8.8	-9.2	1.1	11.4	0.4	core		
Triguero Homestead	08-THR/THT-02_39	-6.3	-6.7	1.0	11.7	0.3	mantle		
Triguero Homestead	08-THR/THT-02_40a	-5.7	-6.1	1.1	11.9	0.5	core		
Triguero Homestead	08-THR/THT-02_40b	-6.6	-7.0	1.1			mantle		
Triguero Homestead	08-THR/THT-02_40c	-3.9	-4.3	1.0	10.8	0.4	mantle		
Triguero Homestead	08-THR/THT-02_40d	-5.2	-5.7	1.0	9.7	0.7	rim		
Triguero Homestead	08-THR/THT-02_41a	-4.6	-5.0	1.2	10.8	0.3	core		
Triguero Homestead	08-THR/THT-02_41b	-5.6	-6.0	1.1	8.9	0.6	mantle		
Triguero Homestead	08-THR/THT-02_42	-8.2	-8.6	1.0	11.4	0.7	mantle		
Triguero Homestead	08-THR/THT-02_71	-6.3	-6.6	1.2	11.5	0.6	core		
Triguero Homestead	08-THR/THT-02_72	-2.9	-3.2	1.1	13.6	0.9	core		
Triguero Homestead	08-THR/THT-02_73	-6.0	-6.4	1.0	10.3	0.8	rim		
Triguero Homestead	08-THR/THT-02_44a	-5.2	-5.5	1.2	14.2	0.3	mantle		
Triguero Homestead	08-THR/THT-02_44b	-5.3	-5.7	1.1	9.8	0.2	mantle		
Triguero Homestead	08-THR/THT-02_46				10.0	0.5	mantle		
Triguero Homestead	08-THR/THT-02_47	-5.7	-6.1	1.0	11.7	0.7	rim		
Triguero Homestead	08-THR/THT-02_74	-6.6	-7.1	1.0	10.4	0.3	core		

Table 4 continued

Unit	Sample #	εHf	εHf_i	2 s.e.	$^{206}Pb/^{238}U$ Age (Ma)	2 s.e.	Location	Age[2]	$\delta^{18}O$ ‰[1,2]
Triguero Homestead	08-THR/THT-02_76a	-4.6	-5.0	1.1	10.3	0.2	core		
Triguero Homestead	08-THR/THT-02_76b	-6.0	-6.4	1.0	10.8	0.9	rim		
Triguero Homestead	08-THR/THT-02_77	-5.9	-6.3	1.0	8.7	0.3	core		
Triguero Homestead	08-THR/THT-02_49a	-8.3	-8.7	0.9	14.9	0.6	mantle		
Triguero Homestead	08-THR/THT-02_49b	-8.2	-8.6	0.9			rim		
Triguero Homestead	08-THR/THT-02_51a	-4.9	-5.2	1.0	12.6	0.7	core		
Triguero Homestead	08-THR/THT-02_51b	-5.6	-6.1	1.0	8.8	0.2	rim		
Triguero Homestead	08-THR/THT-02_79a	-6.4	-6.8	1.0	9.6	0.3	core		
Triguero Homestead	08-THR/THT-02_53	-8.5	-8.8	2.0	13.0	0.6	core		
Triguero Homestead	08-THR/THT-02_55	-6.9	-7.2	1.2	13.5	0.7	rim		
Triguero Homestead	08-THR/THT-02_81	-7.3	-7.8	1.0			mantle		
Triguero Homestead	08-THR/THT-02_82	-6.4	-6.8	1.1			core		
Triguero Homestead	08-THR/THT-02_83a	-5.7	-6.1	0.9	10.2	0.4	core		
Triguero Homestead	08-THR/THT-02_83b	-4.7	-5.1	1.6			rim		
Triguero Homestead	08-THR/THT-02_84	-5.7	-6.1	1.0	11.1	0.5	mantle		
Triguero Homestead	08-THR/THT-02_57	-7.1	-7.5	1.0	12.3	0.6	core		
Triguero Homestead	08-THR/THT-02_58	-6.4	-6.8	0.9	13.1	0.4	core		
Triguero Homestead	08-THR/THT-02_59	-10.3	-10.6	1.0	13.3	0.3	core		
Triguero Homestead	08-THR/THT-02_85						core	12.76	-0.4
Triguero Homestead	08-THR/THT-02_85	-7.0	-7.4	1.0	12.2	0.5	mantle		
Triguero Homestead	08-THR/THT-02_85						rim	10.65	1.3
Triguero Homestead	08-THR/THT-02_87	-6.0	-6.4	1.0	12.8	0.6	core		
Triguero Homestead	08-THR/THT-02_88	-7.3	-7.6	1.1	12.3	0.9	core		
Triguero Homestead	08-THR/THT-02_61	-6.0	-6.4	1.0	9.5	0.6	mantle		
Triguero Homestead	08-THR/THT-02_62	-5.8	-6.2	1.0	10.7	0.3	core		

Table 4 continued

Unit	Sample #	εHf	εHf_i	2 s.e.	$^{206}Pb/^{238}U$ Age (Ma)	2 s.e.	Location	Age[2]	$\delta^{18}O$ ‰[1,2]
Triguero Homestead	08-THR/THT-02_92	-5.8	-6.1	1.0			core		
Triguero Homestead	08-THR/THT-02_64	-5.8	-6.2	0.8	10.5	0.6	rim		
Triguero Homestead	08-THR/THT-02_65	-6.1	-6.4	1.0			mantle		
Triguero Homestead	08-THR/THT-02_66a	-6.8	-7.2	1.0	10.5	0.5	rim		
Triguero Homestead	08-THR/THT-02_66b	-7.9	-8.3	1.0	12.5	0.4	core		
Triguero Homestead	08-THR/THT-02_66c	-6.7	-7.1	0.9	12.6	0.6	mantle		
Triguero Homestead	08-THR/THT-02_67	-5.4	-5.8	1.0	10.2	0.2	core	10.80	1.2
Triguero Homestead	08-THR/THT-02_67						mantle	10.63	1
Triguero Homestead	08-THR/THT-02_67						mantle	10.29	1.1
Triguero Homestead	08-THR/THT-02_67						rim	9.82	1.2
Triguero Homestead	08-THR/THT-02_93	-6.2	-6.6	1.0	12.8	0.7	core		
Triguero Homestead	08-THR/THT-02_95	-5.9	-6.3	0.9			core		
Triguero Homestead	08-THR/THT-02_96	-5.8	-6.2	1.0			core		
Triguero Homestead	08-THR/THT-02_69	-3.4	-3.8	1.1			core		
Triguero Homestead	08-THR/THT-02_70a	-7.0	-7.4	1.1			rim		
Triguero Homestead	08-THR/THT-02_70b	-8.4	-8.8	1.1	11.4	0.2	mantle		
Triguero Homestead	08-THR/THT-02_70c	-7.3	-7.6	1.1	13.6	0.5	core		
Marys Creek	01-MCR-02_01a	-6.0	-6.4	1.1	12.7	0.3	core		
Marys Creek	01-MCR-02_01b	-4.6	-4.9	2.1			rim		
Marys Creek	01-MCR-02_29a	-10.1	-10.5	1.2	12.3	0.4	core		
Marys Creek	01-MCR-02_29b	-3.6	-4.0	1.0	12.5	0.2	rim		
Marys Creek	01-MCR-02_28	-39.1	-39.5	2.3	11.1	0.2	mantle		
Marys Creek	01-MCR-02_05	-7.8	-8.1	1.5	11.8	0.3	rim		

Table 4 continued

Unit	Sample #	εHf	εHf_i	2 s.e.	$^{206}Pb/^{238}U$ Age (Ma)	2 s.e.	Location	Age[2]	$\delta^{18}O$ ‰[1,2]
Marys Creek	01-MCR-02_06a	-15.1	-15.5	1.2	11.4	0.2	core		
Marys Creek	01-MCR-02_06b	-1.9	-2.4	1.1	10.7	0.7	rim		
Marys Creek	01-MCR-02_10a	-6.3	-6.7	1.3	11.1	0.3	core		
Marys Creek	01-MCR-02_10b	-5.4	-5.7	1.2	11.0	0.2	rim		
Marys Creek	01-MCR-02_12	-4.7	-5.1	1.2	12.5	0.3	mantle		
Marys Creek	01-MCR-02_38a	-4.7	-5.1	1.3	11.9	0.2	rim		
Marys Creek	01-MCR-02_38b	-3.8	-4.2	1.4	12.0	0.5	rim		
Marys Creek	01-MCR-02_40a	-9.9	-10.3	1.2	13.1	0.3	core		
Marys Creek	01-MCR-02_40b	-3.9	-4.3	1.0	12.1	0.4	mantle		
Marys Creek	01-MCR-02_40c	-7.3	-7.7	1.1	11.8	0.2	rim		
Marys Creek	01-MCR-02_44a	-5.5	-5.8	1.4	11.7	0.3	core		
Marys Creek	01-MCR-02_44b	-6.2	-6.6	1.8	11.5	0.4	mantle		
Marys Creek	01-MCR-02_19a	-9.0	-9.4	1.1	11.1	0.3	core		
Marys Creek	01-MCR-02_19b	-9.4	-9.8	1.0	11.3	0.2	mantle		
Marys Creek	01-MCR-02_21a	-9.8	-10.2	1.1	11.3	0.3	core		
Marys Creek	01-MCR-02_21b	-7.2	-7.6	0.9	11.8	0.2	rim		
Marys Creek	01-MCR-02_50	-9.8	-10.1	1.0	11.8	0.3	core		
Marys Creek	01-MCR-02_58a	-9.7	-10.0	1.4	13.0	0.3	mantle		
Marys Creek	01-MCR-02_58b	-8.9	-9.2	1.2	12.6	0.8	rim		
Marys Creek	01-MCR-02_62	-8.7	-9.1	1.5	11.8	0.4	core		
Marys Creek	01-MCR-02_69	1.3	0.96	1.6	11.7	0.7	mantle		
Marys Creek	01-MCR-02_70a	-11.3	-11.7	1.2	11.5	0.2	core		
Marys Creek	01-MCR-02_70b	-9.4	-9.8	1.0	10.7	0.2	rim		
Marys Creek	01-MCR-02_71a	-4.9	-5.3	1.4	11.3	0.2	mantle		
Marys Creek	01-MCR-02_71						mantle	10.78	0.9

Table 4 continued

Unit	Sample #	εHf	εHf_i	2 s.e.	$^{206}Pb/^{238}U$ Age (Ma)	2 s.e.	Location	Age[2]	$\delta^{18}O$ ‰[1,2]
Marys Creek	01-MCR-02_71						core	10.87	1.5
Marys Creek	01-MCR-02_71						mantle	10.47	1.3
Marys Creek	01-MCR-02_71b	-7.9	-8.3	1.2	10.8	0.2	rim		
Marys Creek	01-MCR-02_72				10.7	0.4	core		
Marys Creek	01-MCR-02_73a	-6.0	-6.4	1.0	11.8	0.4	core		
Marys Creek	01-MCR-02_73b	-5.9	-6.3	1.3	12.3	0.4	rim		
Marys Creek	01-MCR-02_75a	-9.7	-10.0	1.3	11.3	0.2	core		
Marys Creek	01-MCR-02_75b	-6.1	-6.4	1.2	11.2	0.7	rim		
Marys Creek	01-MCR-02_76a	-7.6	-8.0	1.3	11.3	0.3	core		
Marys Creek	01-MCR-02_76b	-6.5	-6.8	1.0	11.8	0.3	rim		
Marys Creek	01-MCR-02_82a	-7.9	-8.3	1.2	11.5	0.2	mantle		
Marys Creek	01-MCR-02_82b	-7.7	-8.1	1.2	10.9	0.3	rim		
Marys Creek	01-MCR-02_85	-12.8	-13.2	1.6	12.1	0.2	core		
Marys Creek	01-MCR-02_87a	-8.6	-9.00	1.2	12.4	0.5	core		
Marys Creek	01-MCR-02_87						core	9.68	1.1
Marys Creek	01-MCR-02_87						mantle	10.90	1.5
Marys Creek	01-MCR-02_87b	-5.6	-6.05	1.2	11.3	0.2	mantle		
Marys Creek	01-MCR-02_87						mantle	9.55	1.7
Marys Creek	01-MCR-02_87c	-5.3	-5.73	1.1	11.5	0.3	rim		
Marys Creek	01-MCR-02_87						rim	9.82	-0.3
Marys Creek	01-MCR-02_87						rim	11.40	-0.7
Marys Creek	01-MCR-02_91	-6.5	-6.85	1.1	12.0	0.4	core		

Epsilon Hf values were calculated using CHUR values of Bouvier *et al.* (2008) and the ^{176}Lu decay constant of Söderlund *et al.* (2004).

1. CPT $\delta^{18}O$ values (Cathey, 2011)

2. Lava ages and $\delta^{18}O$ values (Seligman, 2012)

APPENDIX B

CATHODOLUMINESCENCE IMAGES OF BRUNEAU-JARBIDGE ZIRCONS

The following figures (Figures 27-79) are cathodoluminescence (CL) and back-scattered electron (BSE) images of zircons analyzed by laser ablation in this study. Laser ablation sites are marked as red circles scaling to 53 μm in diameter. Red numbers are used for εHf values and yellow numbers for $^{206}Pb/^{238}U$ ages. Measurements taken in previous studies are marked as yellow circles or ovals. Blue values indicate $\delta^{18}O$ values from Cathey for CTPX (2011) and Seligman for lavas (2012). Yellow numbers with asterisks are $^{206}Pb/^{238}U$ values from Seligman (2012). Zircons were imaged prior to this study by Henrietta Cathey (CPT X) and Barbara Nash (Lavas).

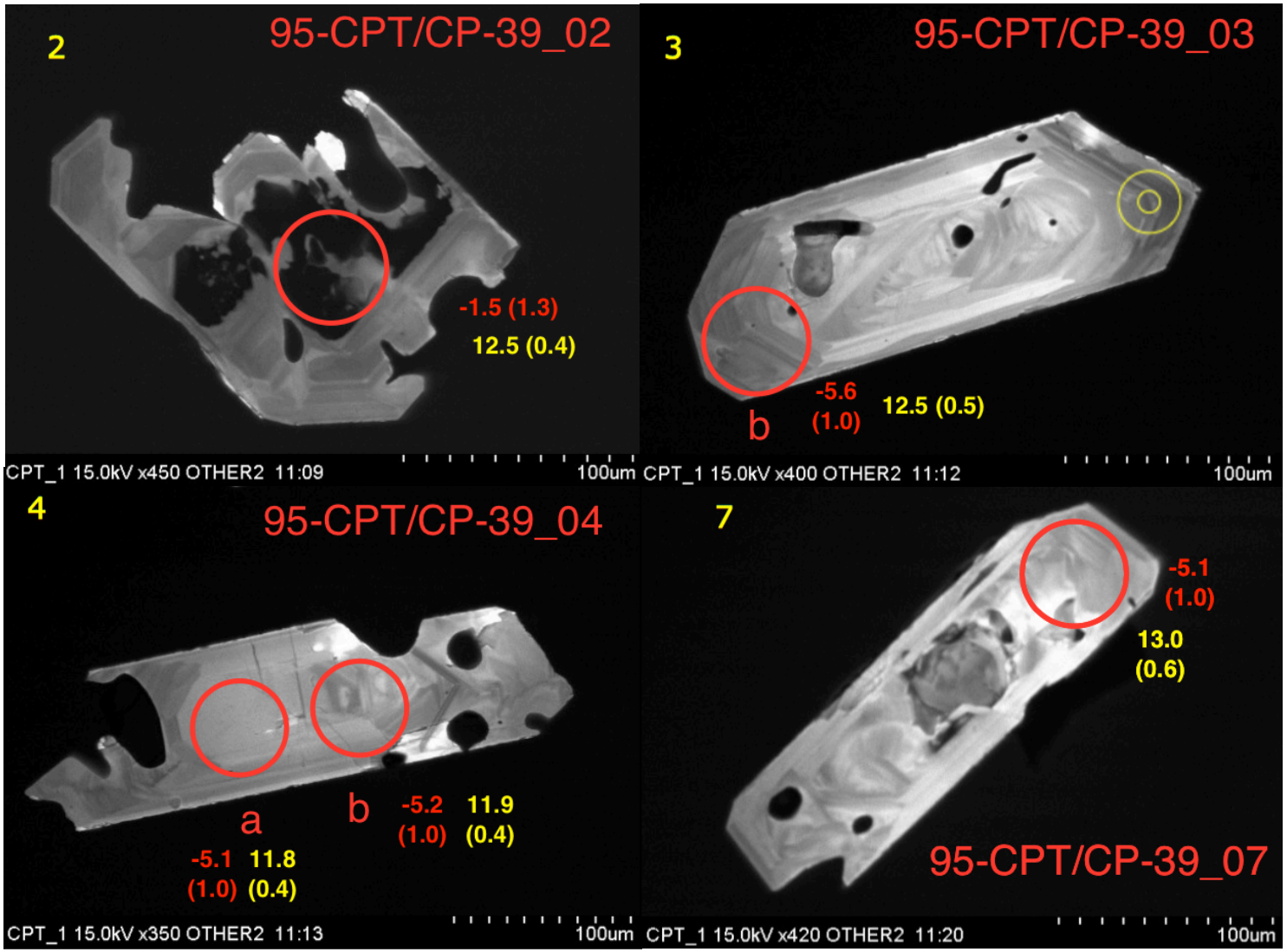

Figure 27. Cougar Point Tuff X zircons

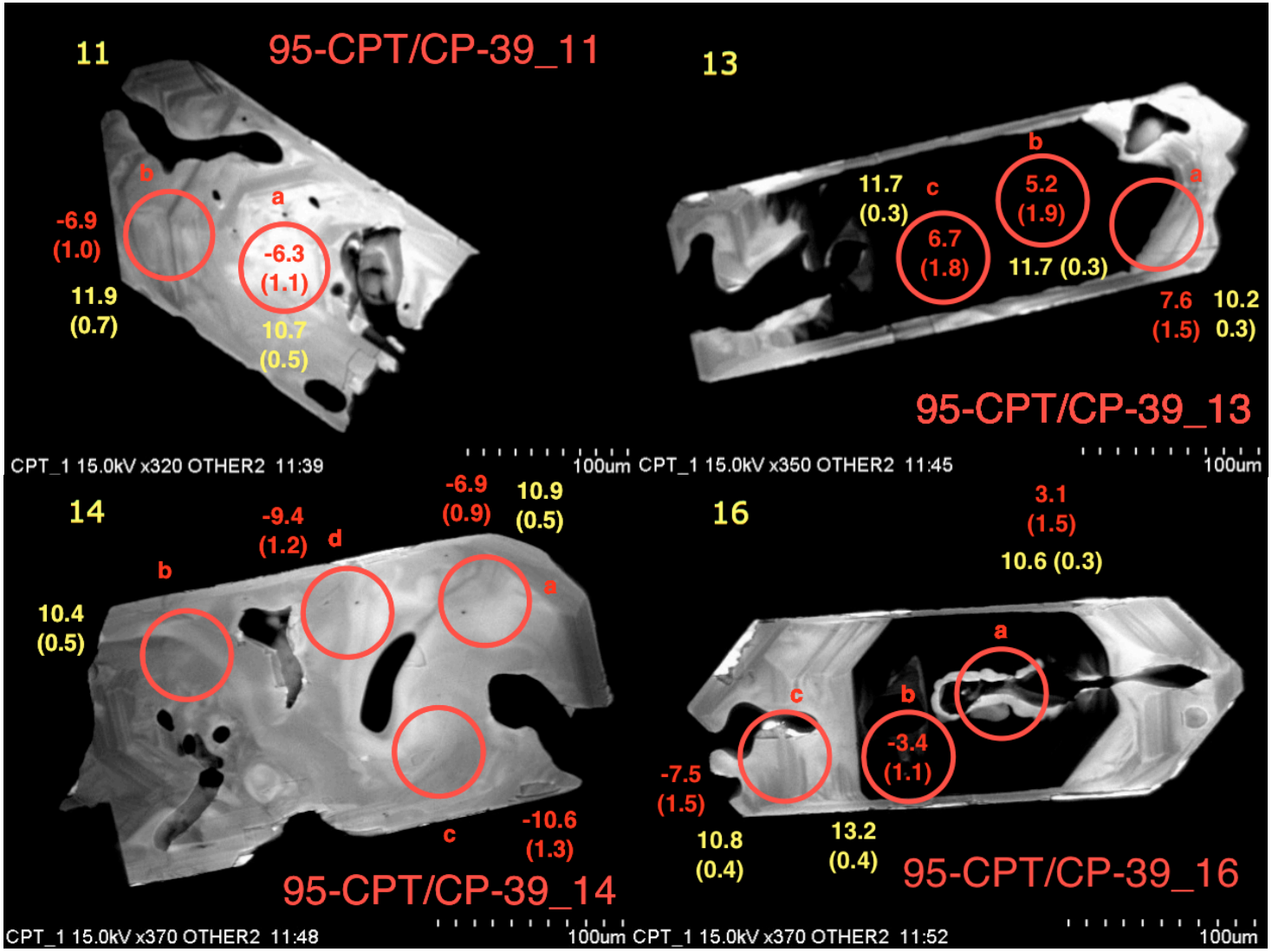

Figure 28. Cougar Point Tuff X zircons

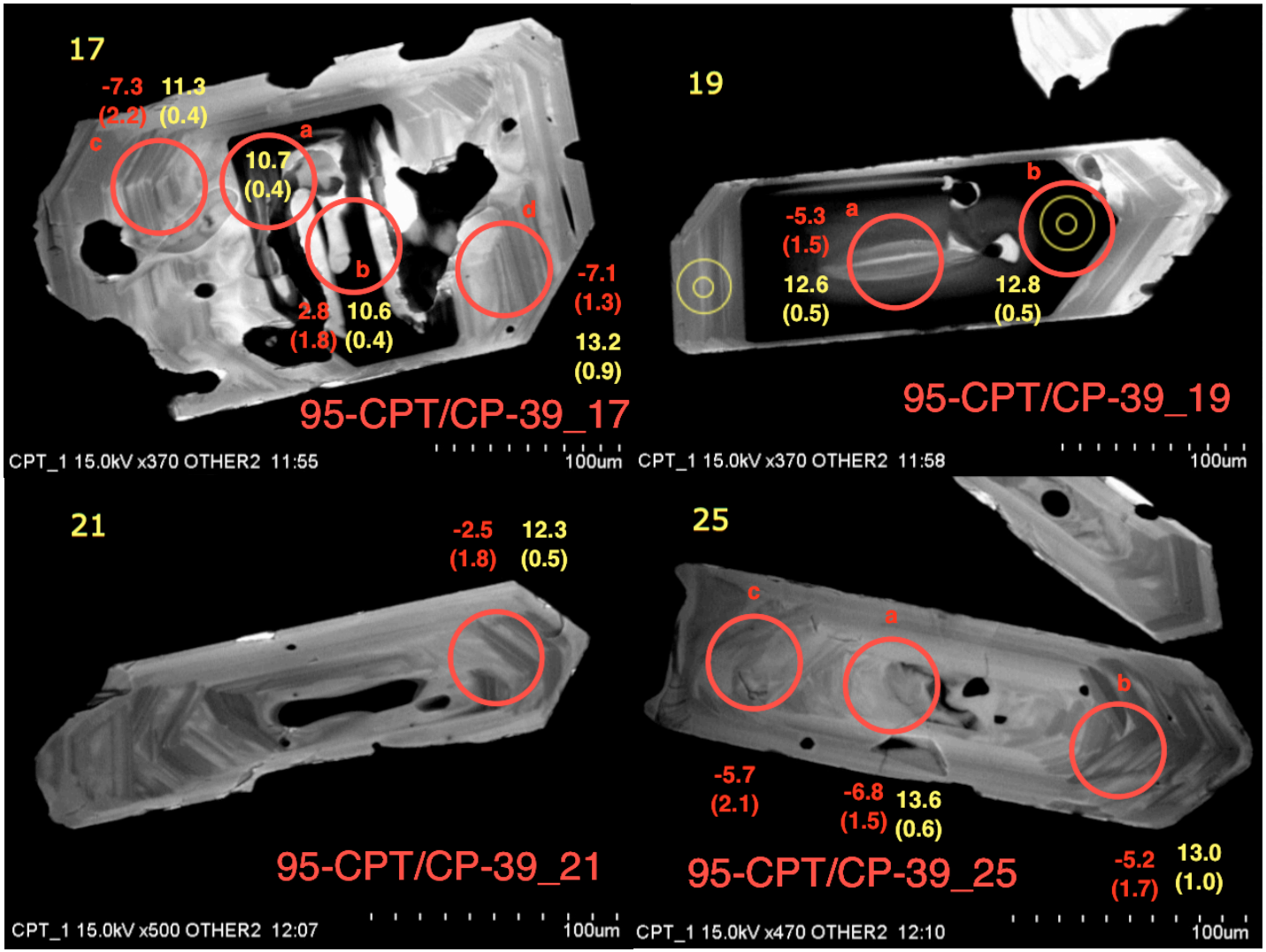

Figure 29. Cougar Point Tuff X zircons

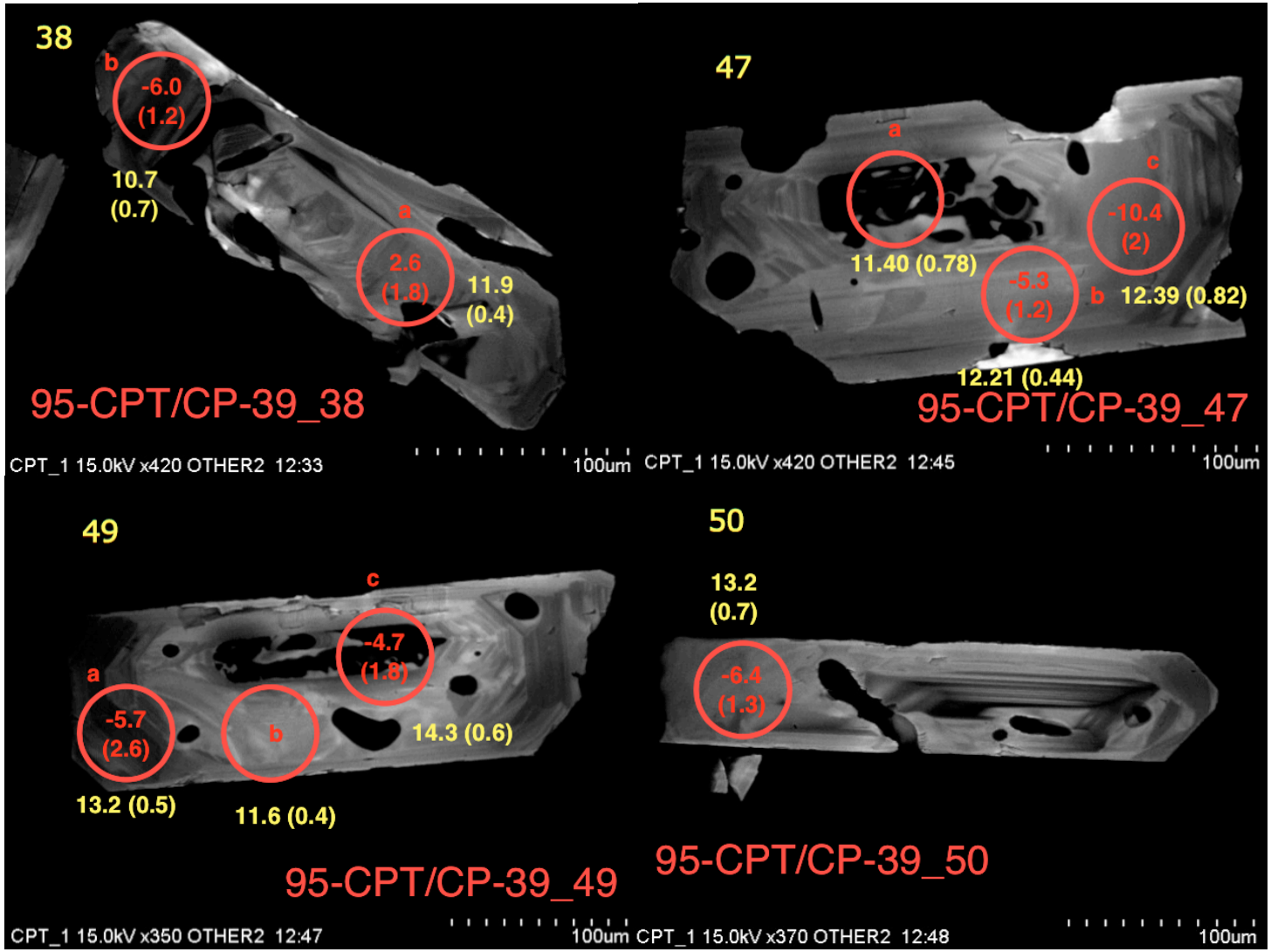

Figure 30. Cougar Point Tuff X zircons

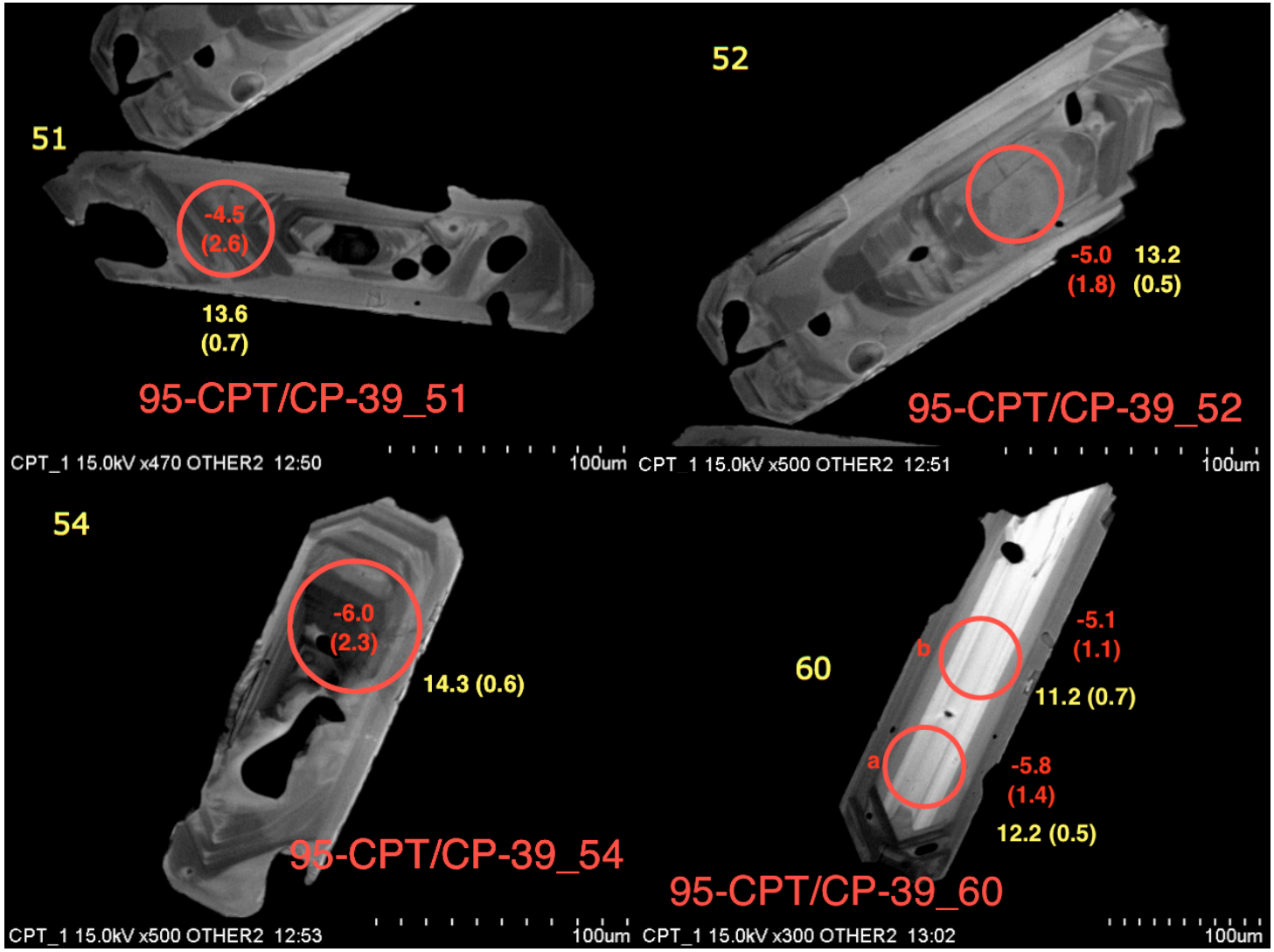

Figure 31. Cougar Point Tuff X zircons

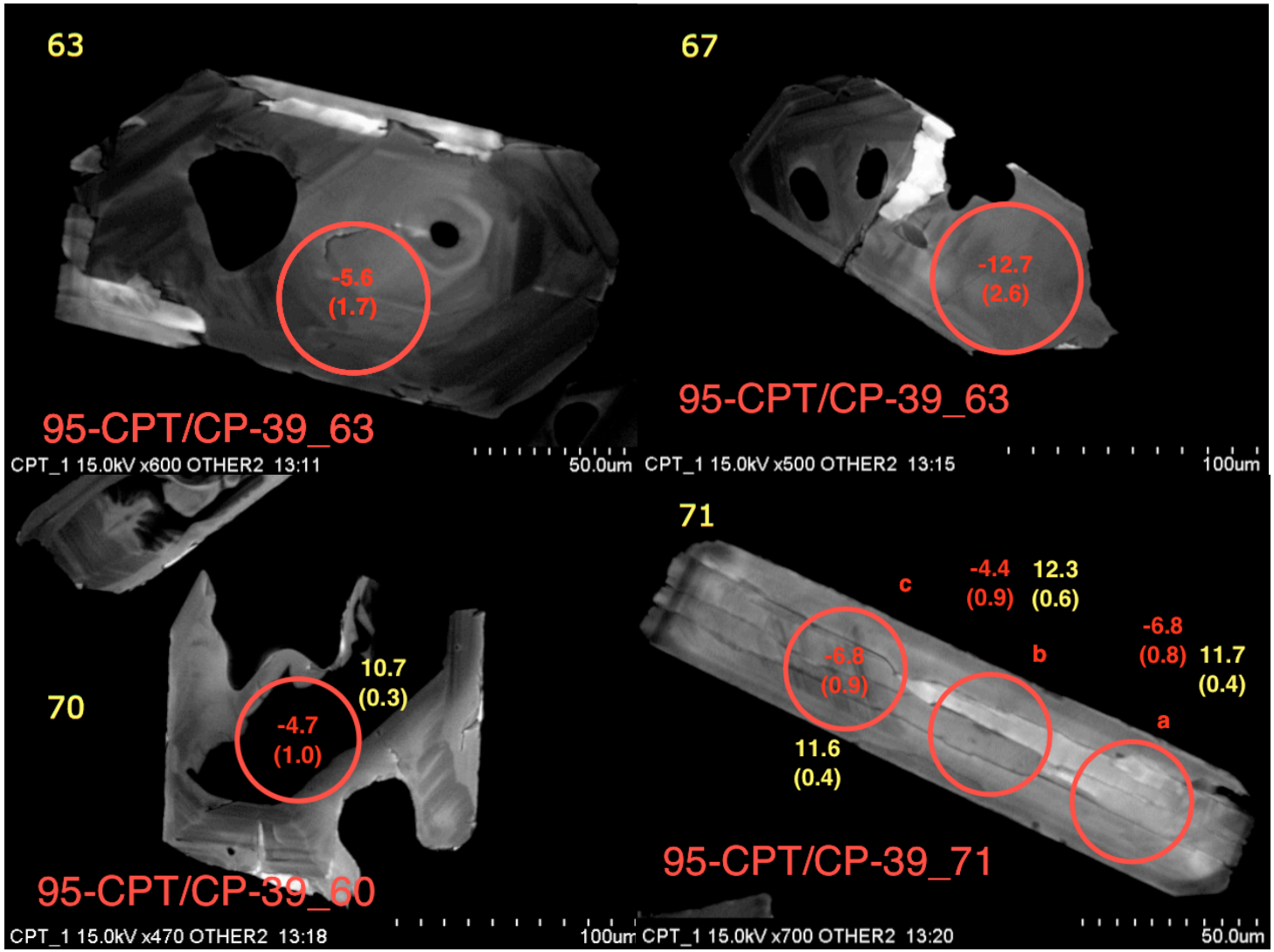

Figure 32. Cougar Point Tuff X zircons

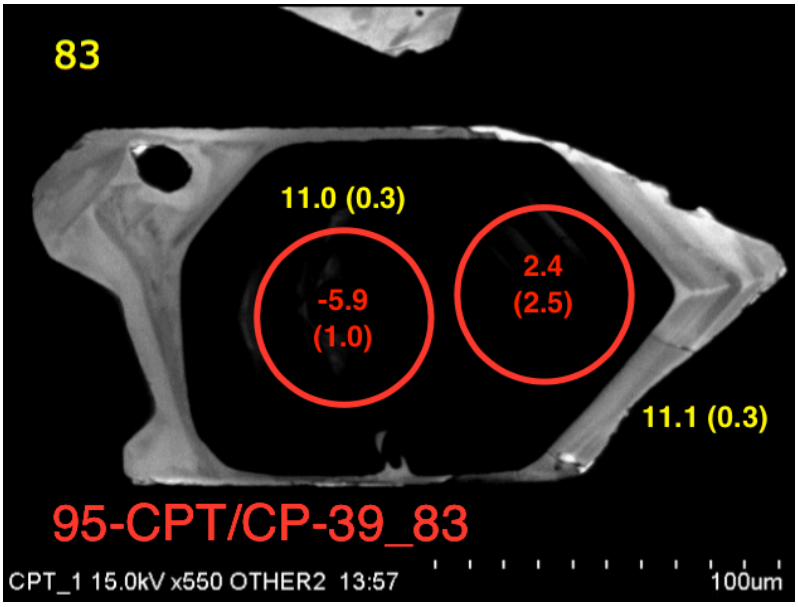

Figure 33. Cougar Point Tuff X zircons

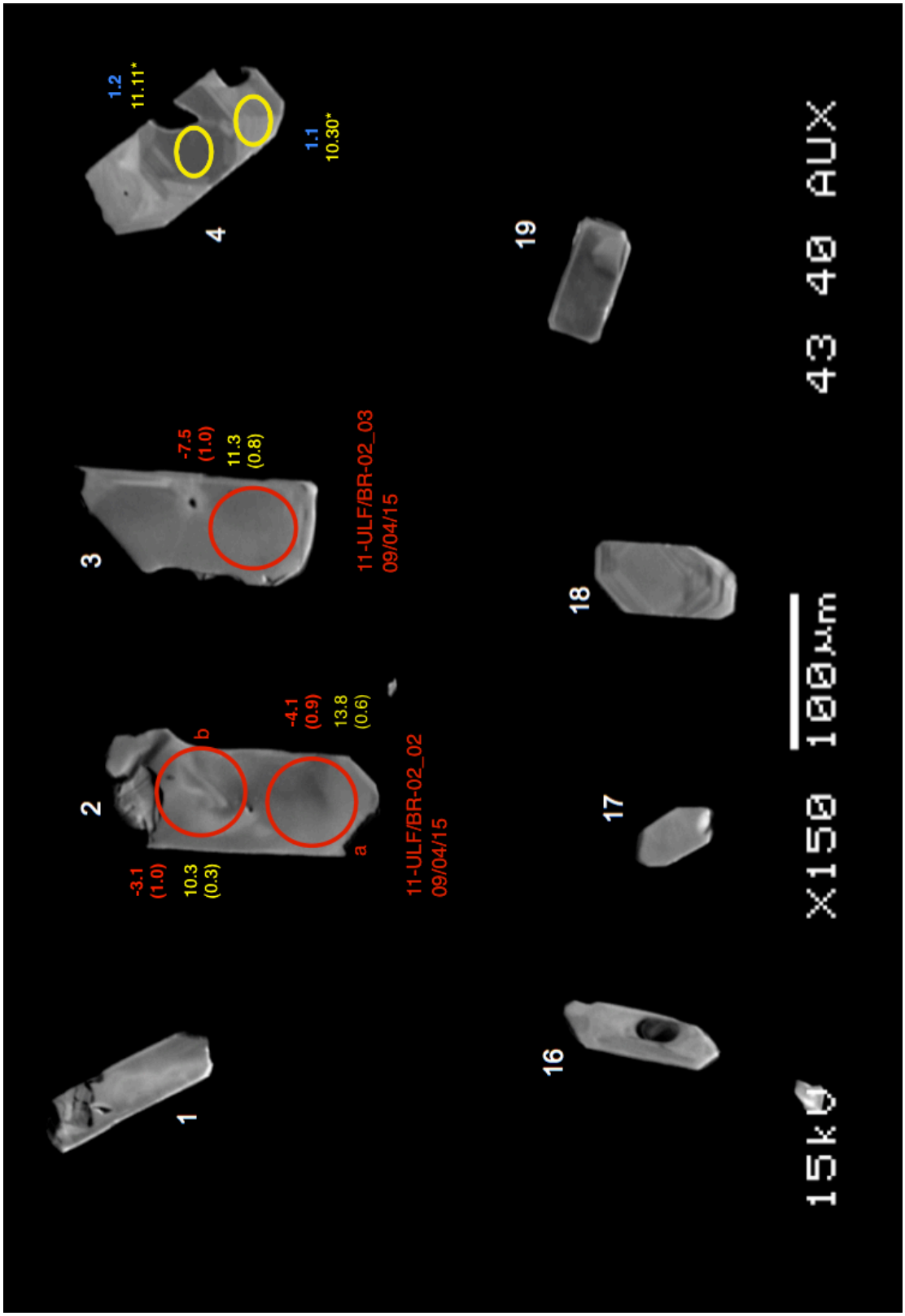

Figure 34. Lower lava flow zircons

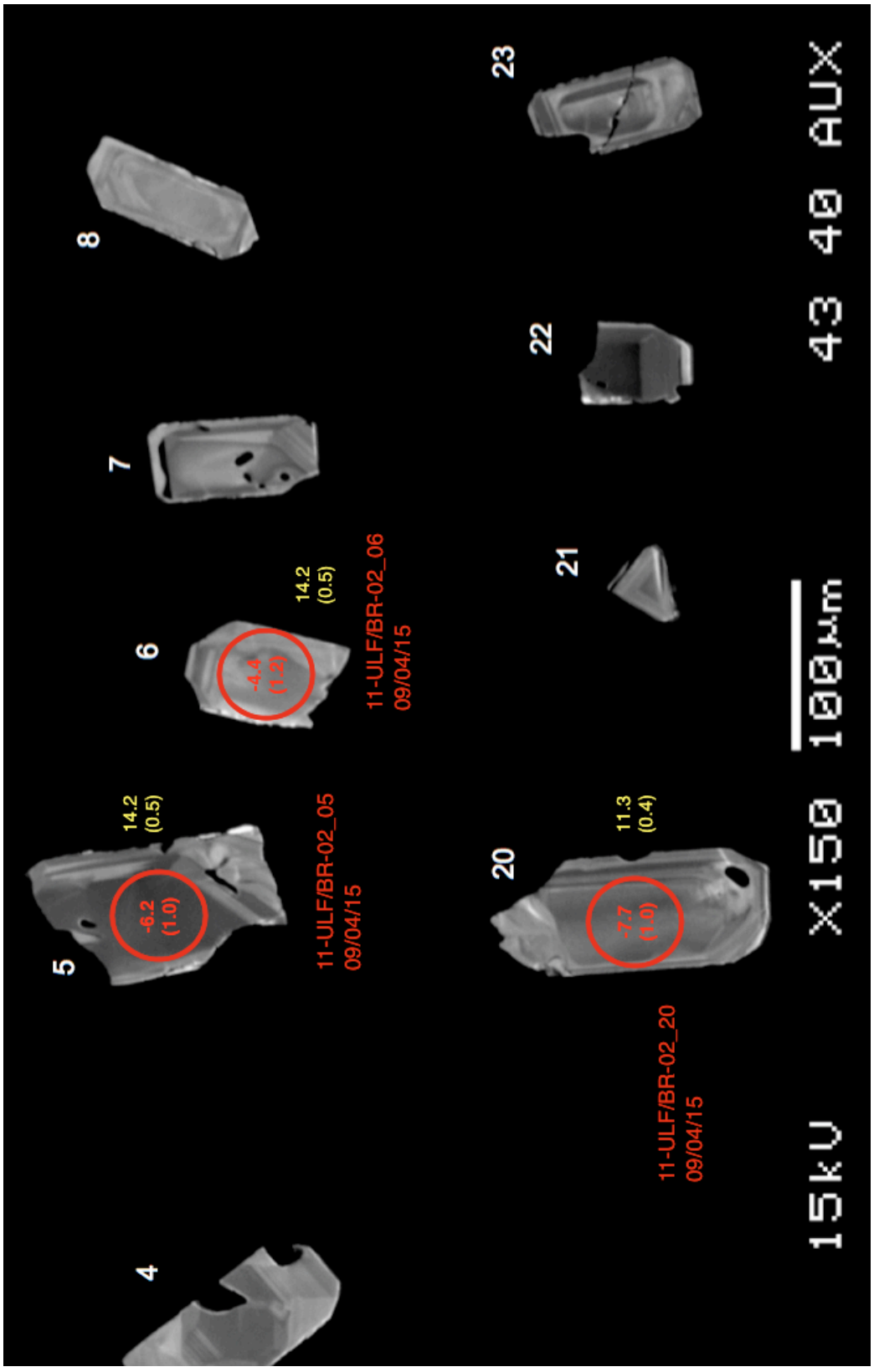

Figure 35. Lower lava flow zircons

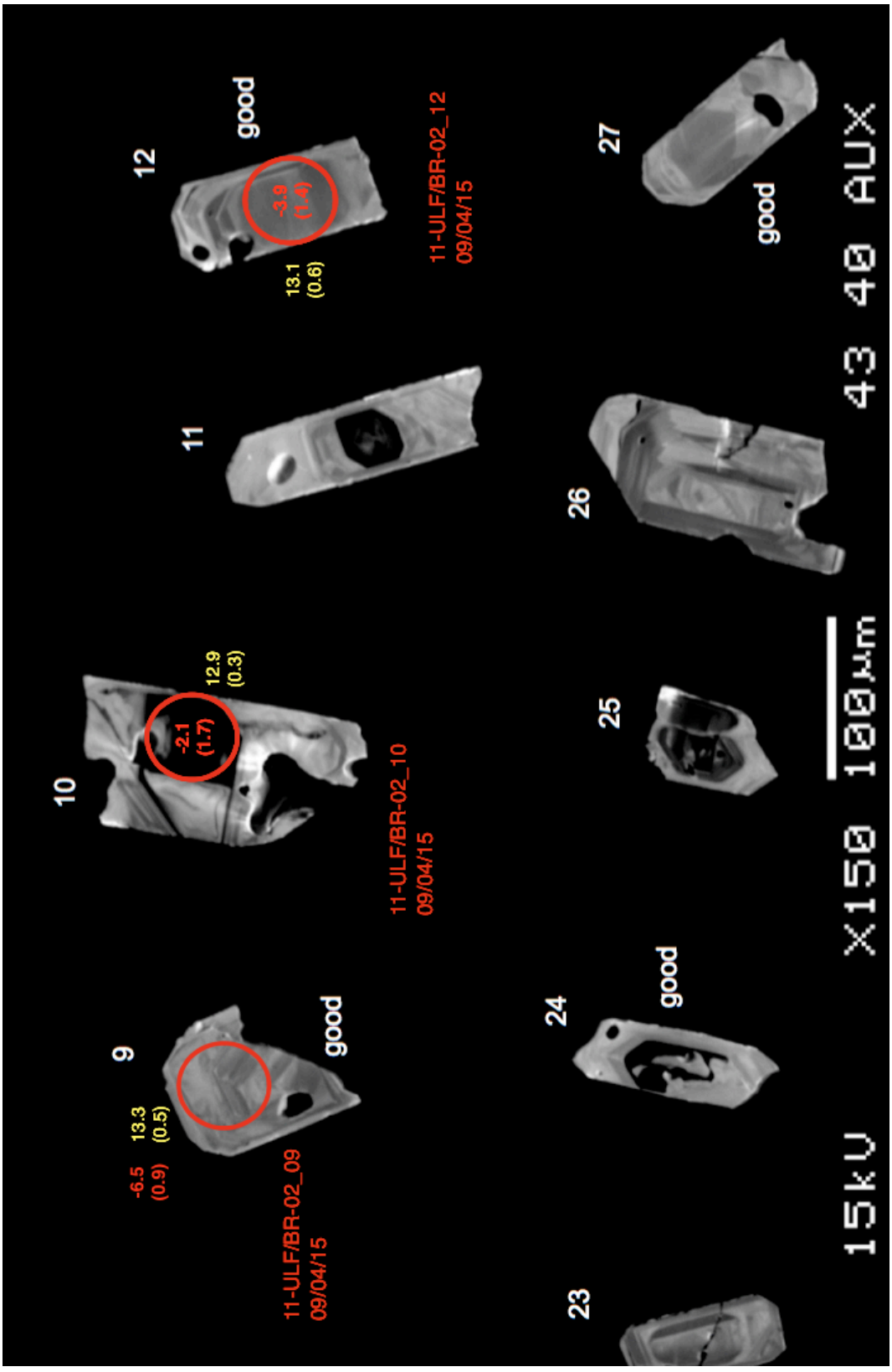

Figure 36. Lower lava flow zircons

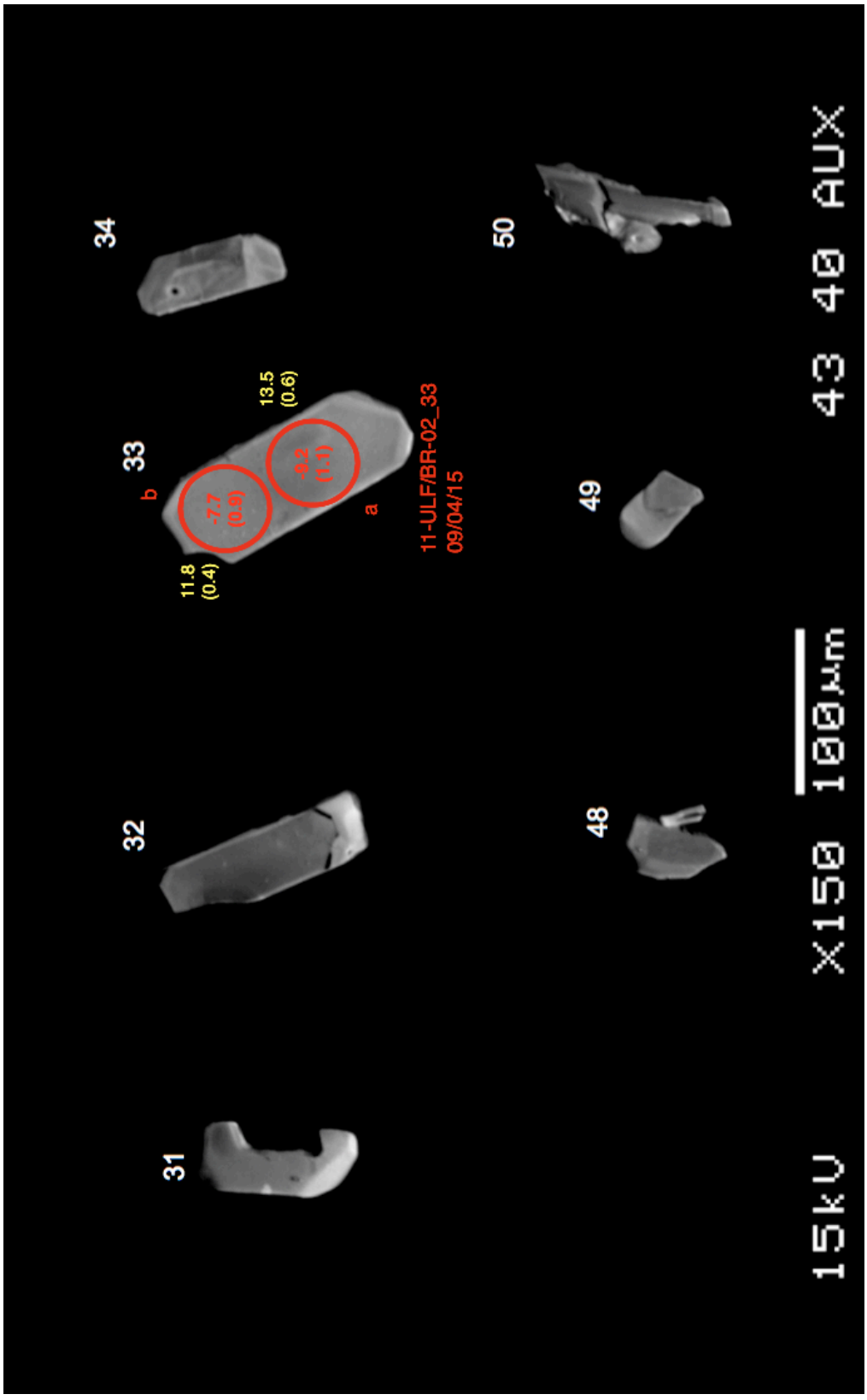

Figure 37. Lower lava flow zircons

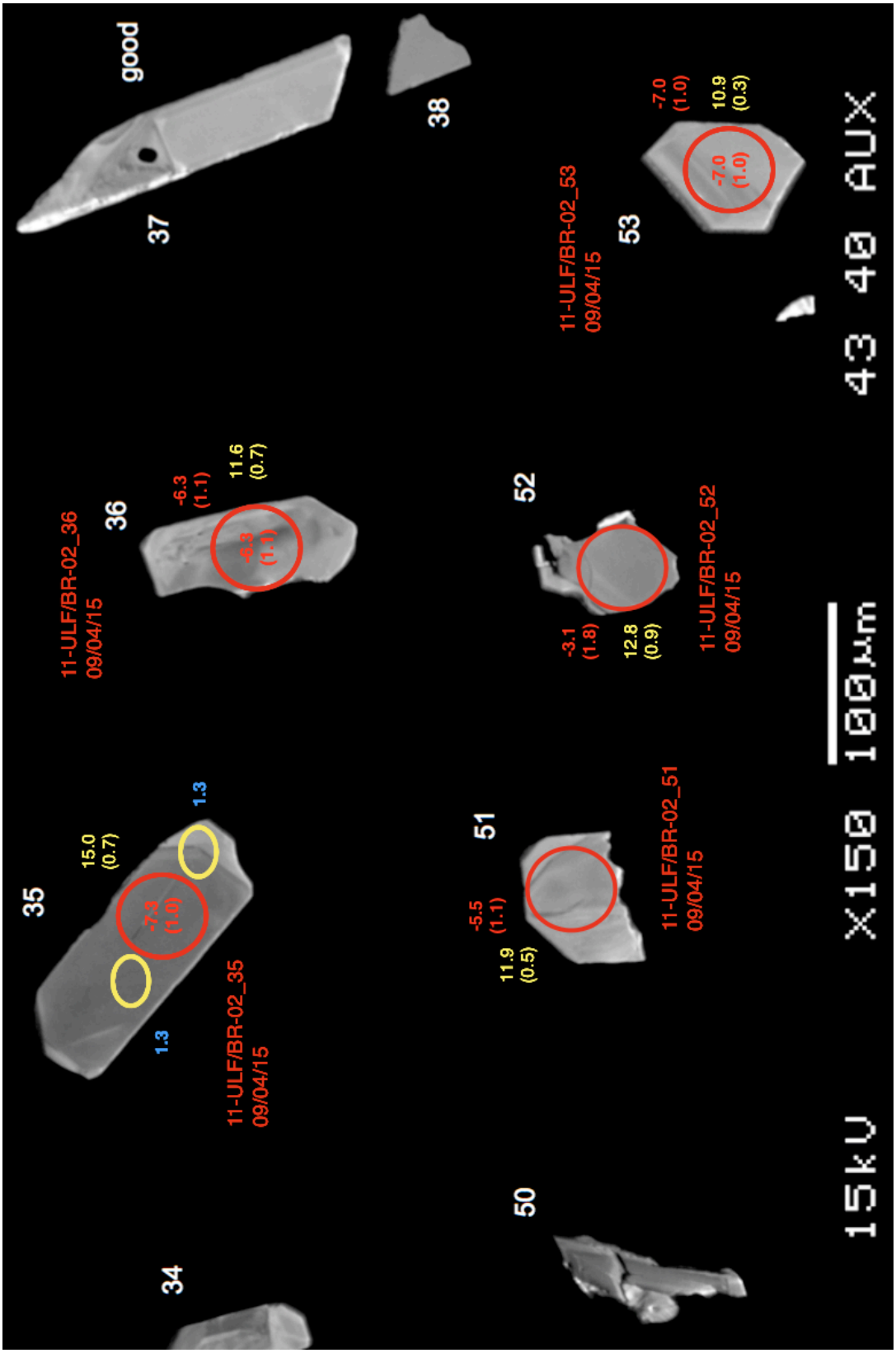

Figure 38. Lower lava flow zircons

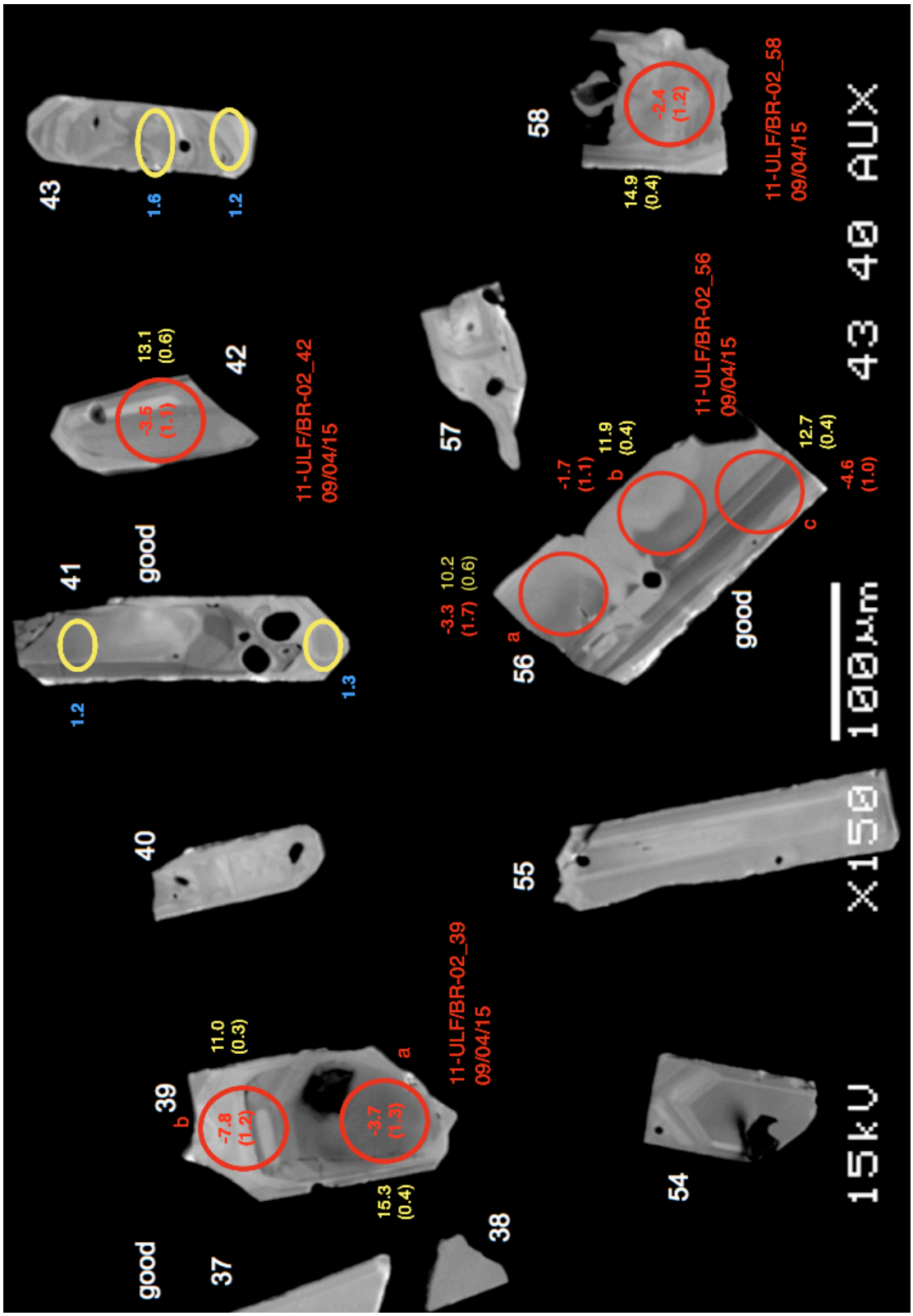

Figure 39. Lower lava flow zircons

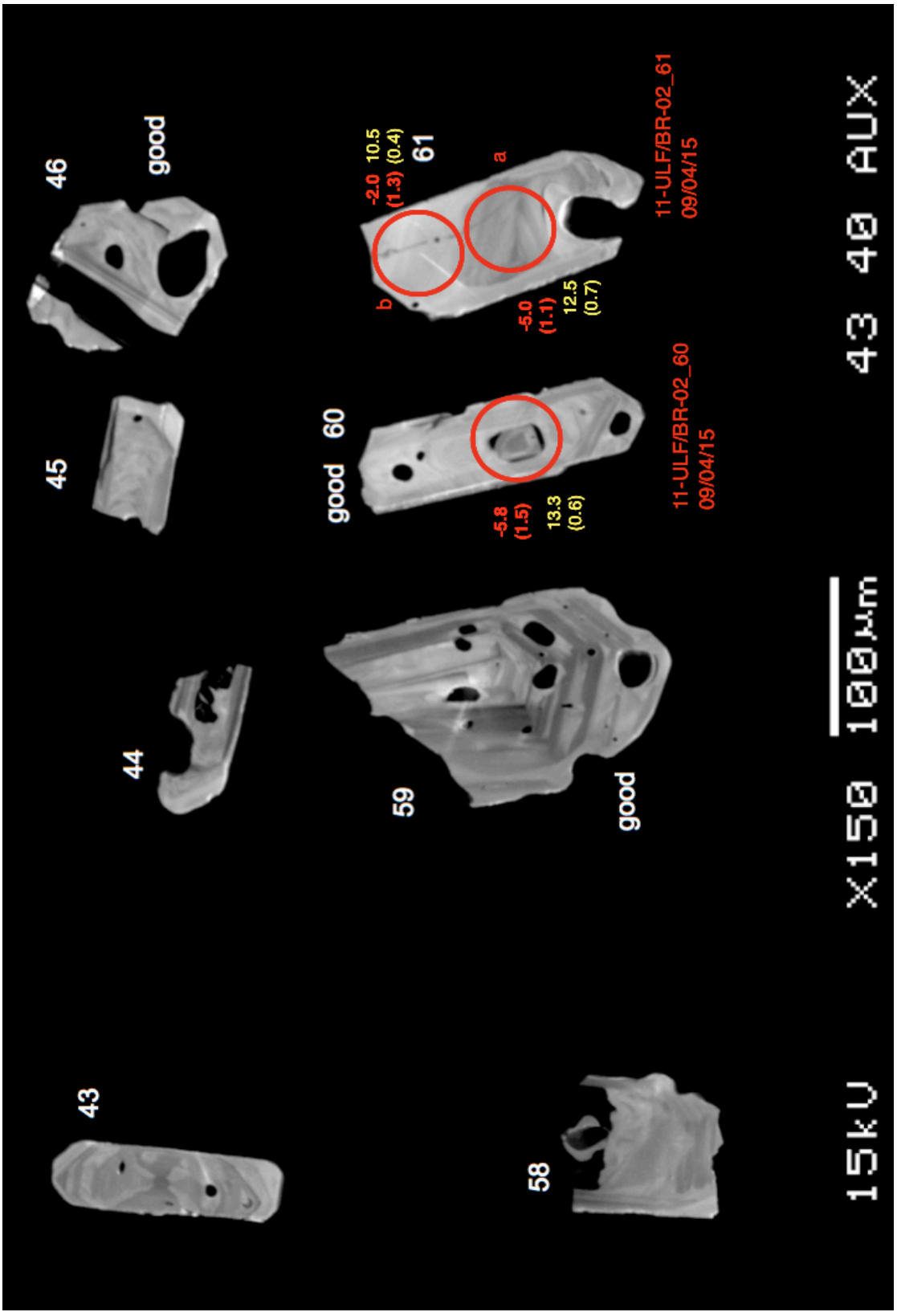

Figure 40. Lower lava flow zircons

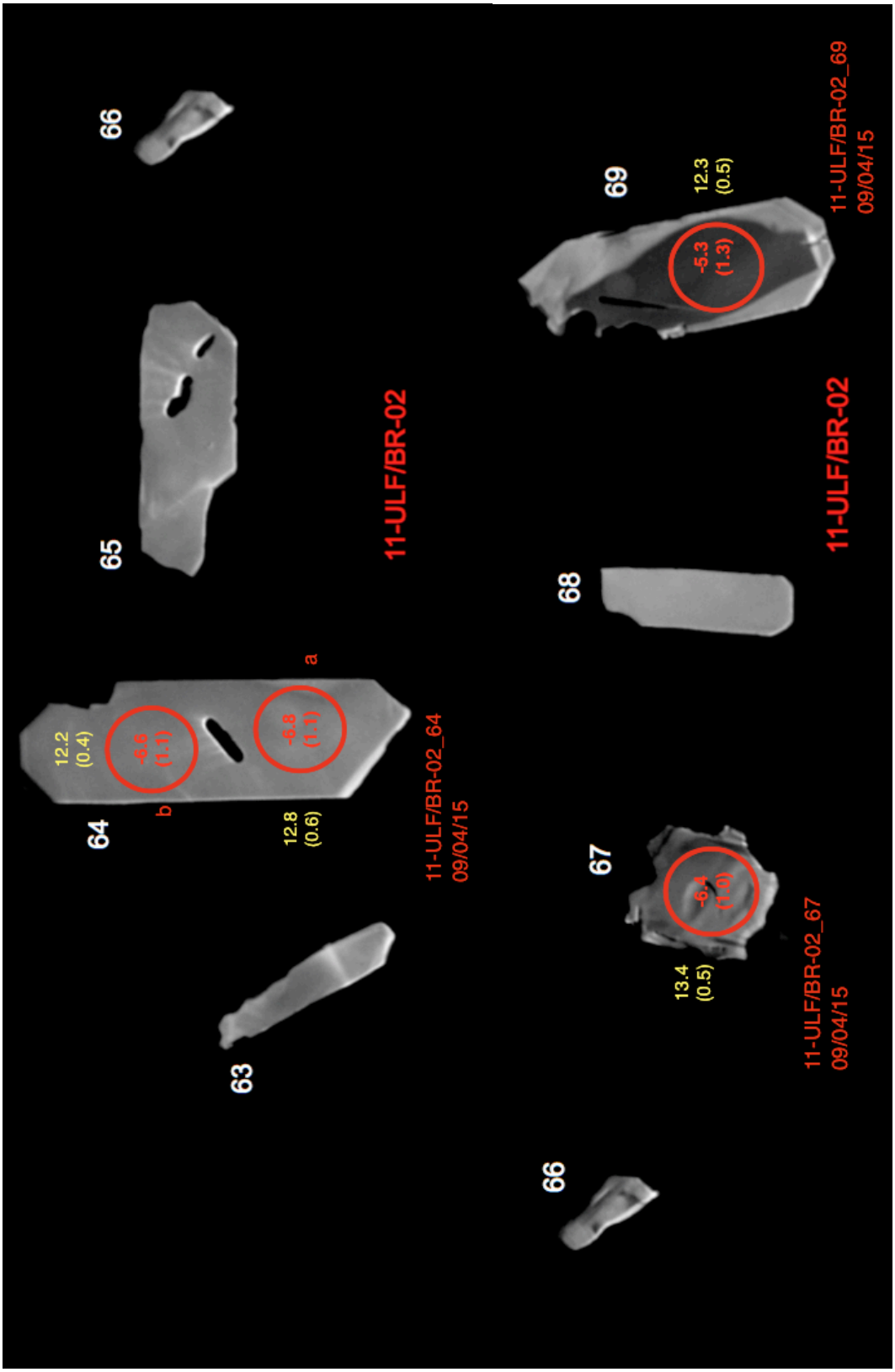

Figure 41. Lower lava flow zircons

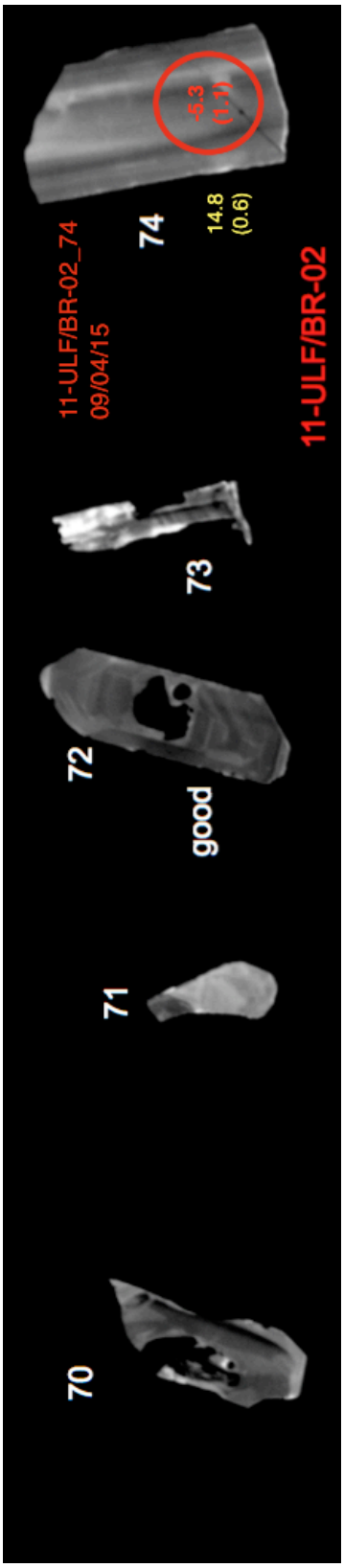

Figure 42. Lower lava flow zircons

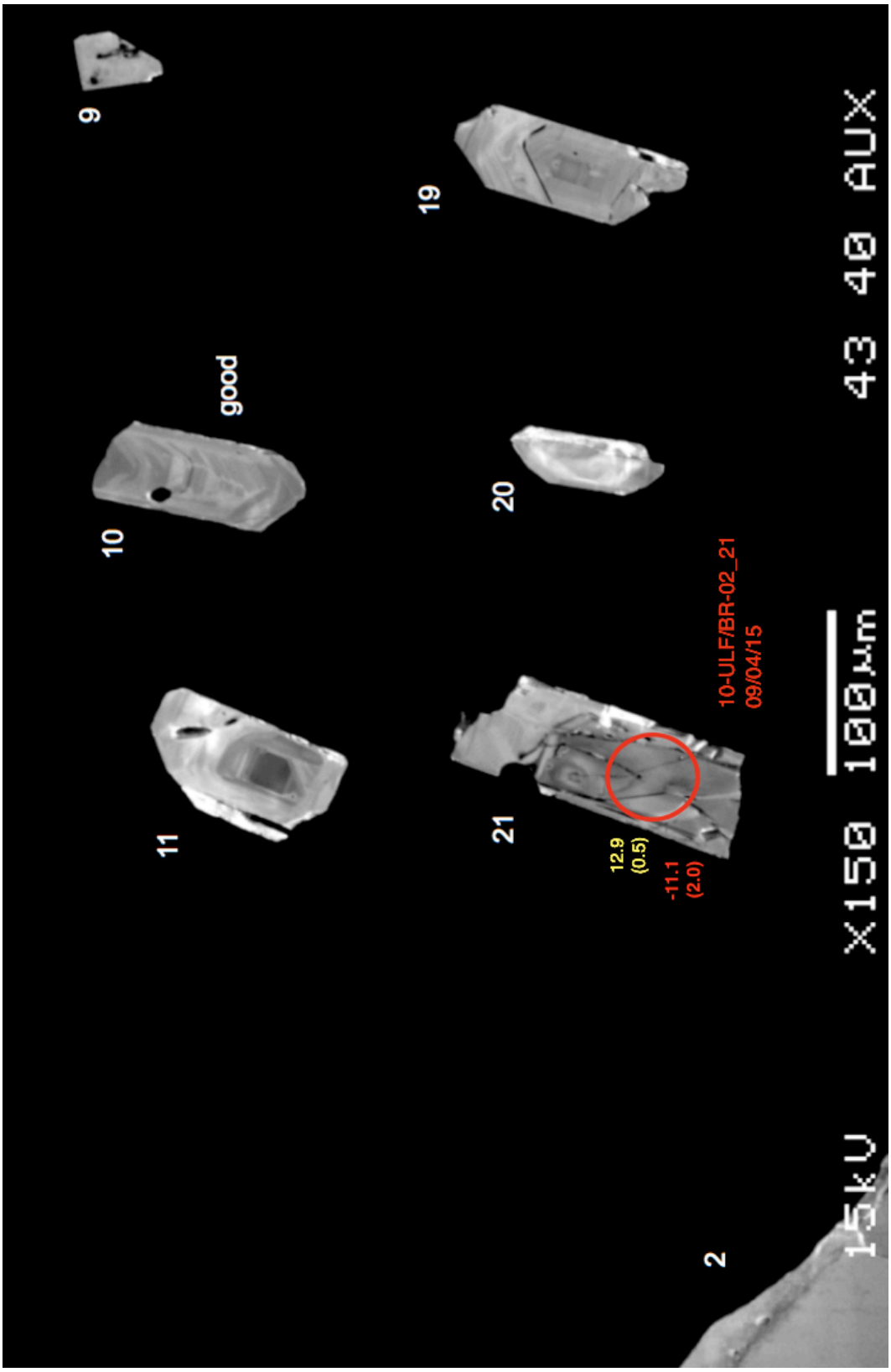

Figure 43. Upper lava flow zircons

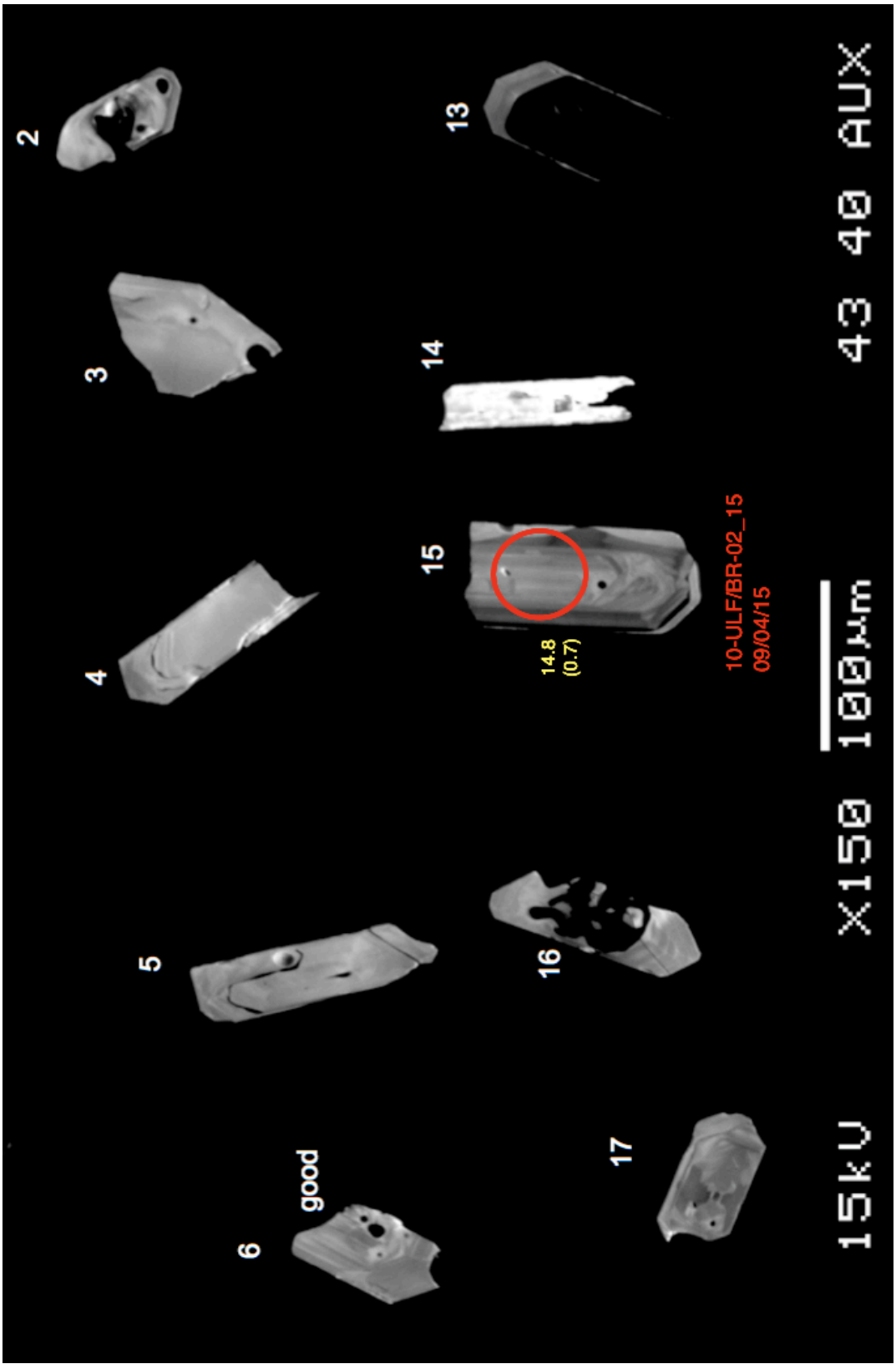

Figure 44. Upper lava flow zircons

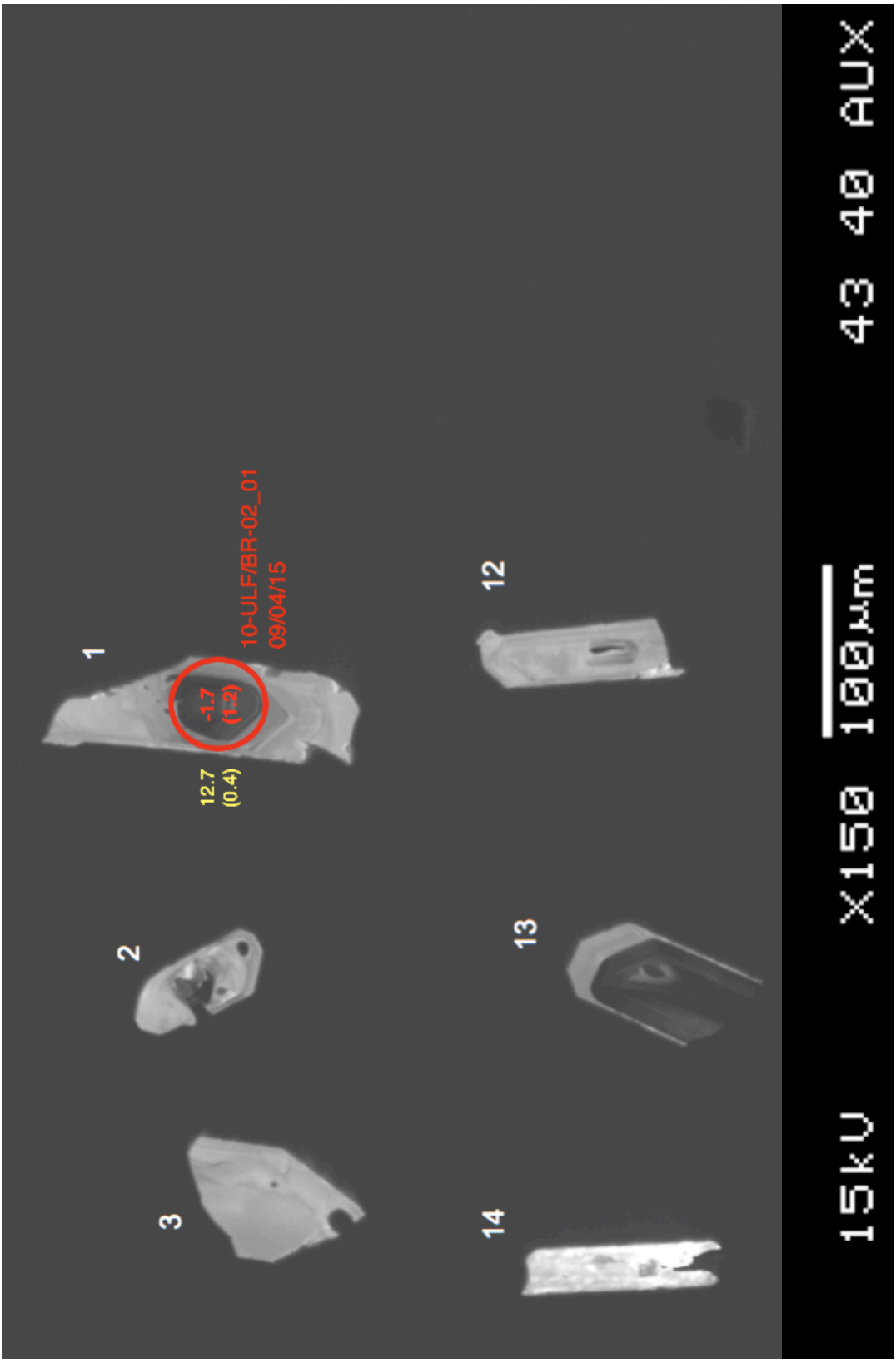

Figure 45. Upper lava flow zircons

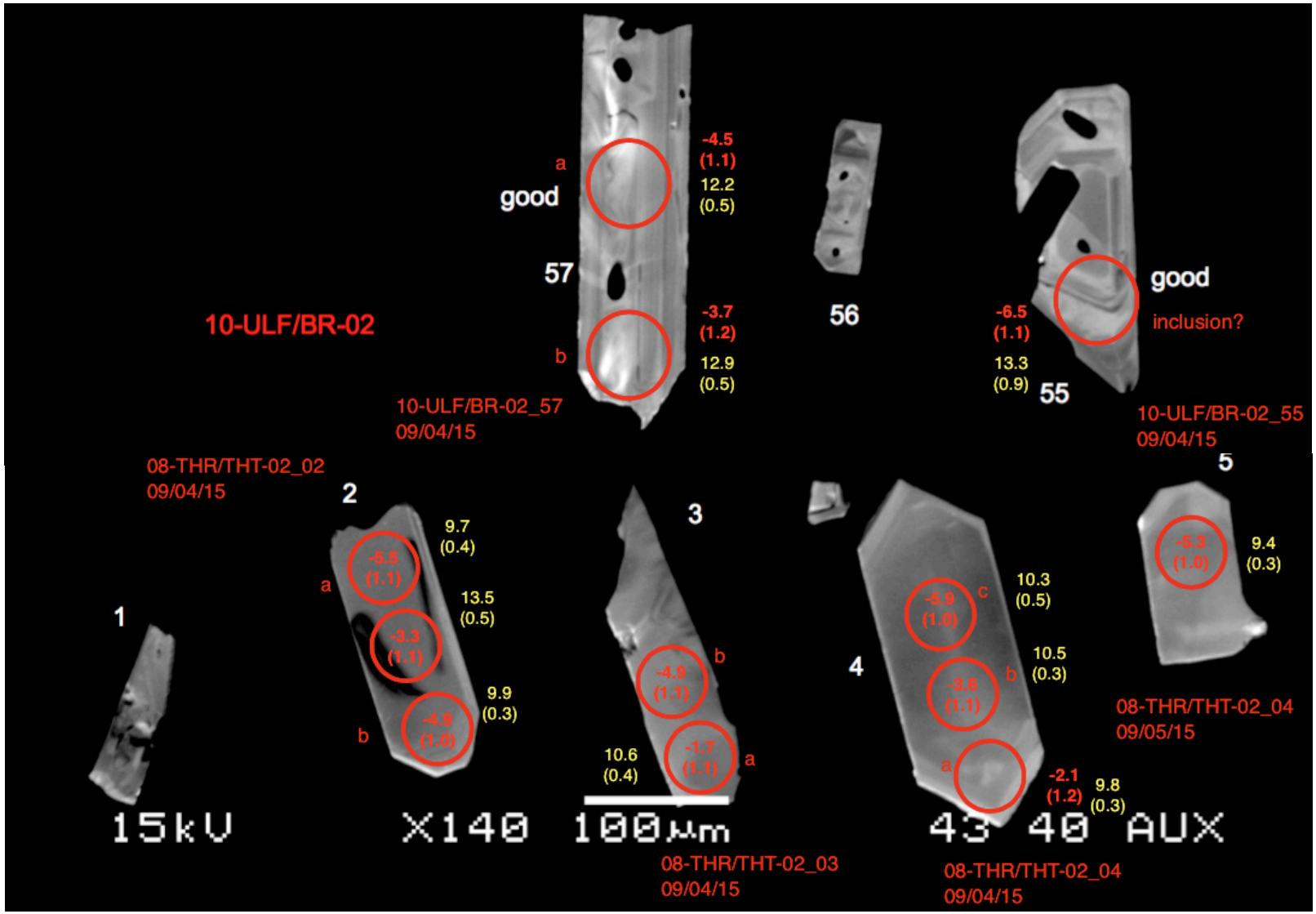

Figure 46. Triguero Homestead rhyolite zircons

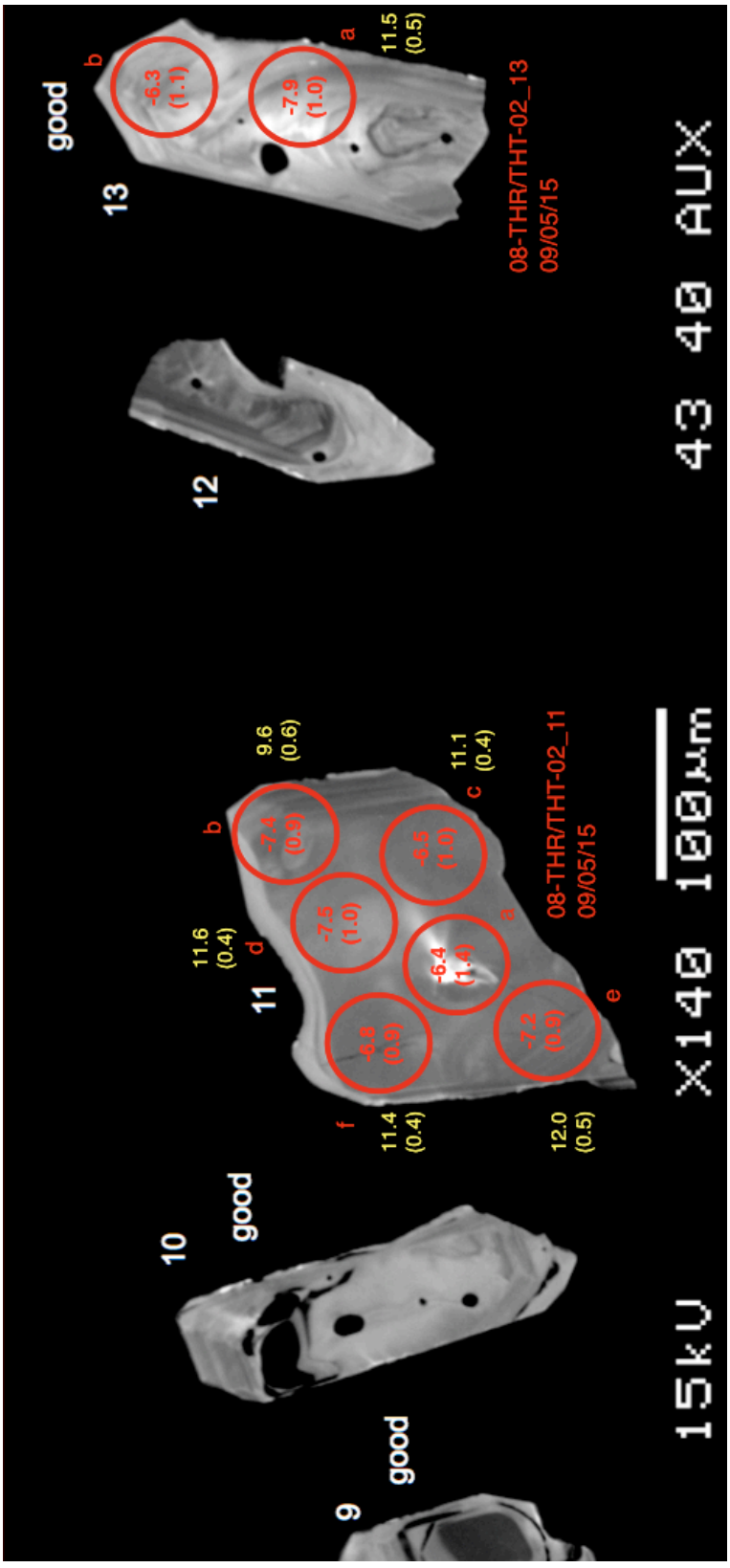

Figure 47. Triguero Homestead rhyolite zircons

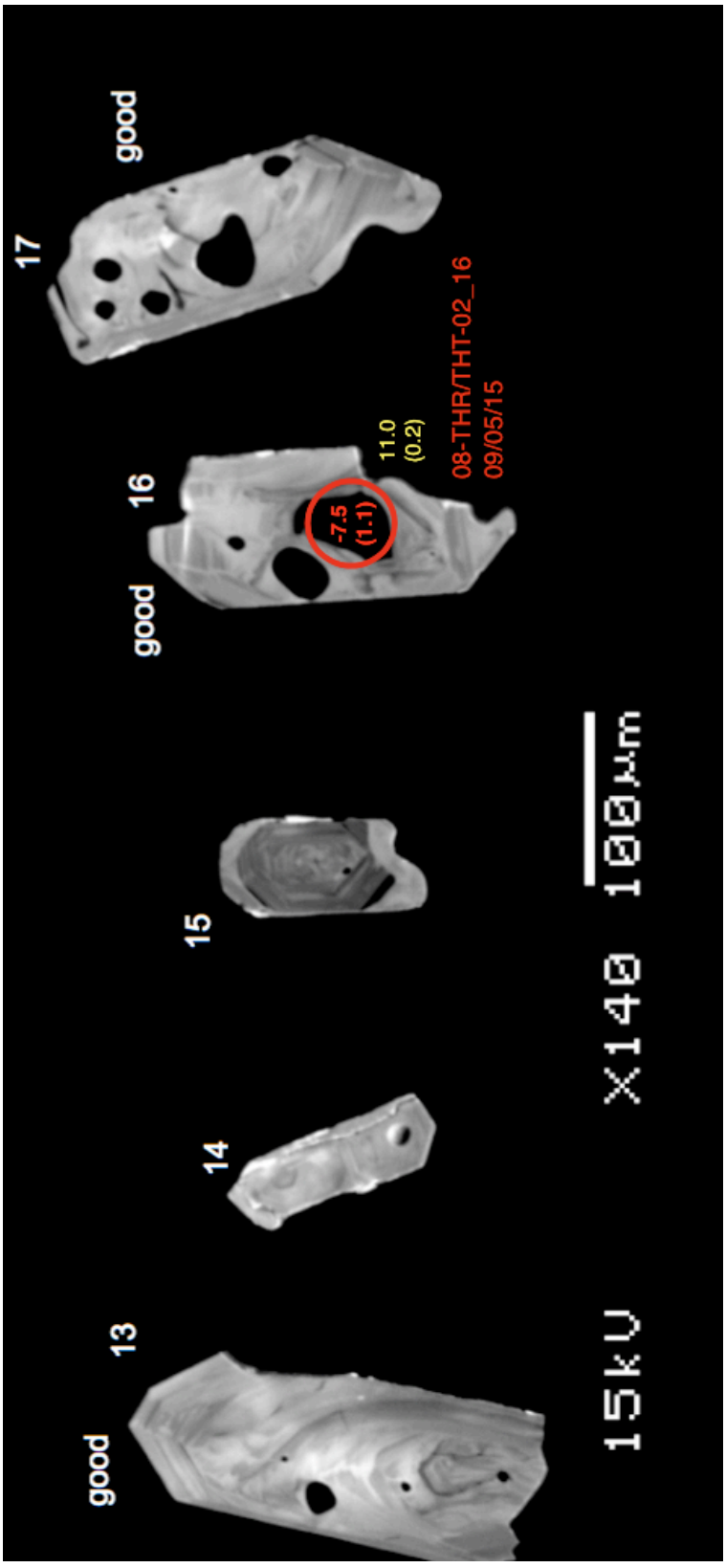

Figure 48. Triguero Homestead rhyolite zircons

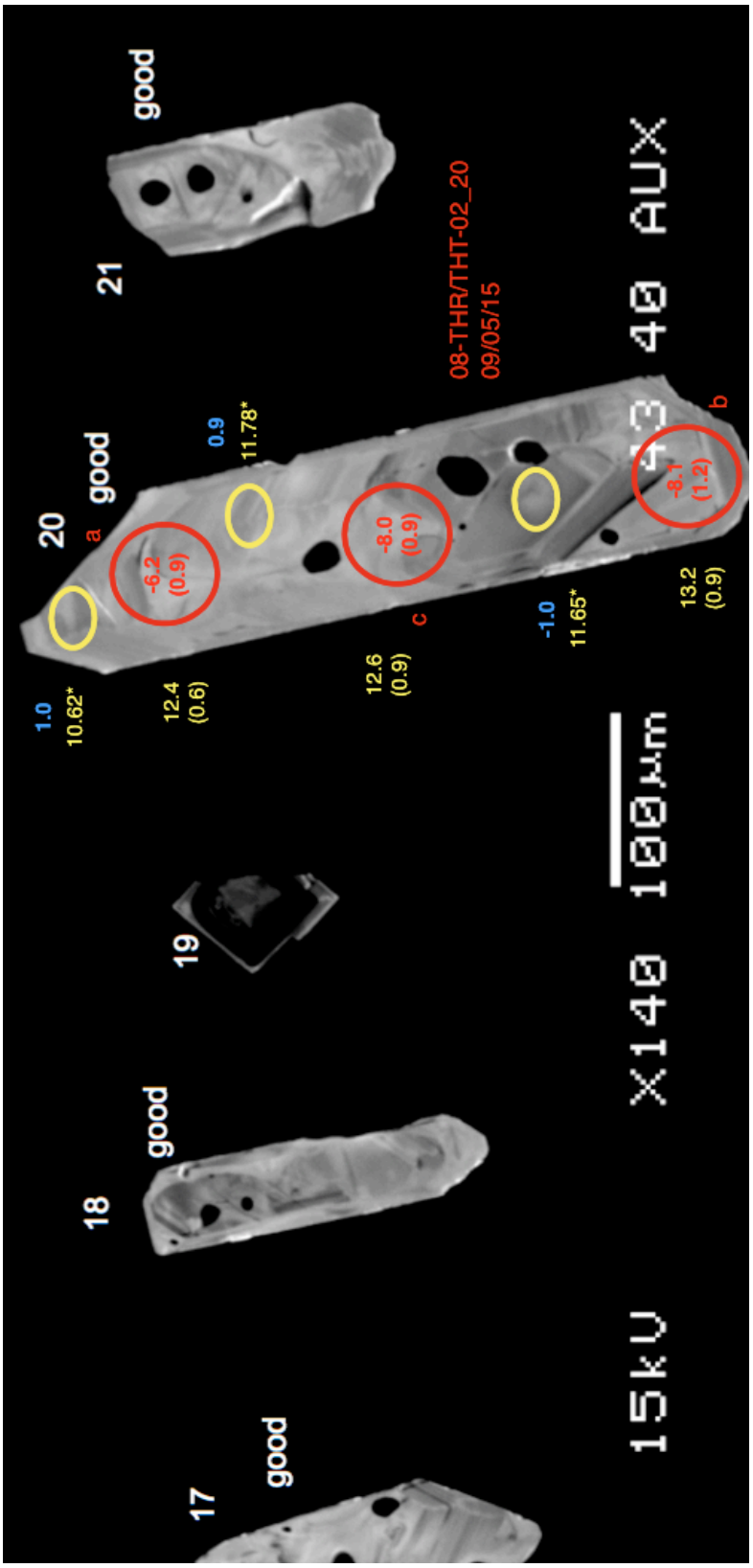

Figure 49. Triguero Homestead rhyolite zircons

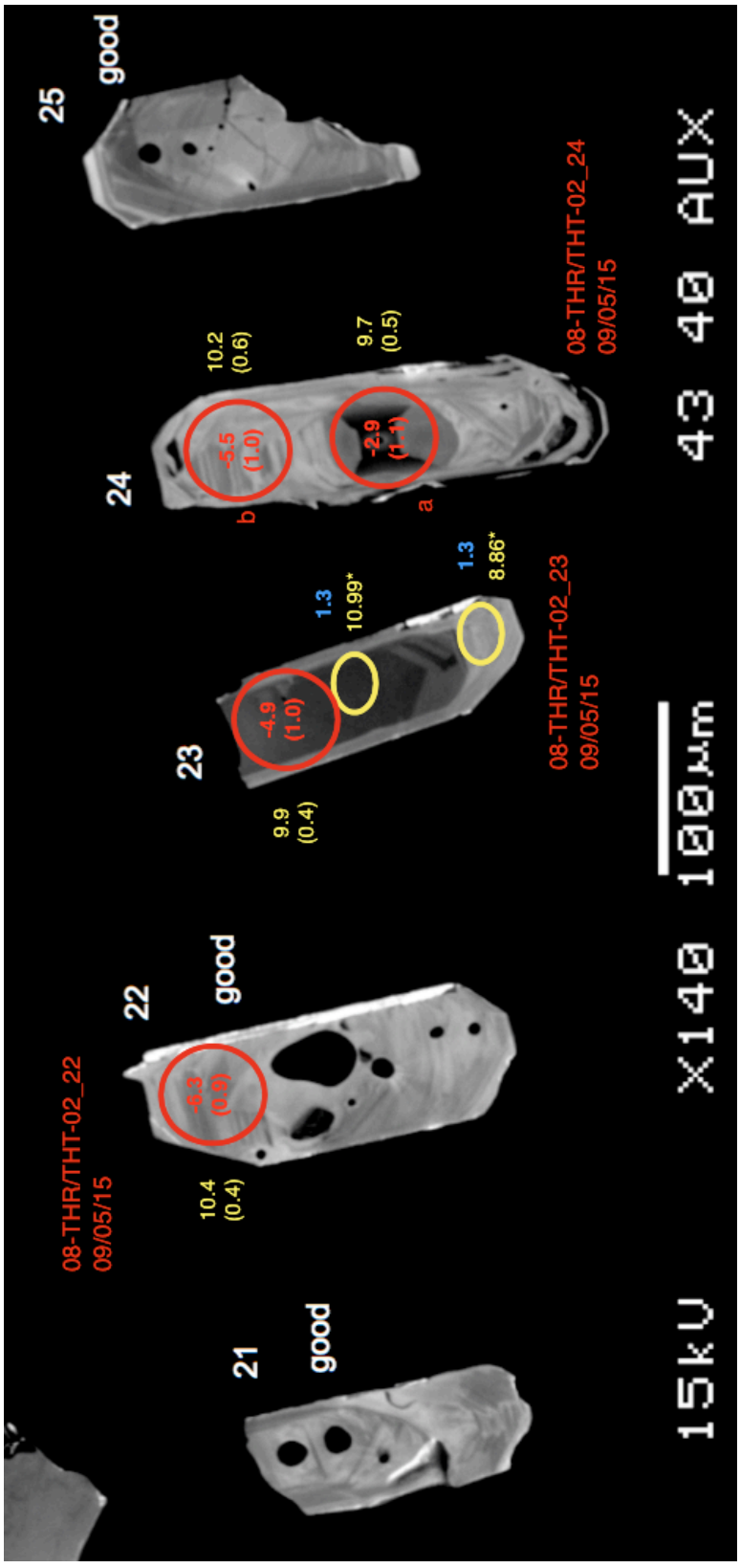

Figure 50. Triguero Homestead rhyolite zircons

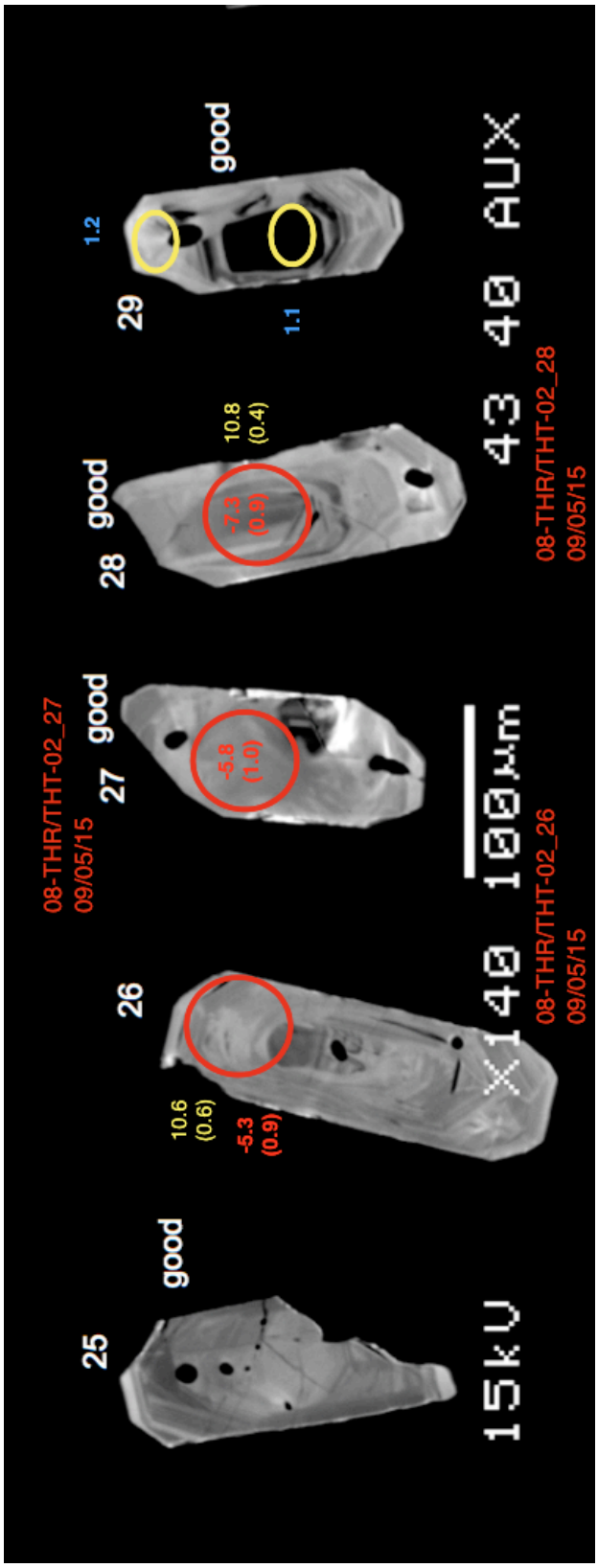

Figure 51. Triguero Homestead rhyolite zircons

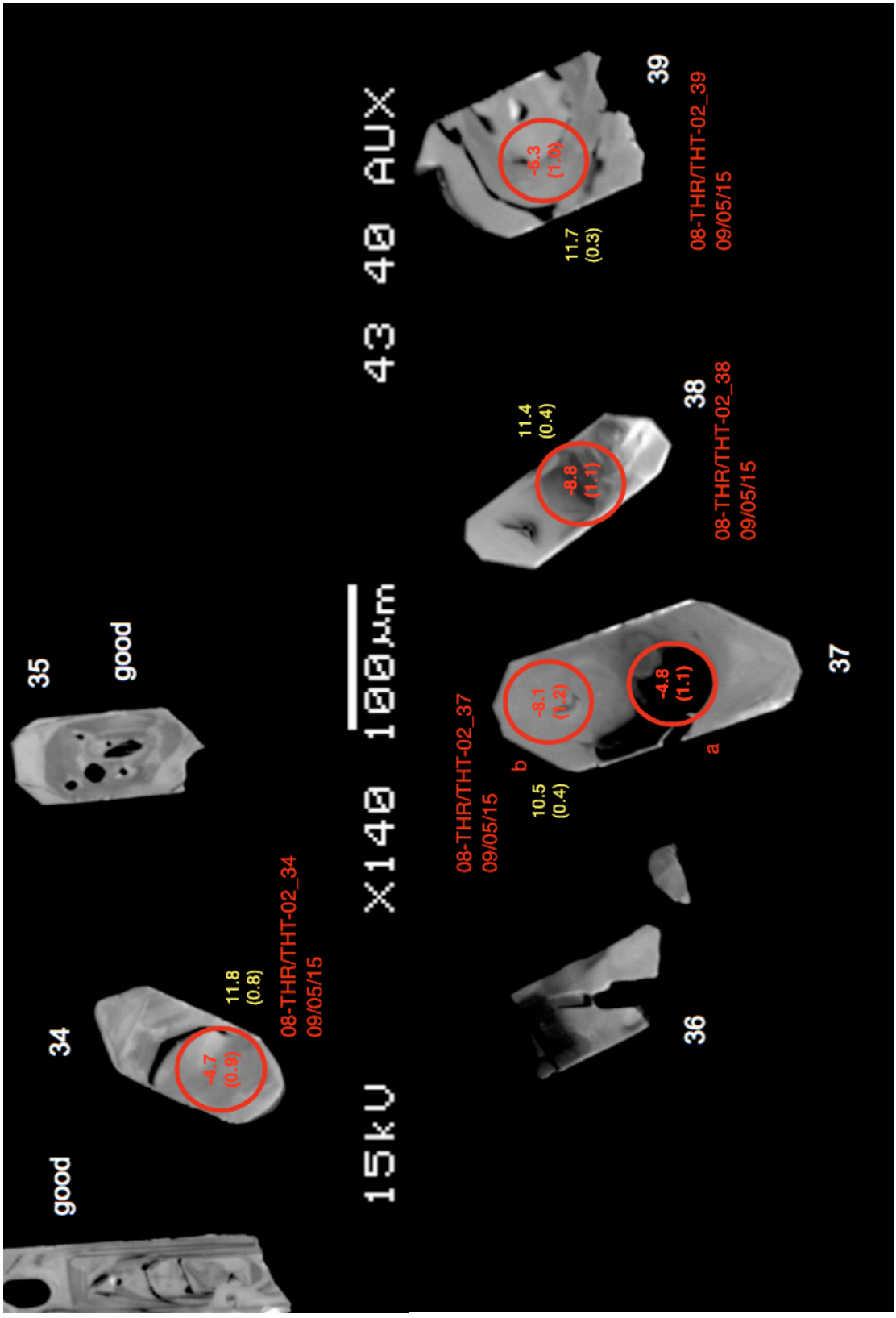

Figure 52. Triguero Homestead rhyolite zircons

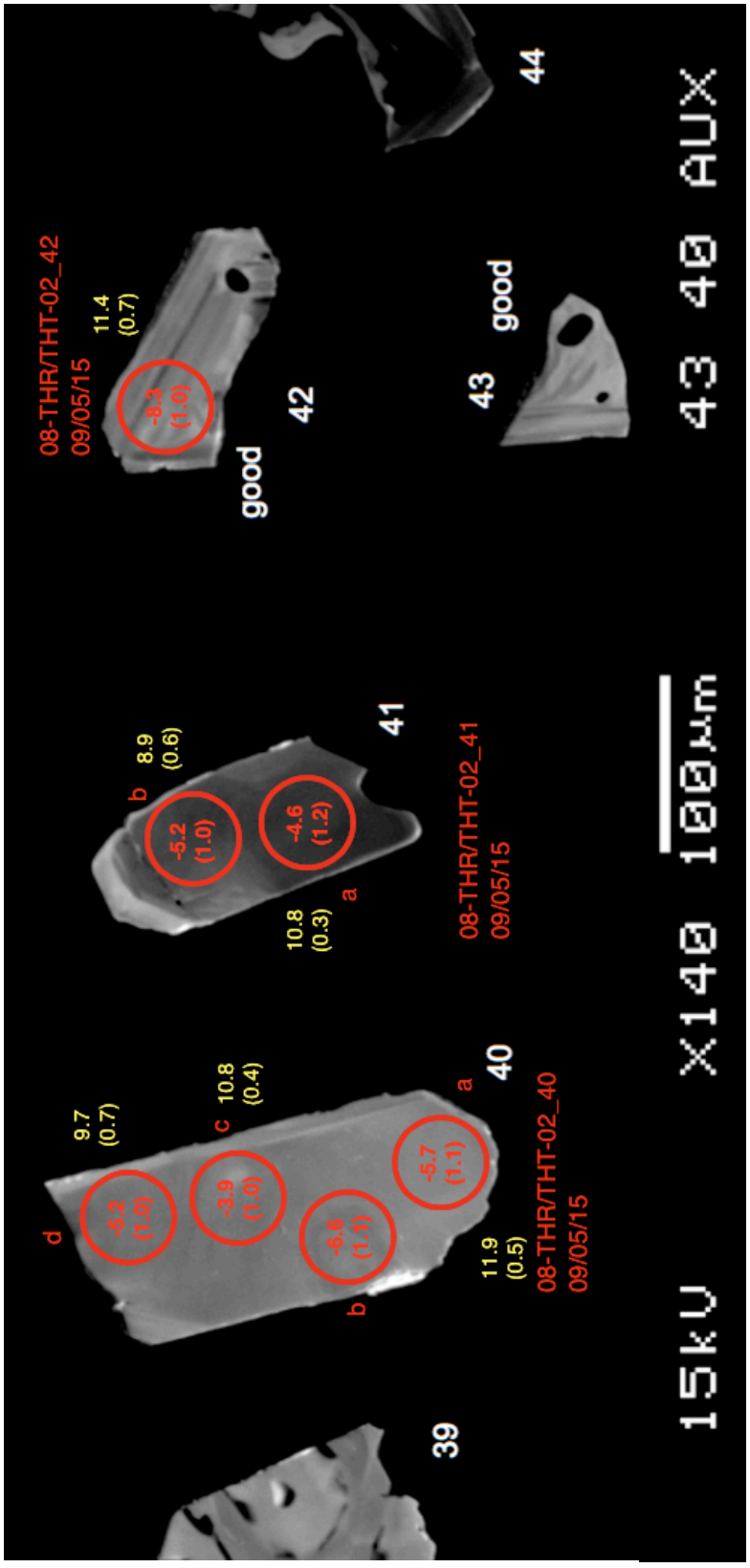

Figure 53. Triguero Homestead rhyolite zircons

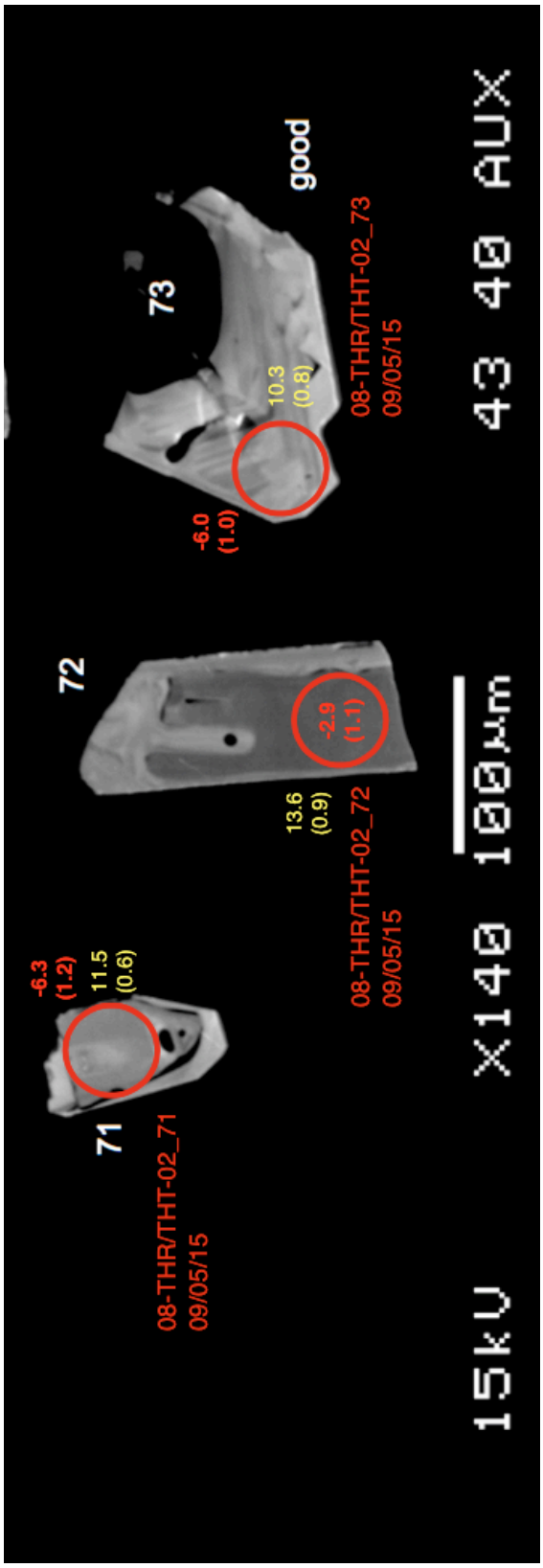

Figure 54. Triguero Homestead rhyolite zircons

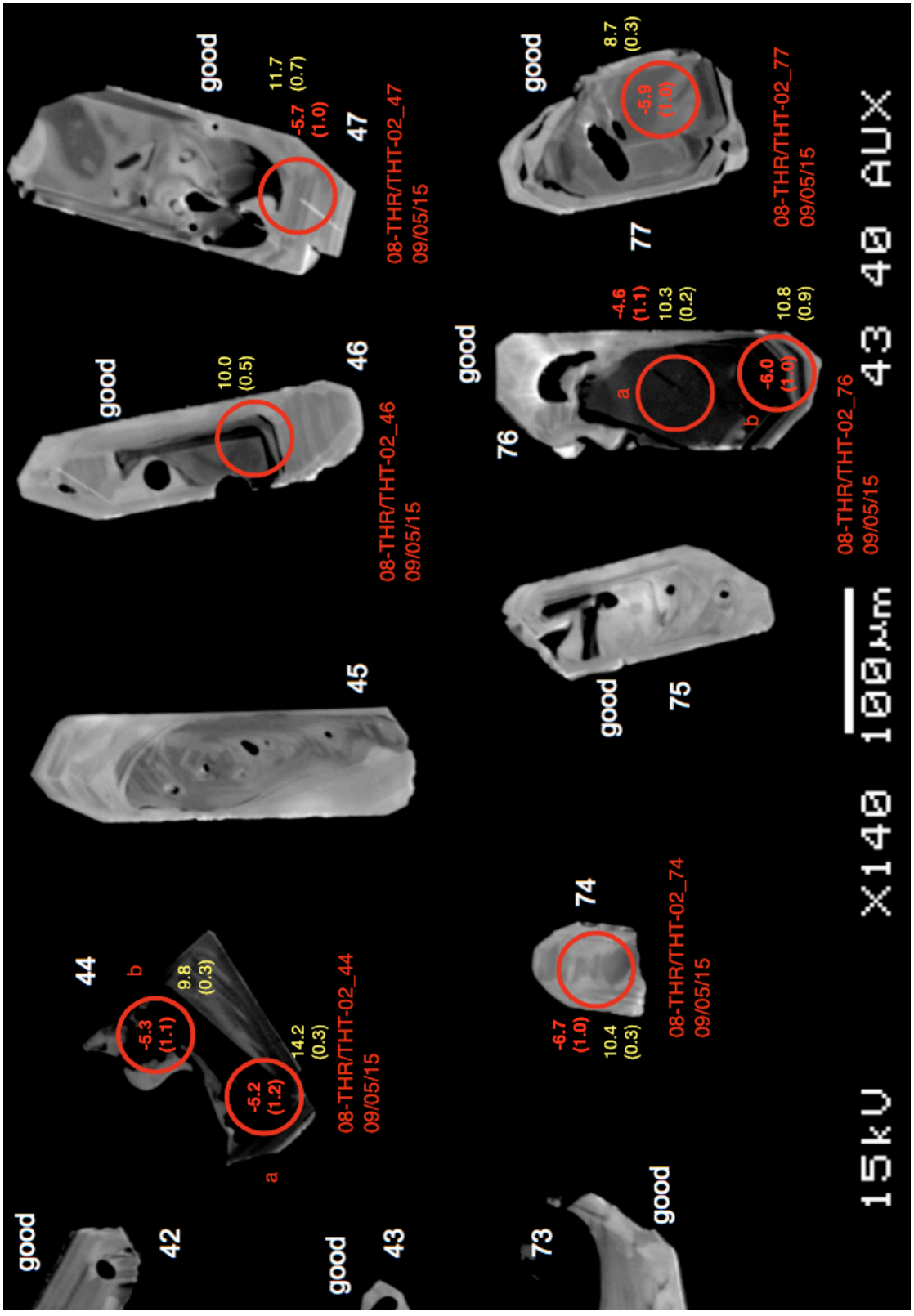

Figure 55. Triguero Homestead rhyolite zircons

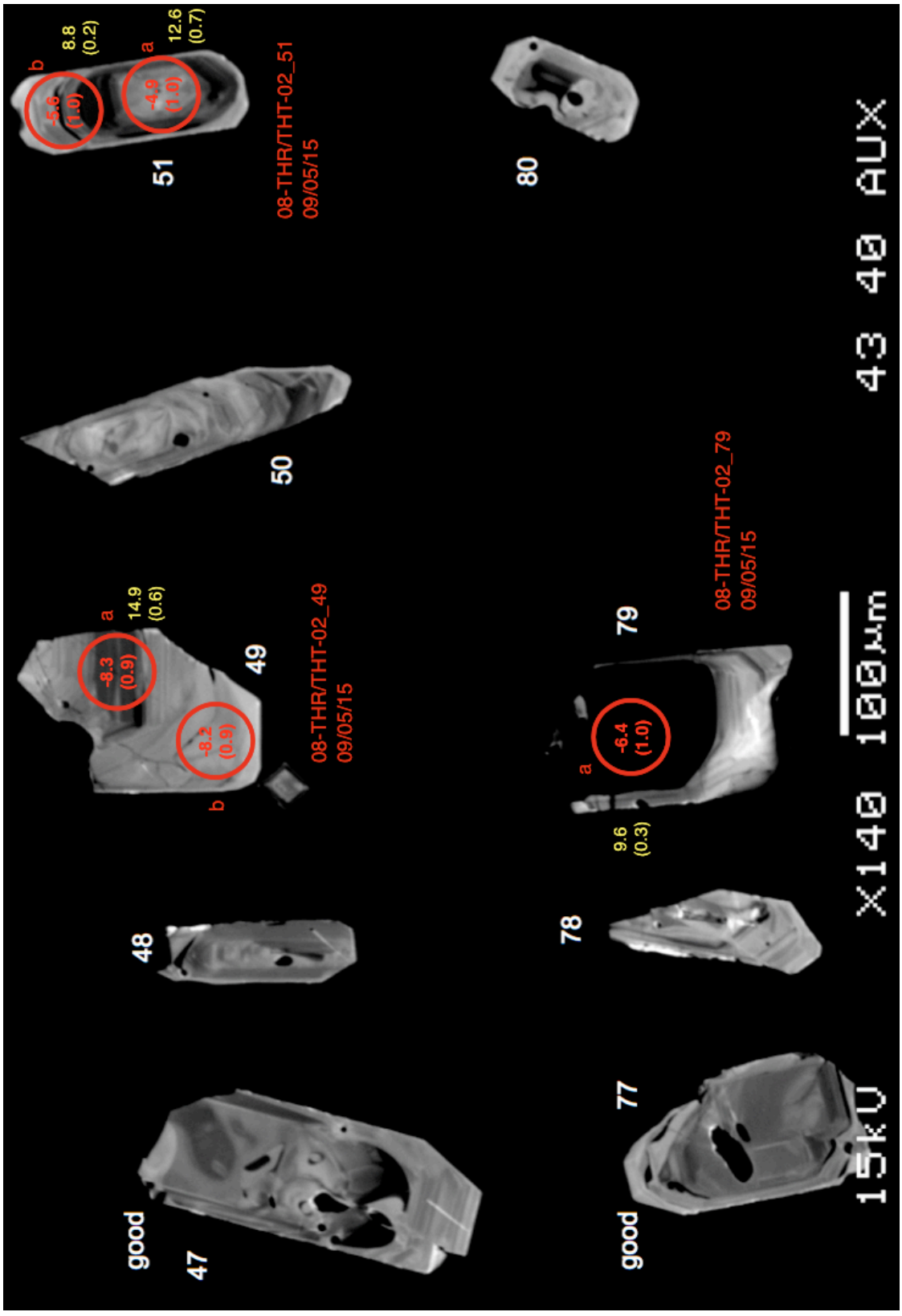

Figure 56. Triguero Homestead rhyolite zircons

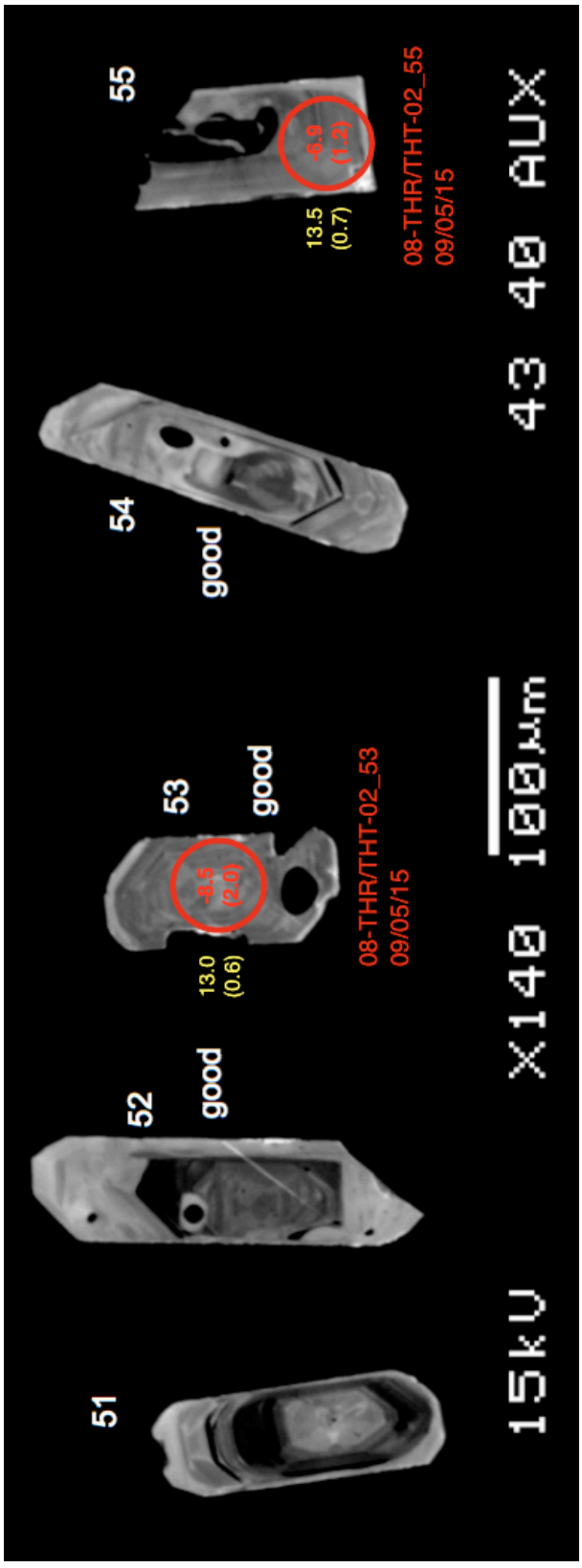

Figure 57. Triguero Homestead rhyolite zircons

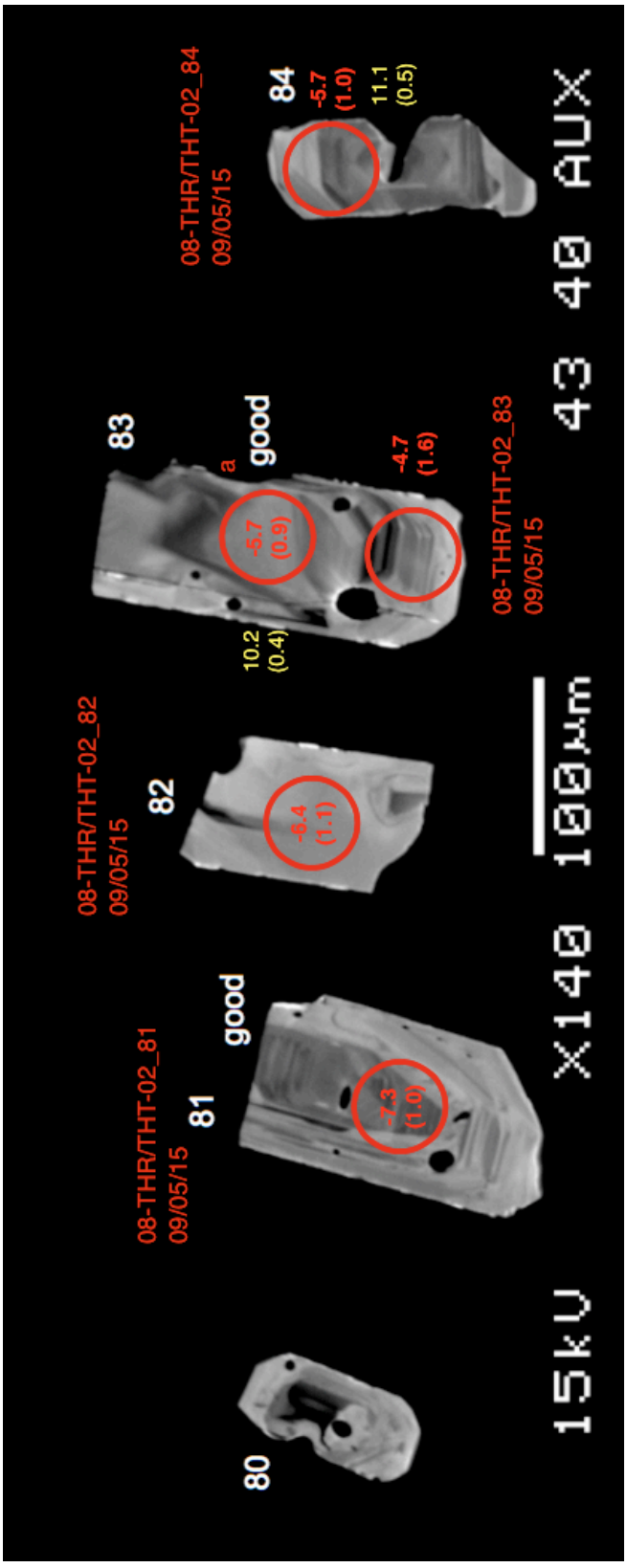

Figure 58. Triguero Homestead rhyolite zircons

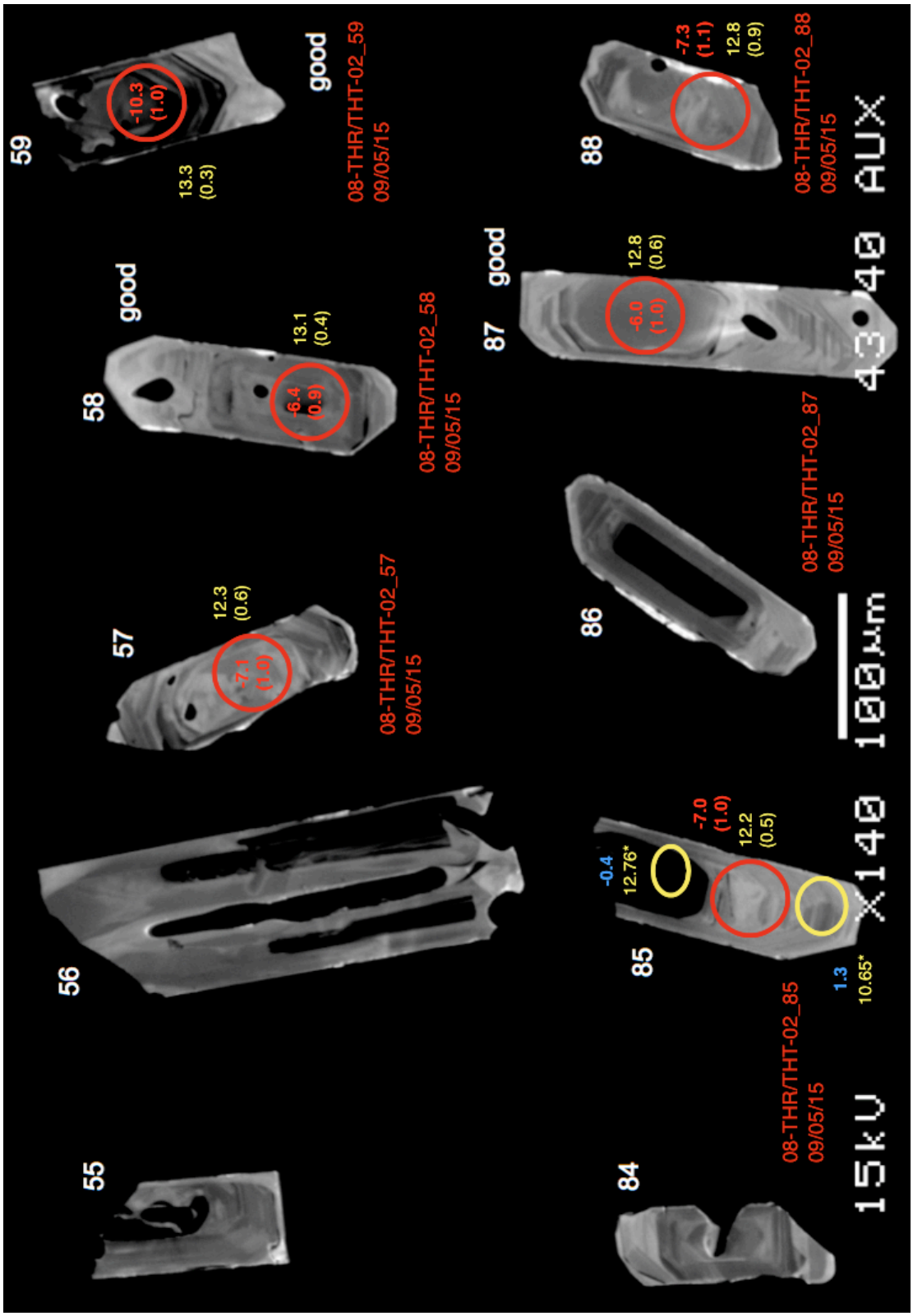

Figure 59. Triguero Homestead rhyolite zircons

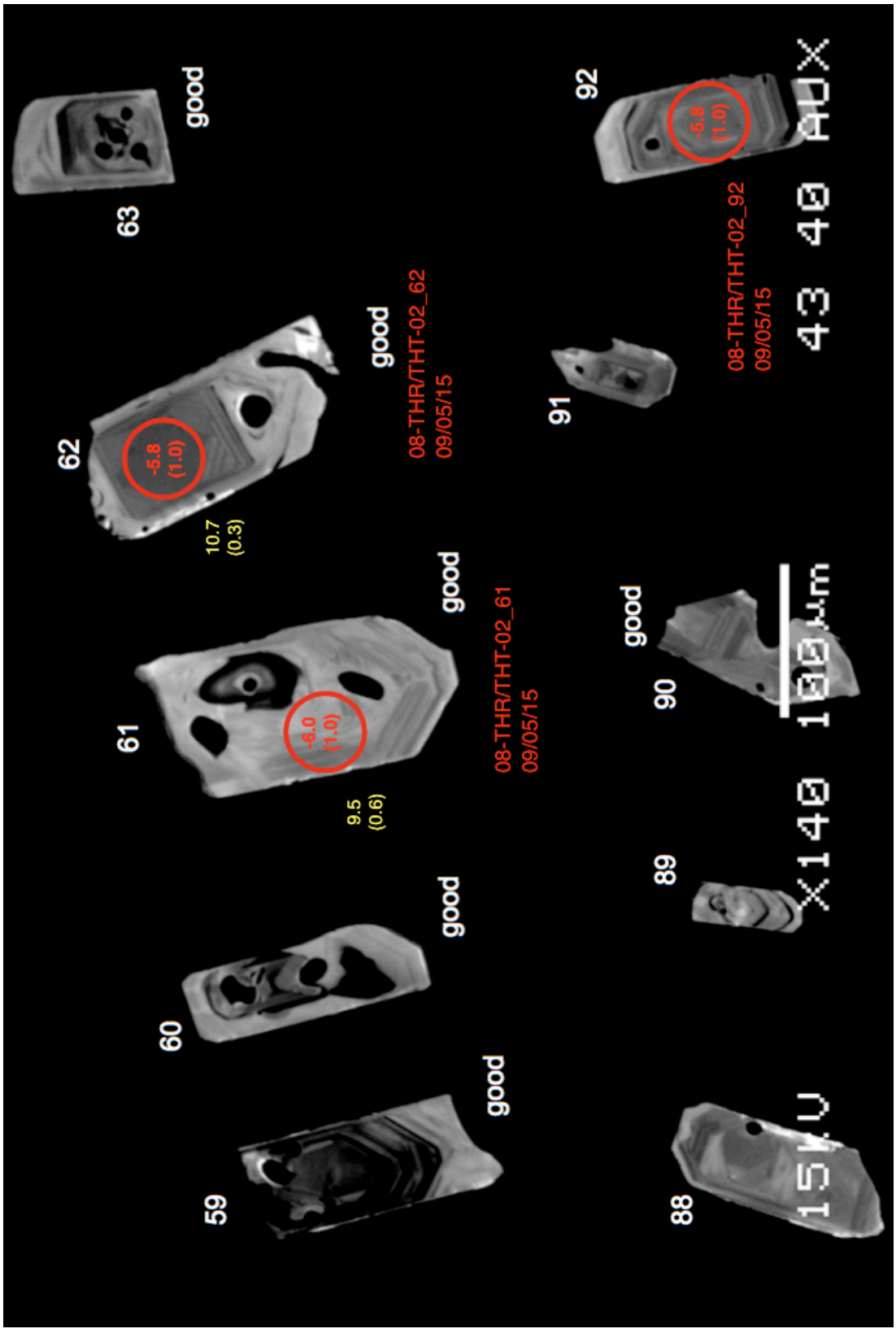

Figure 60. Triguero Homestead rhyolite zircons

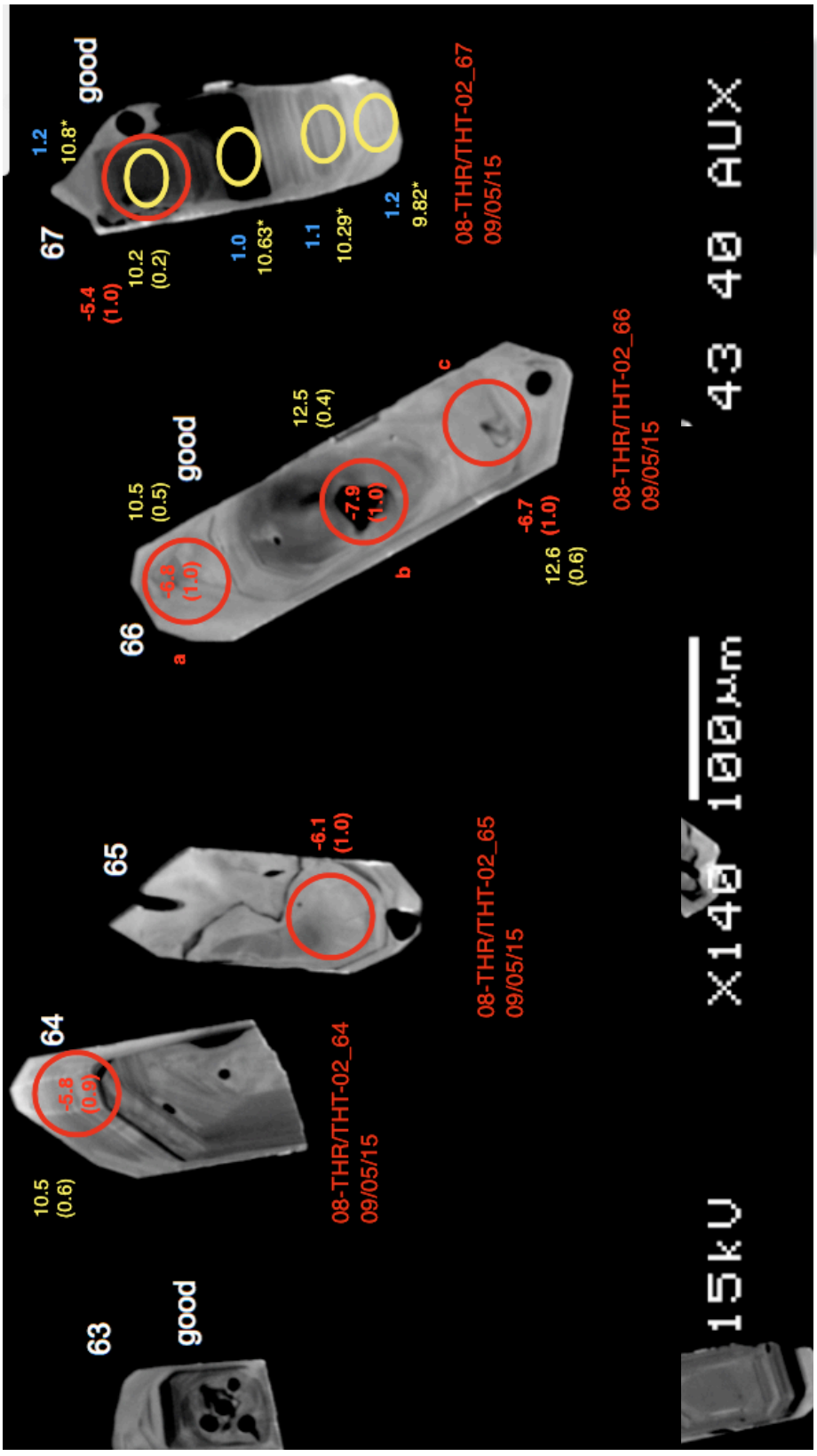

Figure 61. Triguero Homestead rhyolite zircons

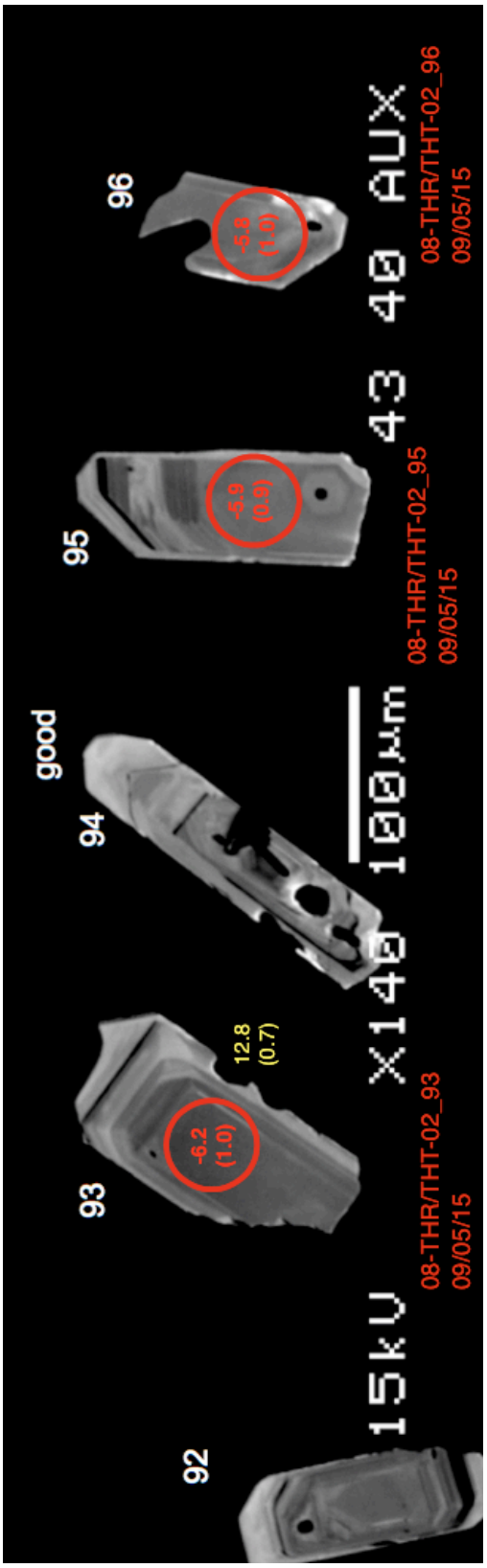

Figure 62. Triguero Homestead rhyolite zircons

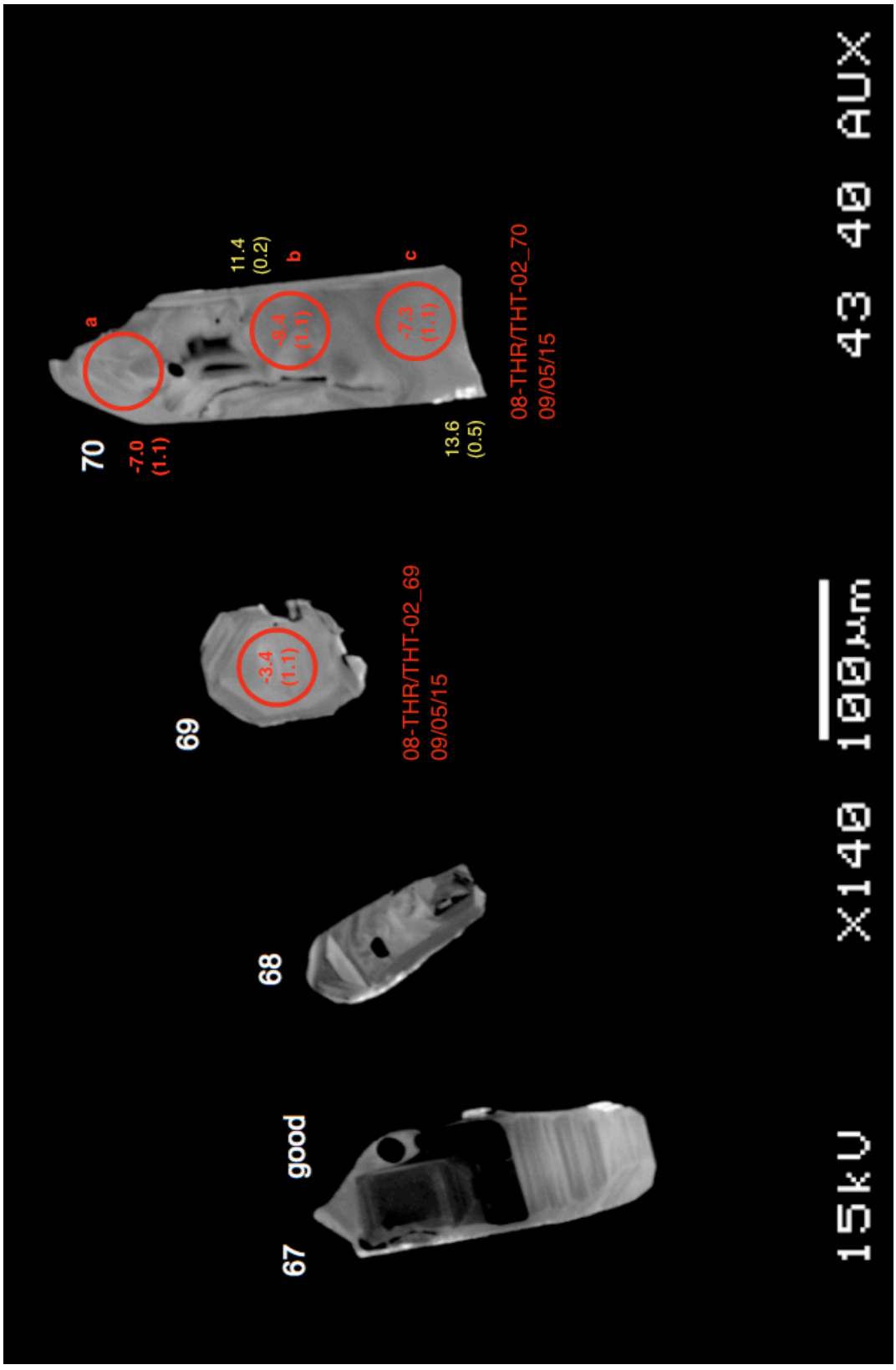

Figure 63. Triguero Homestead rhyolite zircons

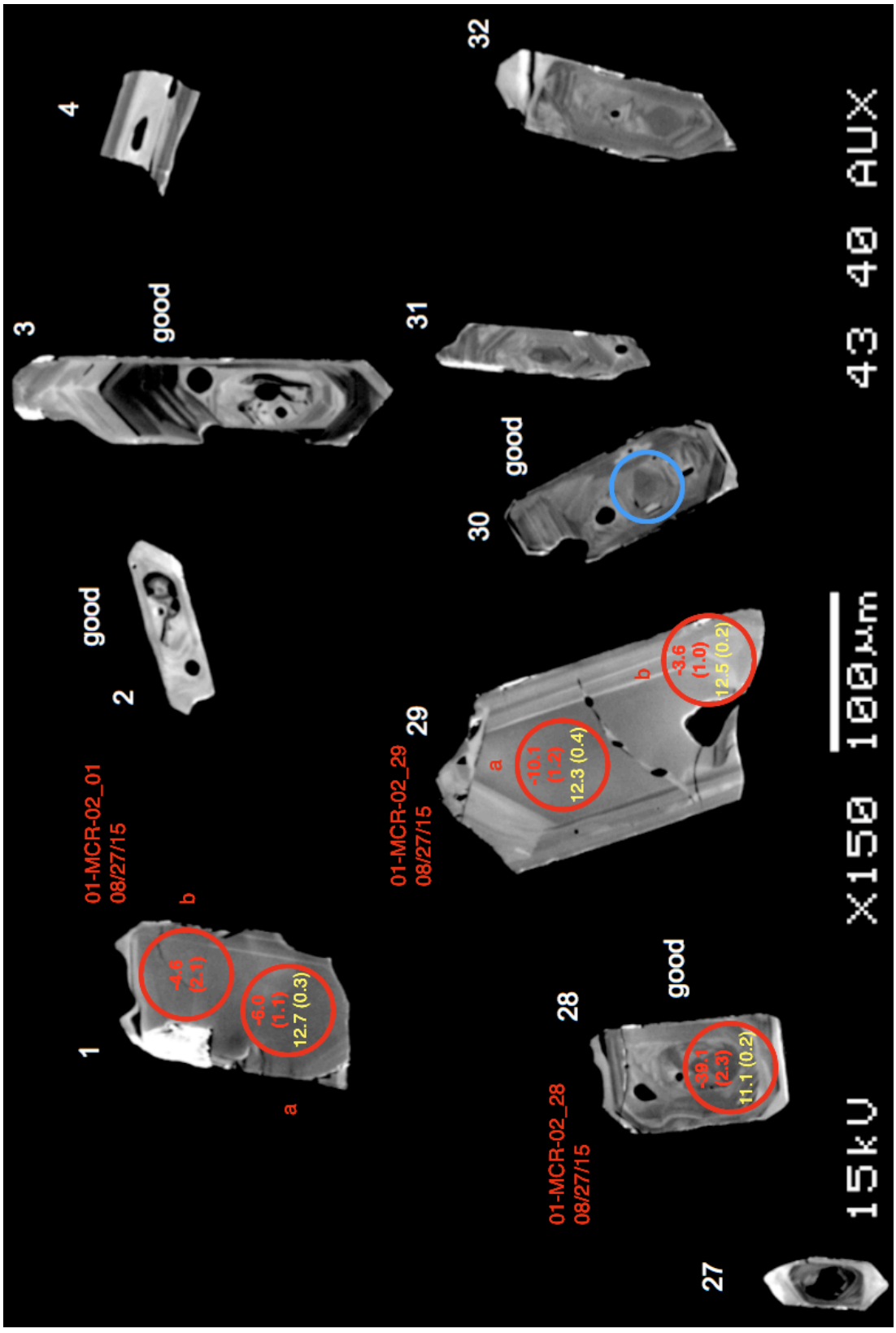

Figure 64. Marys Creek rhyolite zircons

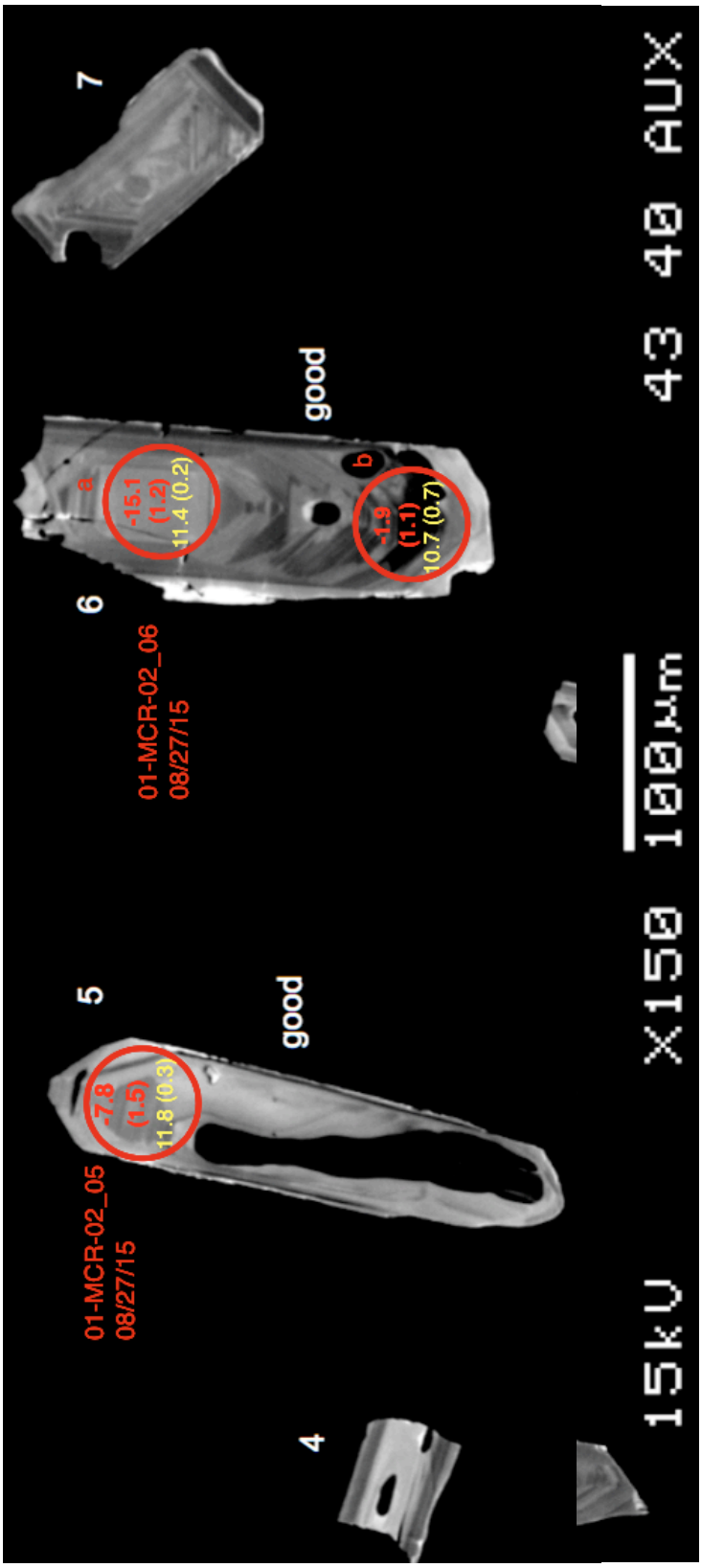

Figure 65. Marys Creek rhyolite zircons

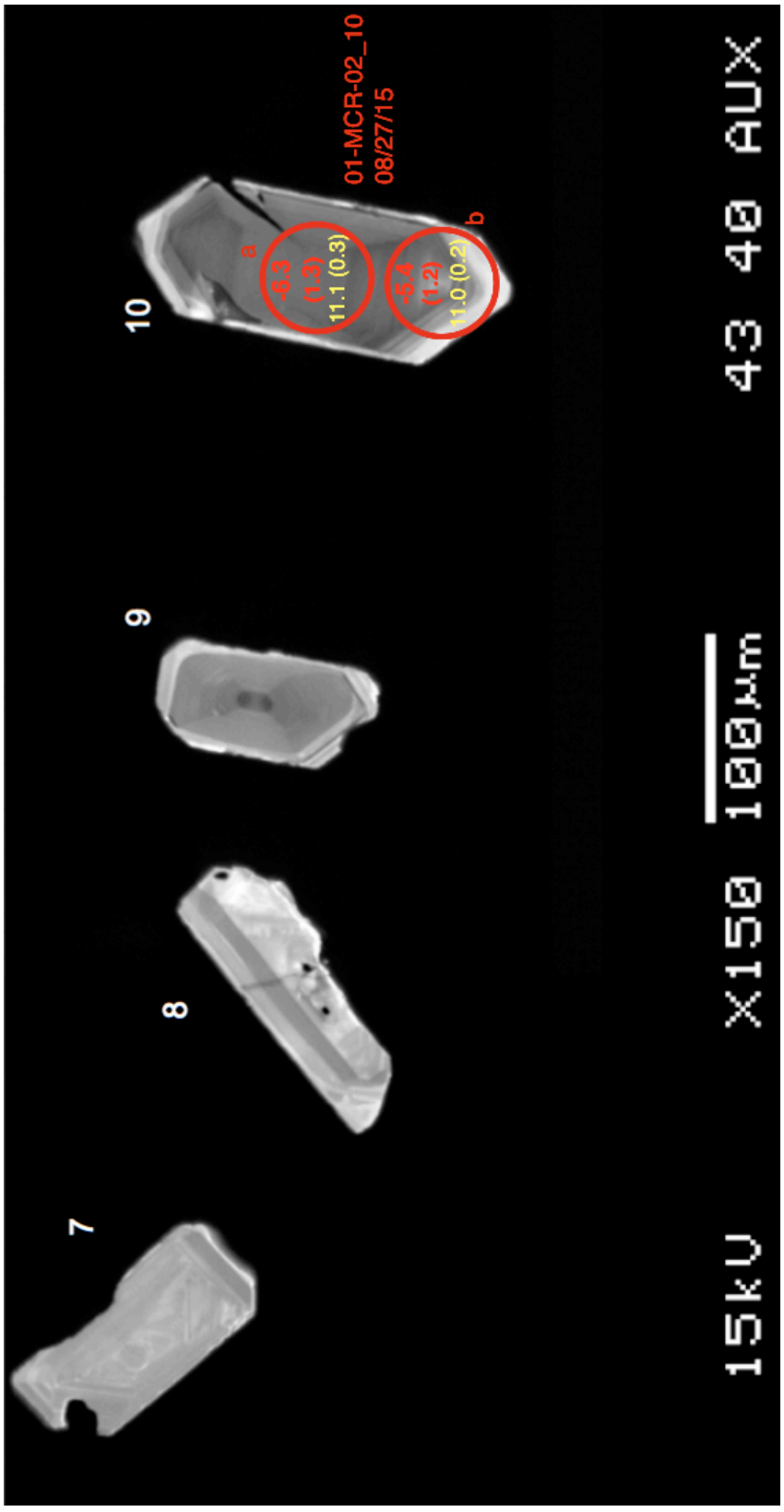

Figure 66. Marys Creek rhyolite zircons

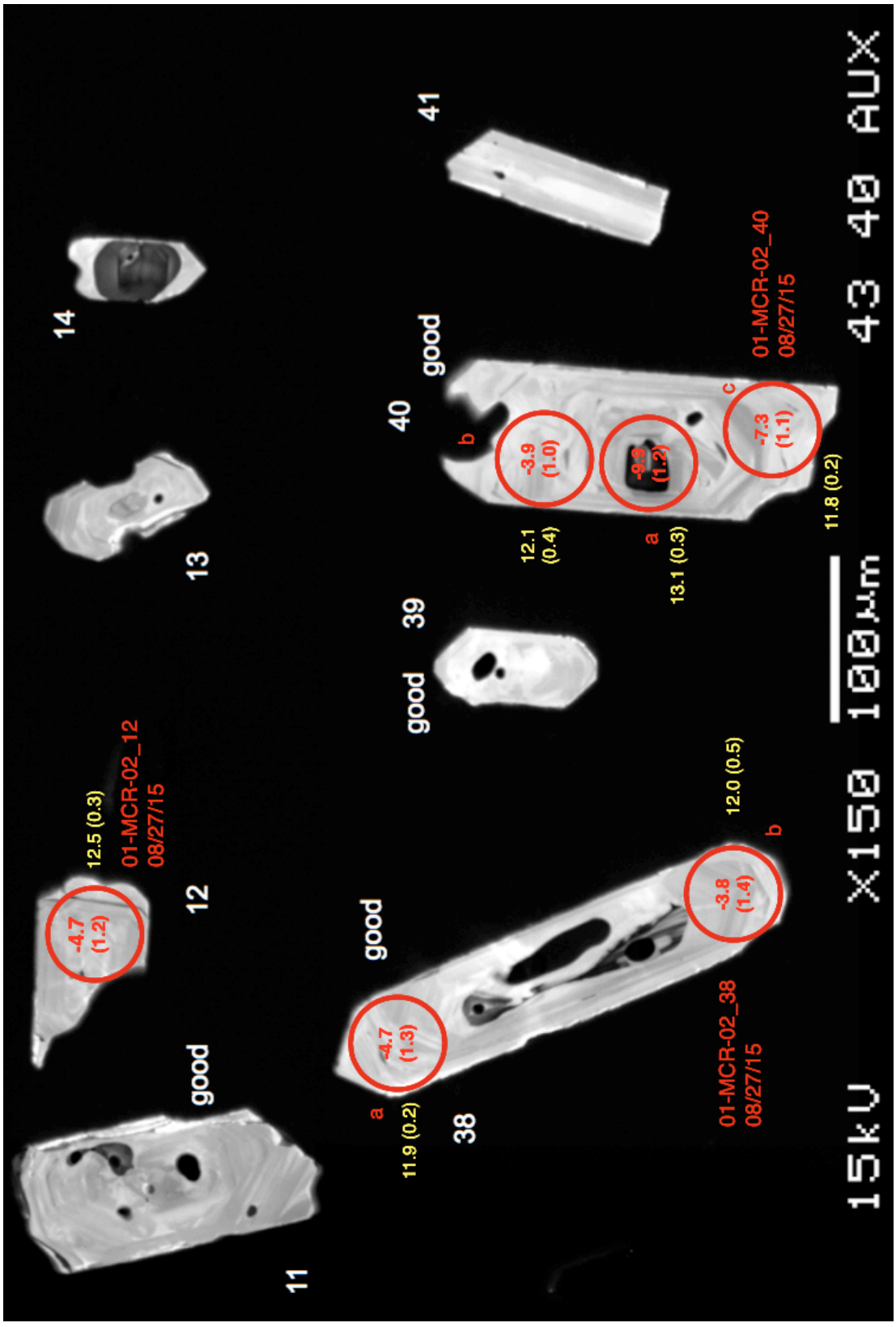

Figure 67. Marys Creek rhyolite zircons

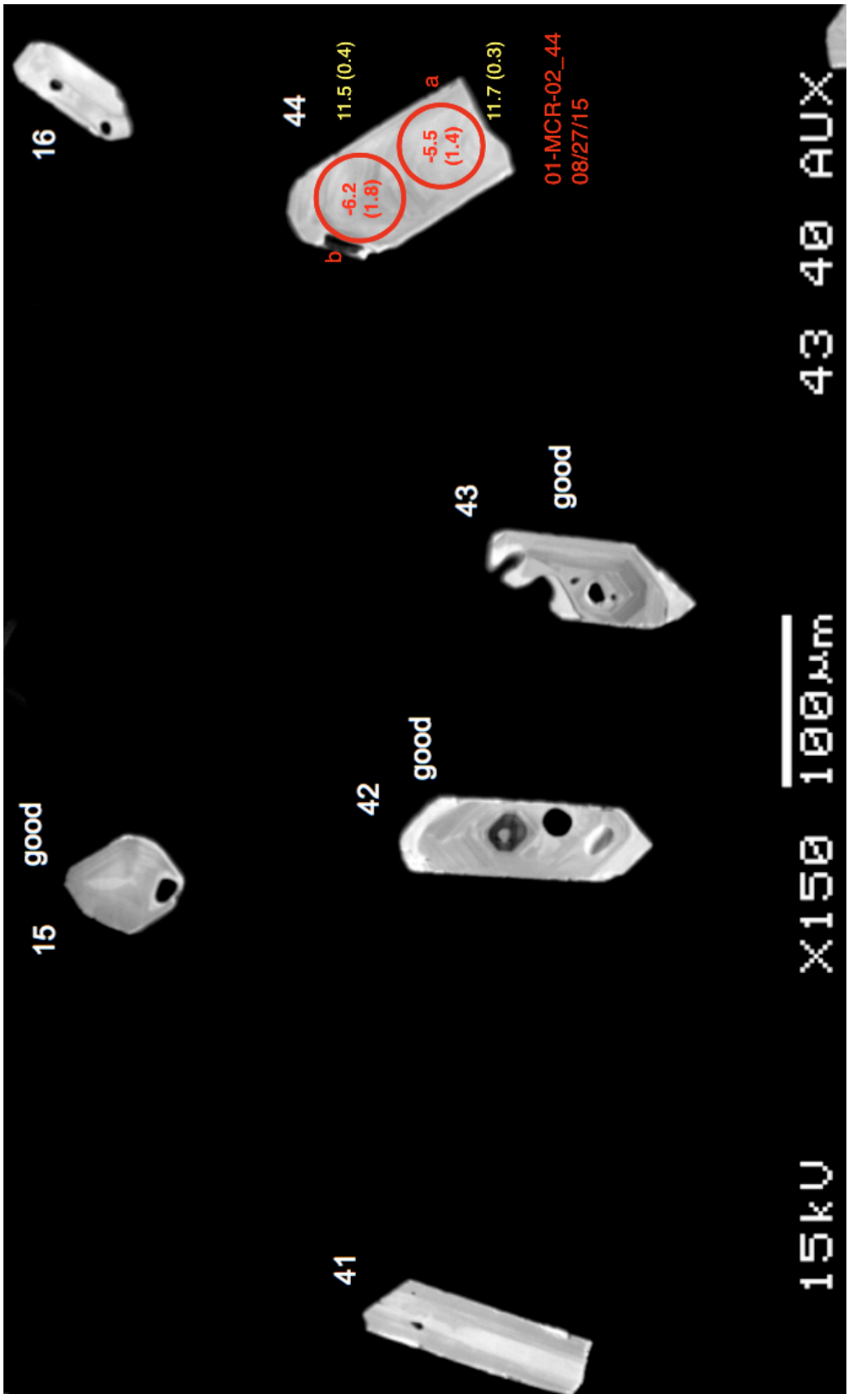

Figure 68. Marys Creek rhyolite zircons

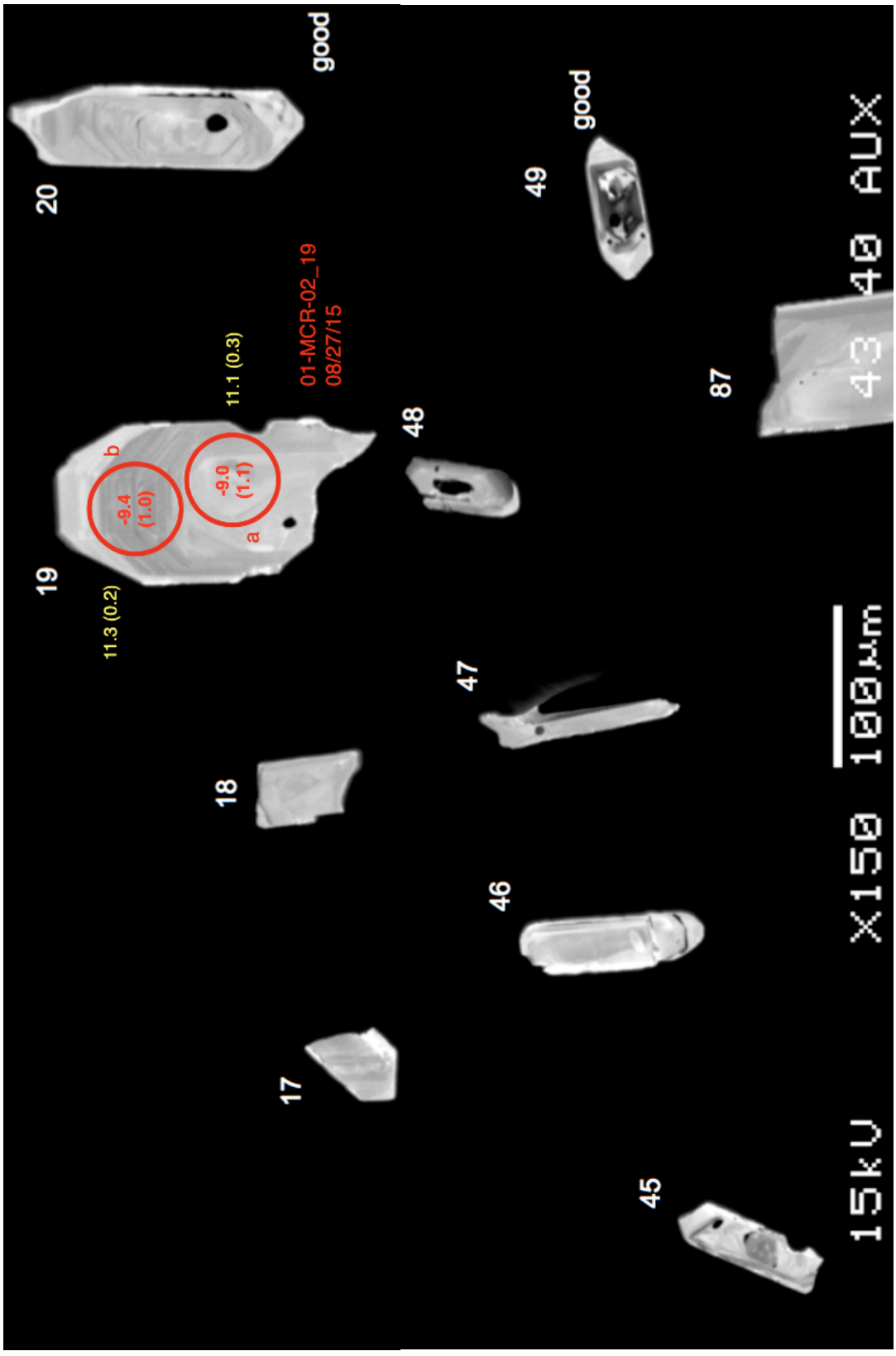

Figure 69. Marys Creek rhyolite zircons

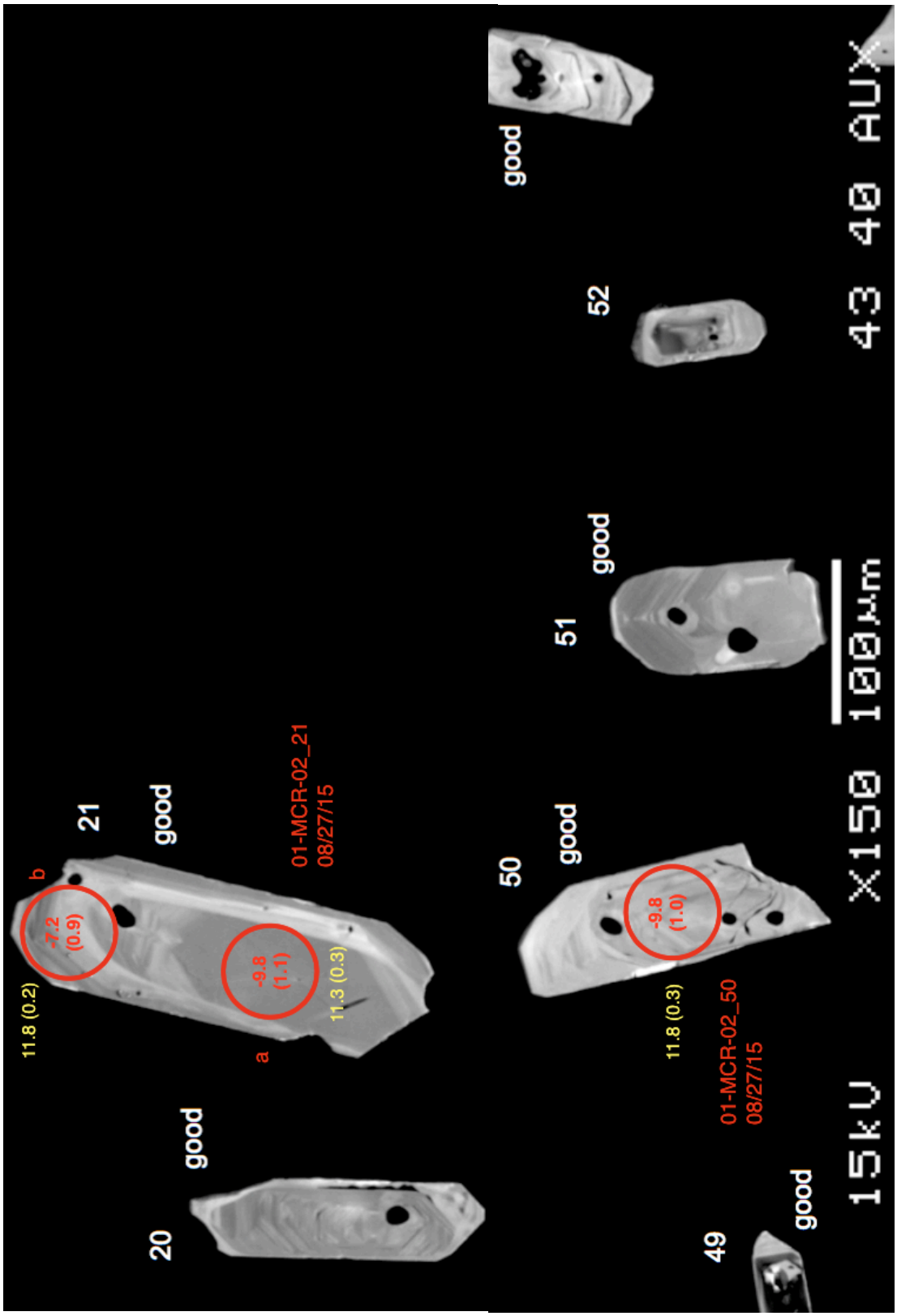

Figure 70. Marys Creek rhyolite zircons

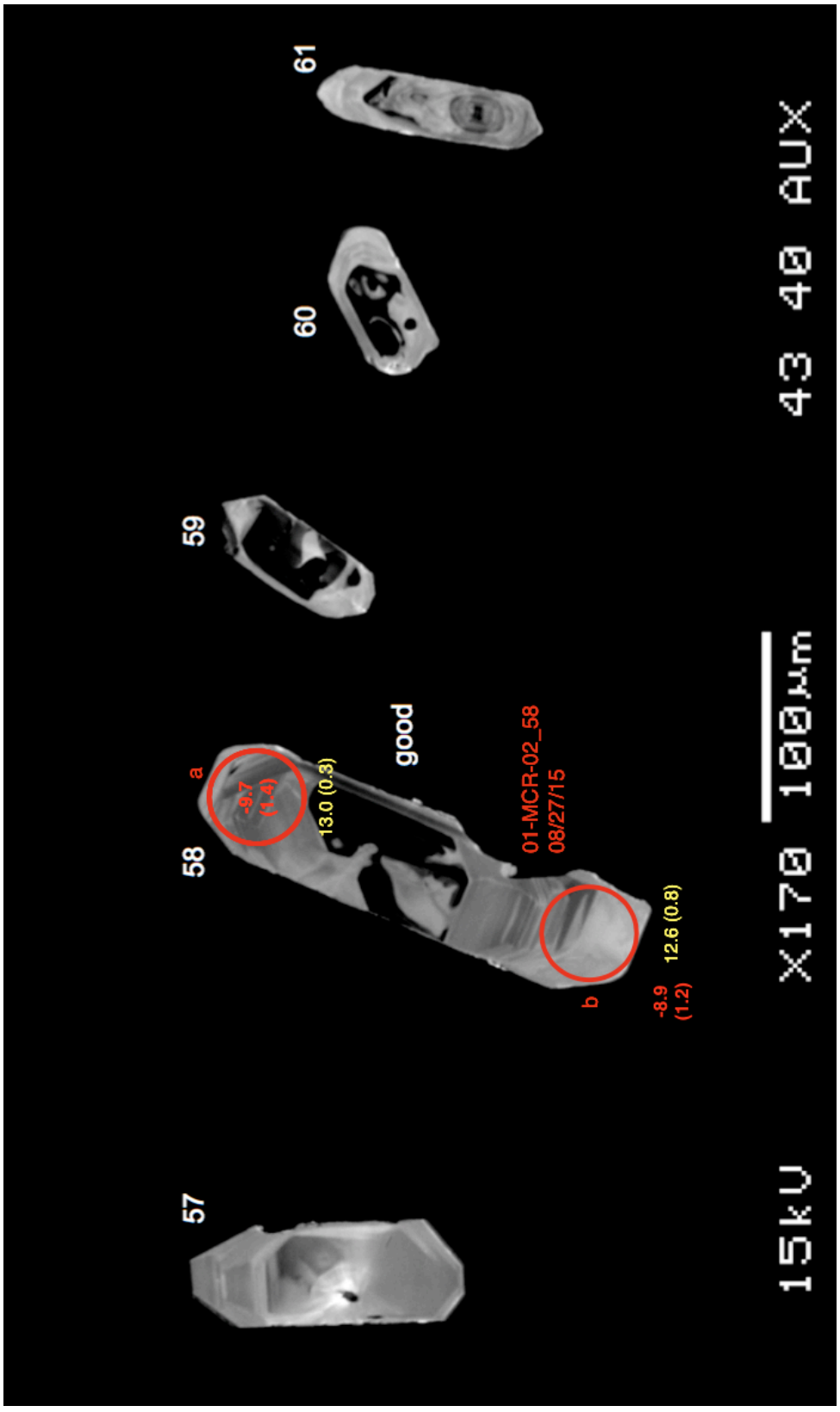

Figure 71. Marys Creek rhyolite zircons

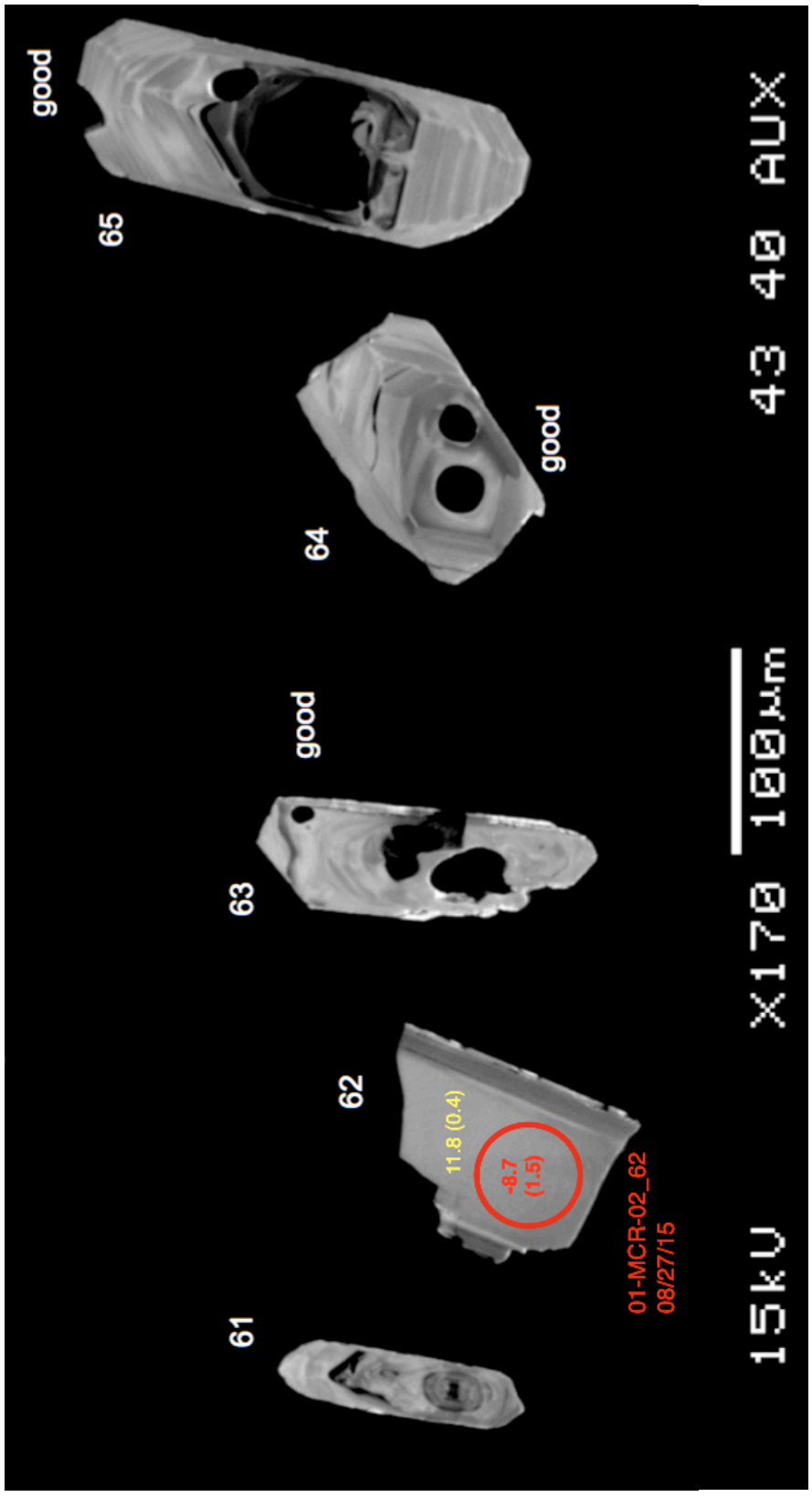

Figure 72. Marys Creek rhyolite

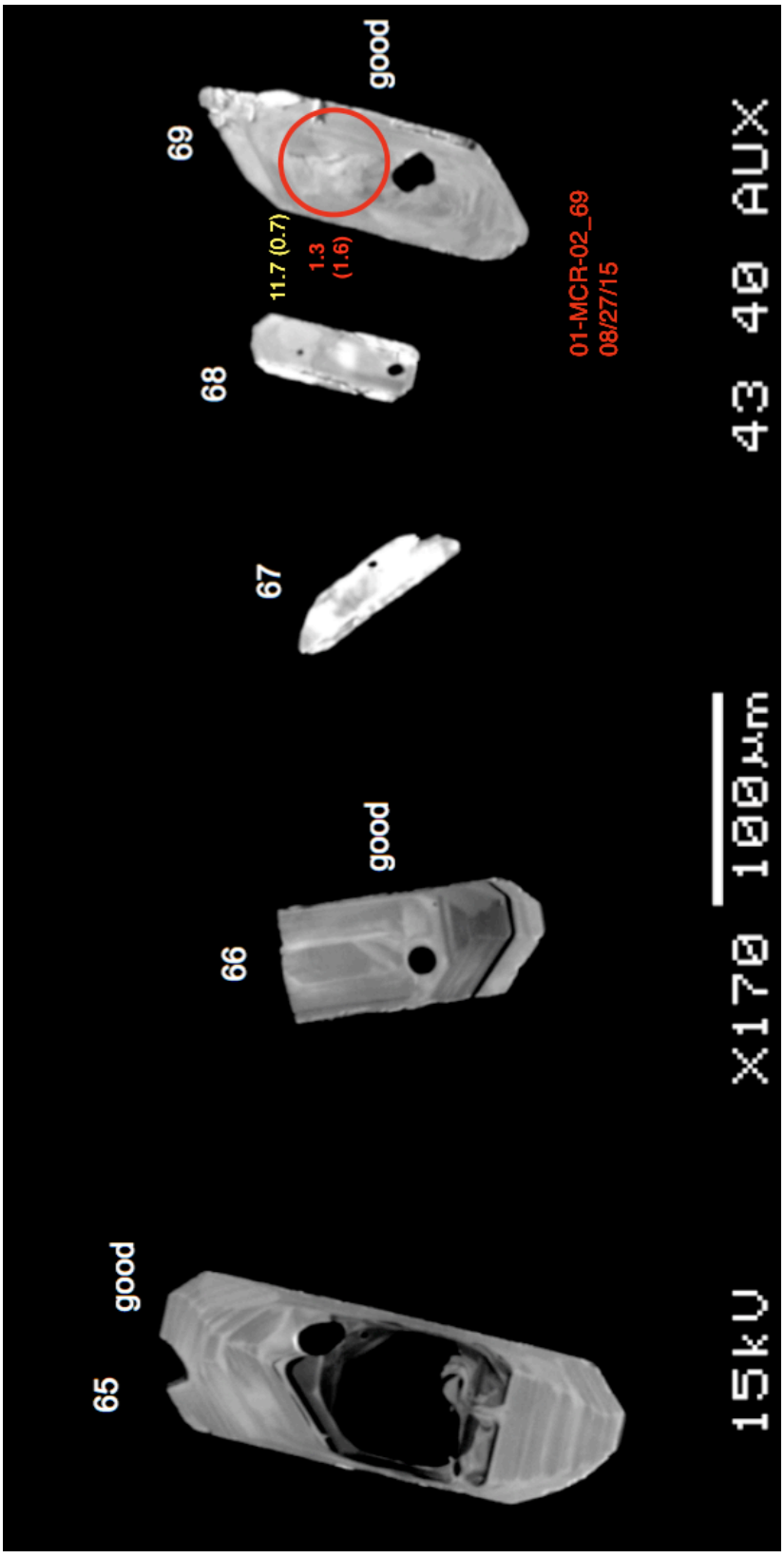

Figure 73. Marys Creek rhyolite

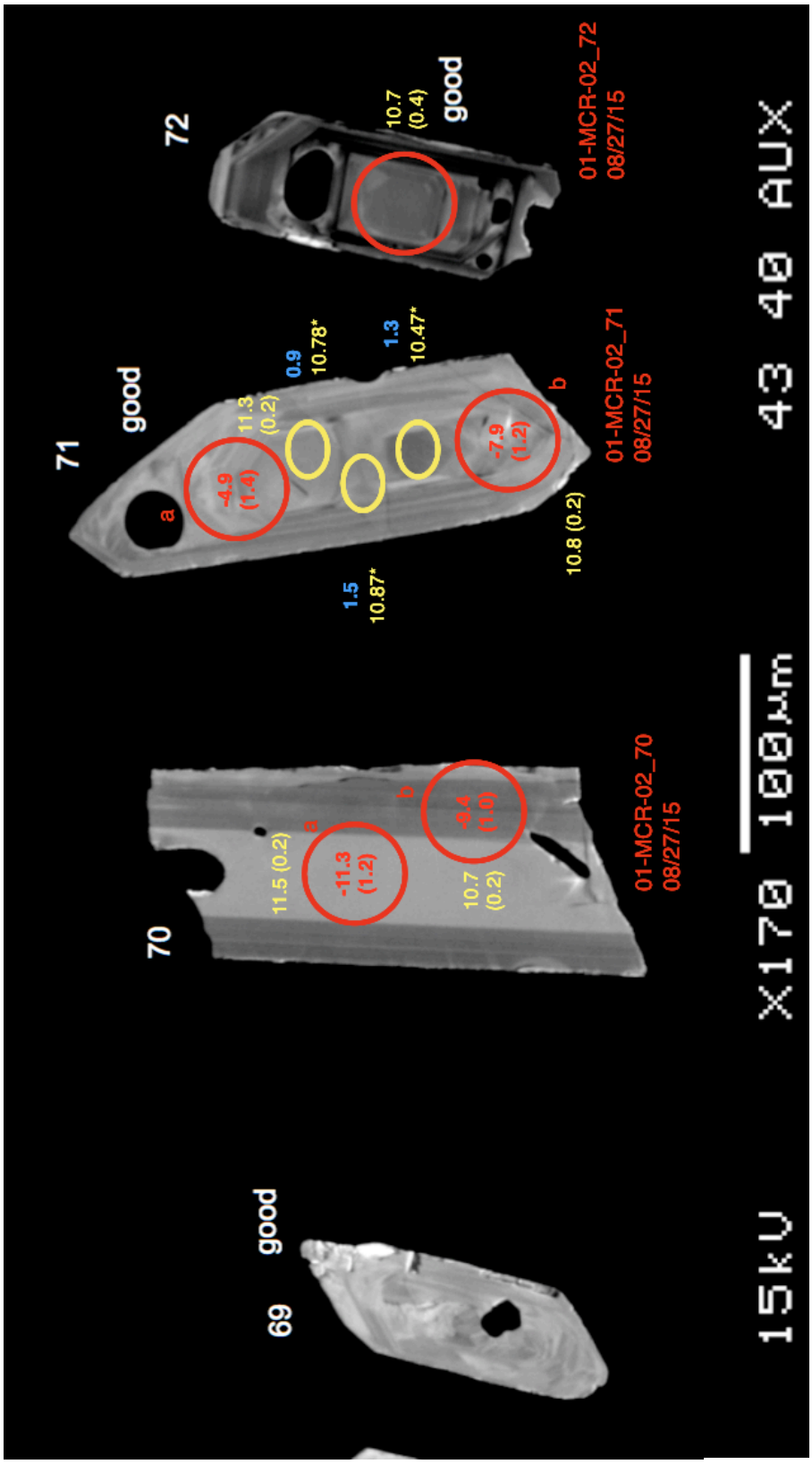

Figure 74. Marys Creek rhyolite

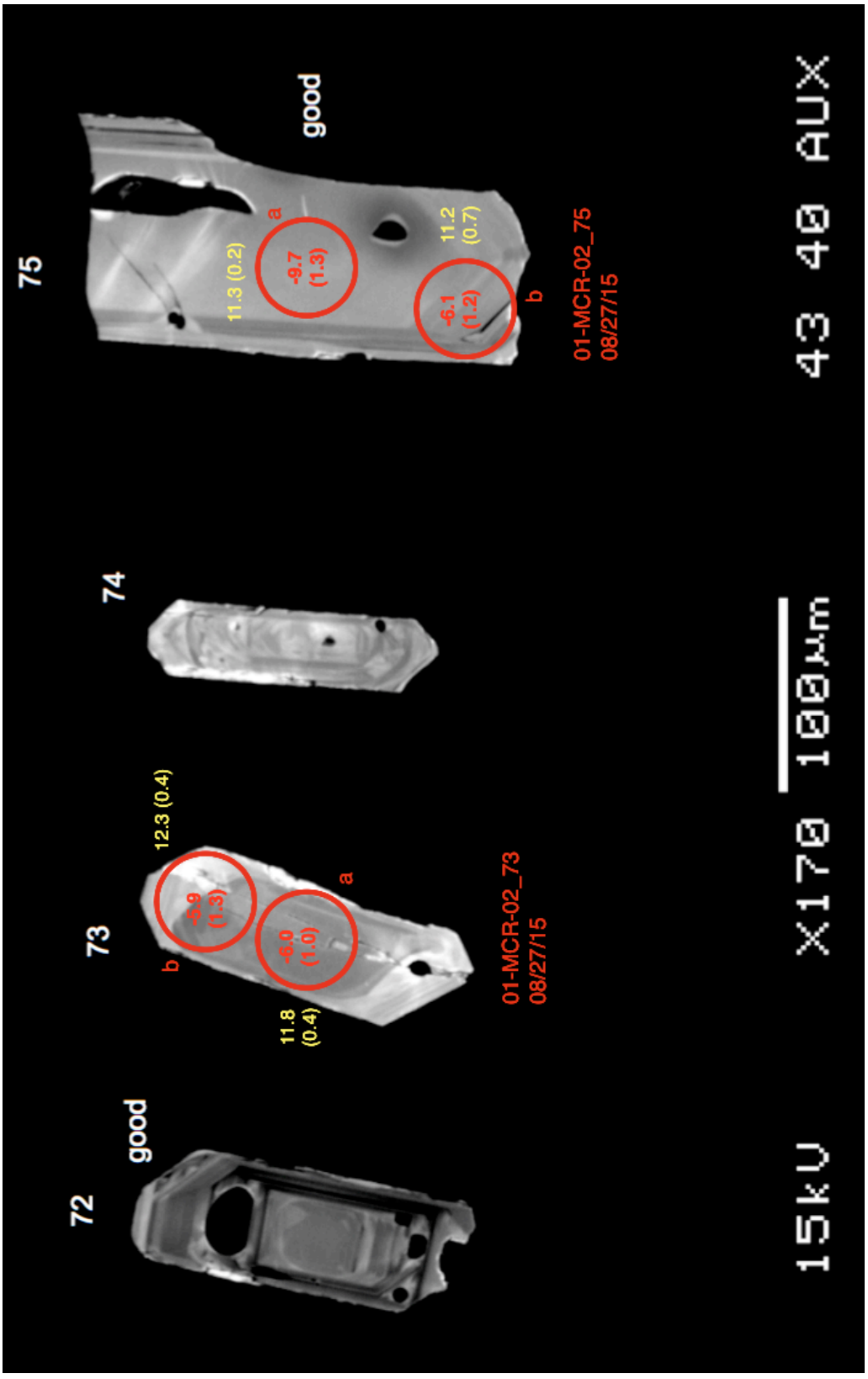

Figure 75. Marys Creek rhyolite

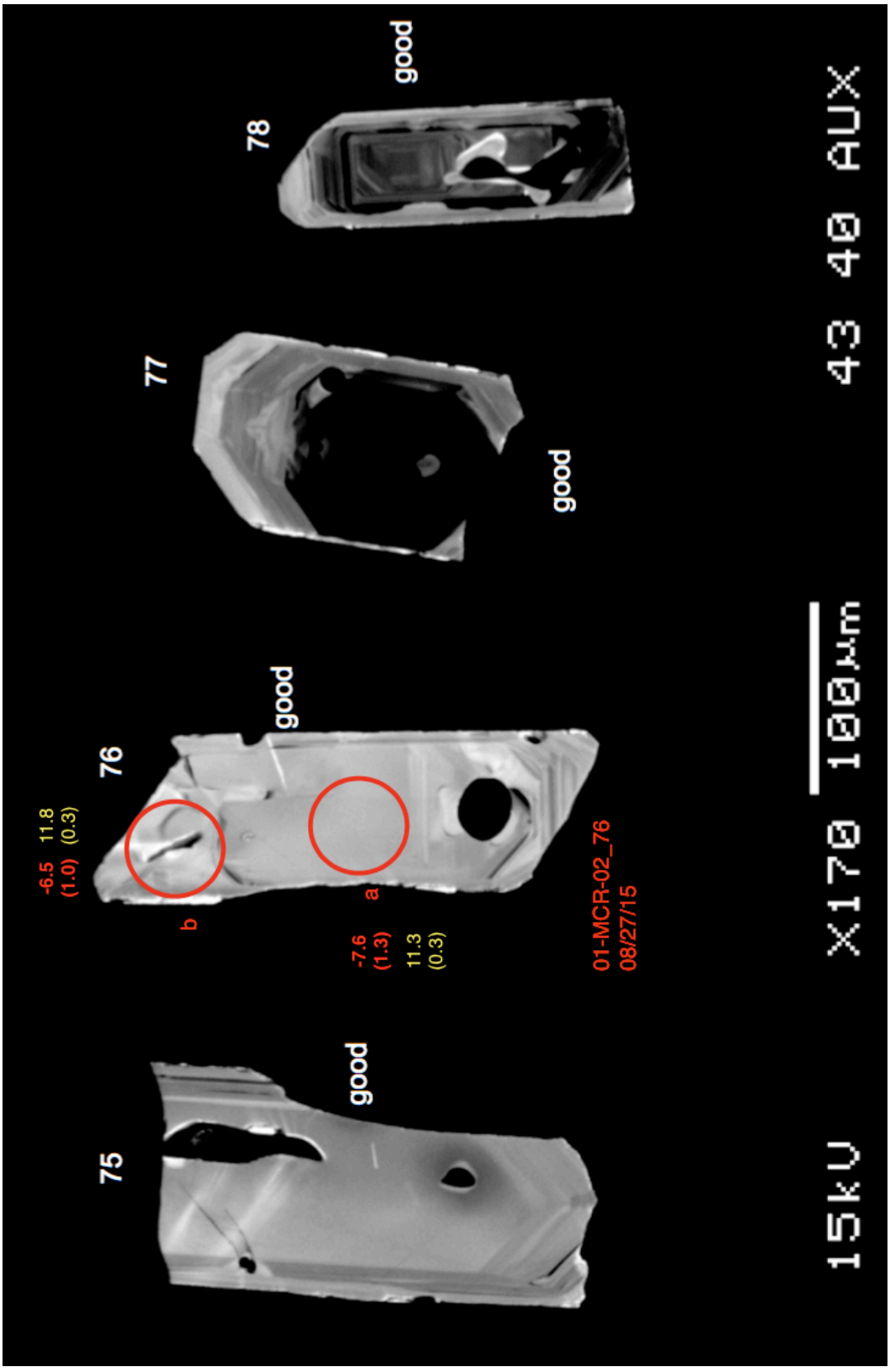

Figure 76. Marys Creek rhyolite

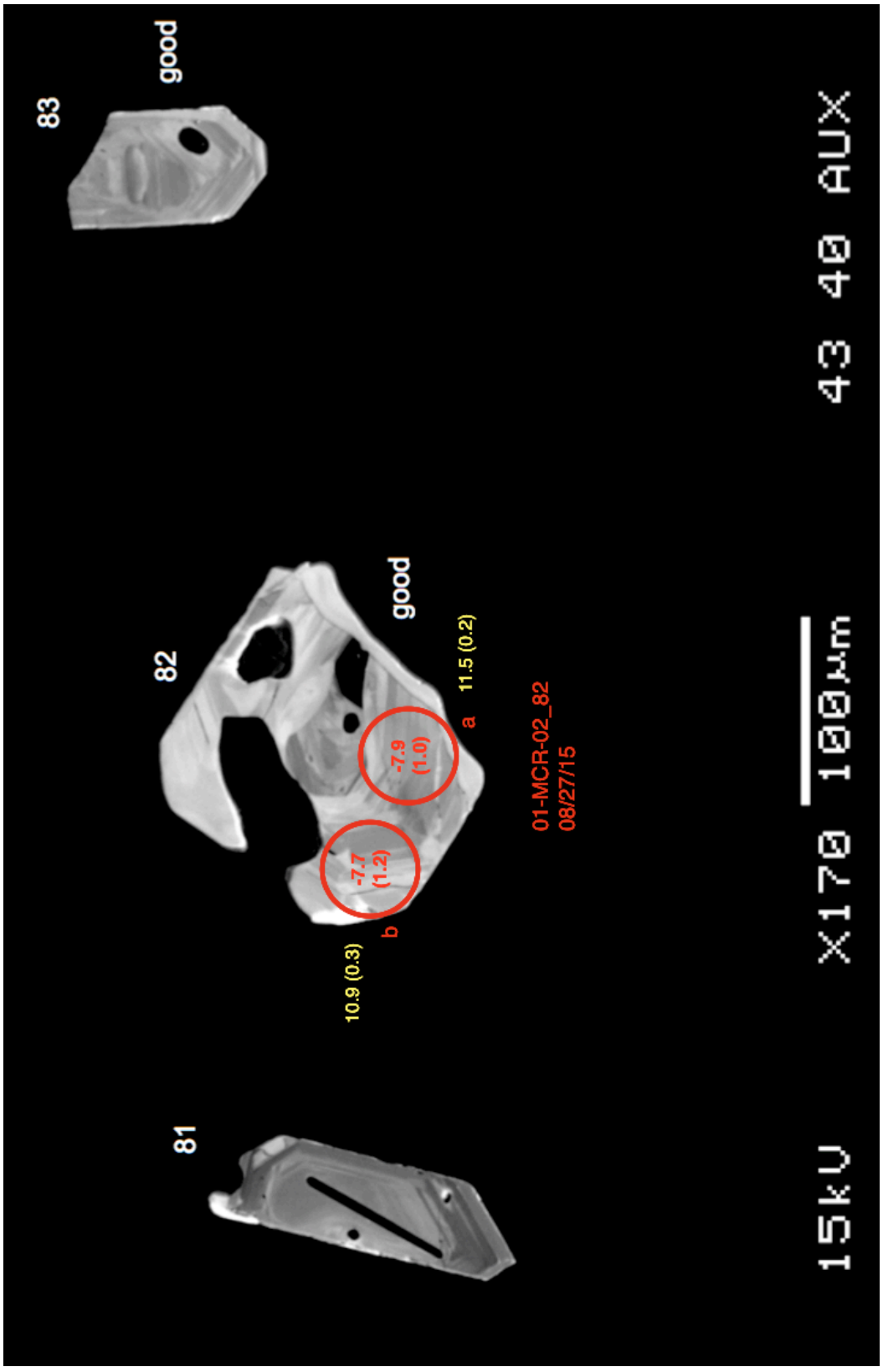

Figure 77. Marys Creek rhyolite

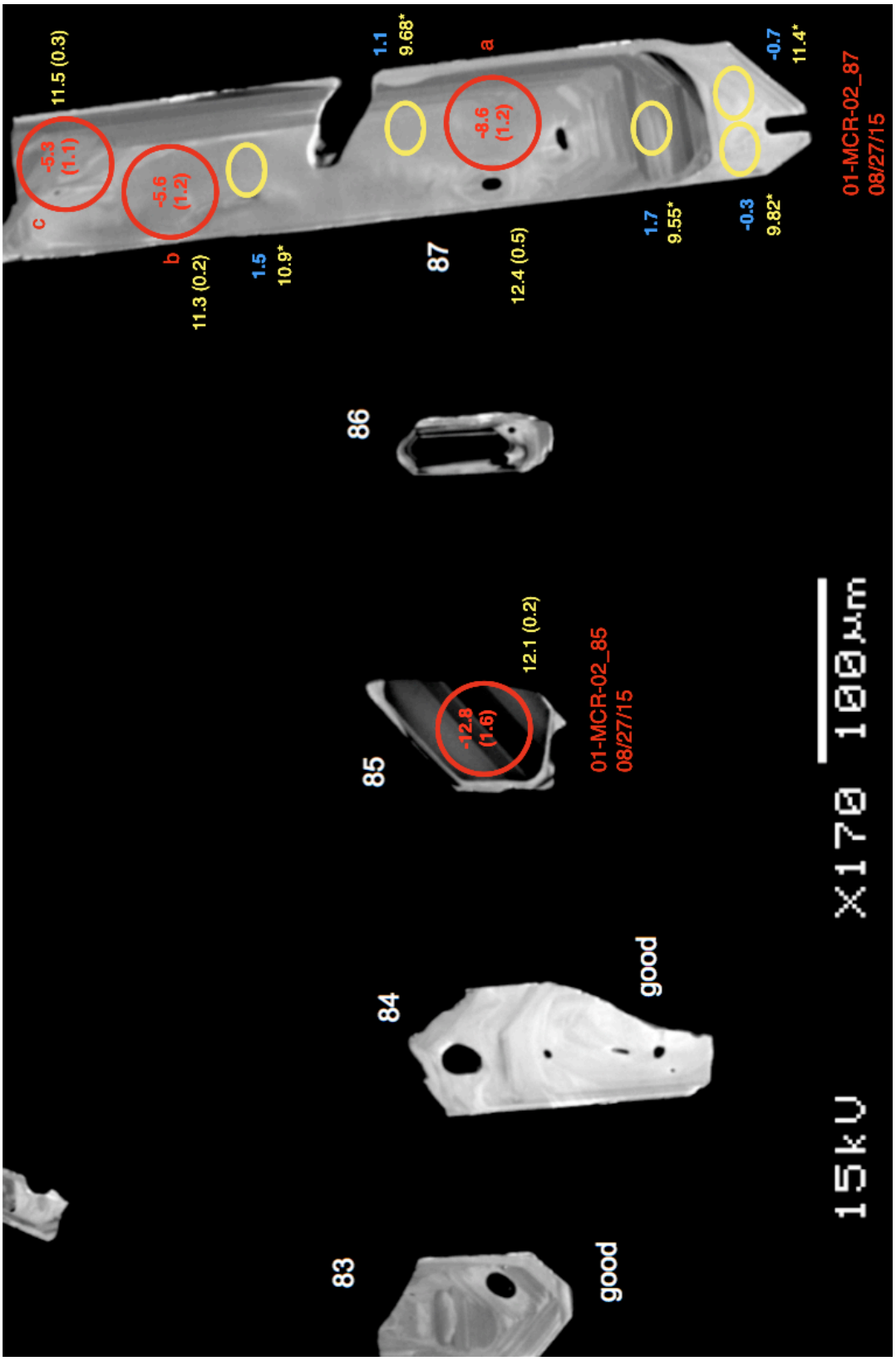

Figure 78. Marys Creek rhyolite

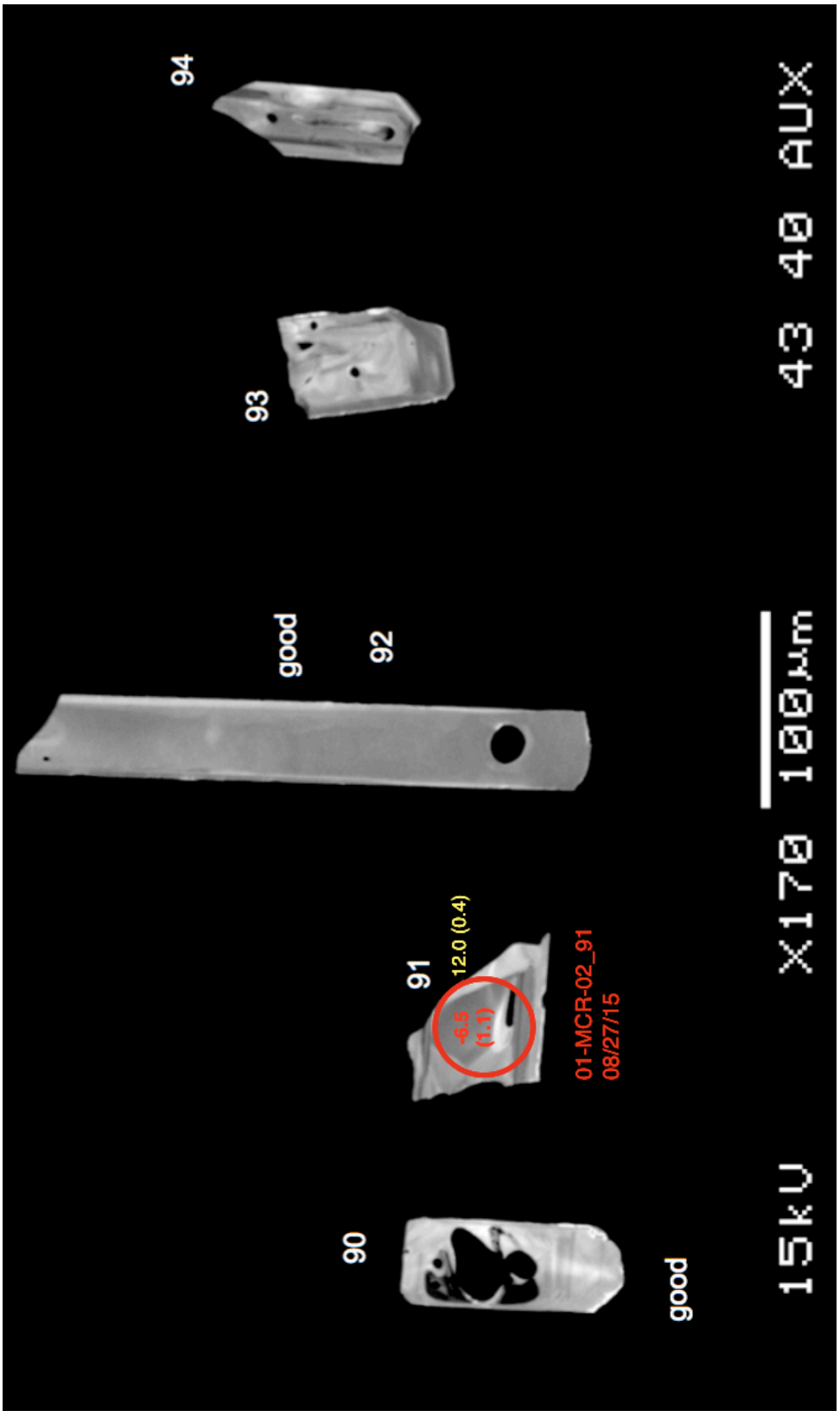

Figure 79. Marys Creek rhyolite